Manipulating the Electronic Spin State of Transition Metal Complexes in Pursuit of Advanced Molecular Materials

A DISSERTATION

SUBMITTED TO THE GRADUATE SCHOOL IN PARTIAL FULFILLMENT OF THE REQUIREMENTS

for the degree

DOCTOR OF PHILOSOPHY

Field of Chemistry

By

Alexandra Gaudette

EVANSTON, ILLINOIS

December 2017

ABSTRACT

The electronic spin state (S) of metal ions is fundamental to the performance of magnets, protein cofactors, and magnetic resonance imaging (MRI) contrast agents. The ability to manipulate the spin state of transition metals allows for the development of advanced materials with emergent properties. This following chapters will introduce two different methods of tuning S, targeting metal-organic magnetic materials and responsive magnetic resonance probes.

One way to tune the spin state of transition metal ions is through the introduction of magnetic coupling. Strong coupling between metal centers is particularly important for the design of magnetic materials, including metal-organic magnets. Metal organic magnets offer several advantages over inorganic magnets, but strong magnetic coupling between metal centers is difficult to achieve across large organic linkers. To address this issue, we targeted a strong magnetic coupling mechanism called double-exchange which stems from fast electron transfer between metal ions in different oxidation states. While double-exchange coupling is well documented in inorganic materials like perovskites, it is exceedingly rare in organic-bridged molecules and materials. As a proof of concept, we synthesized a mixed-valence dinuclear $Fe^{2+}Fe^{3+}$ complex with a diiminobenzoquinone-based bridging ligand to allow electron transfer and magnetic coupling between metal centers. Mössbauer spectroscopy, single crystal X-Ray crystallography, and SQUID magnetometry confirmed the presence of double-exchange coupling and a well-isolated $S = 9/2$ spin ground state. This work represents the largest metal-metal separation observed for double-exchange coupling.

The spin state of transition metal ions can also be manipulated through the modification of its ligand environment. With the appropriate ligand strength and geometry, some iron(II)

complexes can undergo a thermally-induced spin transition, a process called spin-crossover. These spin-crossover compounds occupy a diamagnetic $S = 0$ ground state at low temperature, but are thermally excited to the $S = 2$ state at high temperatures. Considering the resonance frequencies of NMR-active nuclei are highly dependent on S, we have developed a ^{19}F magnetic resonance pH sensor in which the value of S depends on its protonation state. This was accomplished by introducing mildly acidic hydroxylpyridine groups to our previously developed spin-crossover ^{19}F MR thermometer. Deprotonation of the hydroxylpyridine ligands increases S and causes a dramatic 35.25 ppm shift in the ^{19}F resonance frequency at 25 °C as the pH is increased from 4.74 to 7.82. A plot of resonance frequency vs pH can then be used as a standard curve for the direct measurement of pH in samples or tissues.

ACKNOWLEDGEMENTS

Dave Harris, thank you for taking a chance on me five years ago. It has been amazing to see the lab grow from a rotovap in Elad Harel's lab space to the well-oiled machine it is today. Thank you for always pushing me to "leave it all on the field" and for introducing me to the beauty of electronic spin.

Danna Freedman, thank you for always having an open ear. I am so grateful for your support and guidance over the past 5 years. Thanks especially for helping me salvage my double-exchange crystal structure after my data collection was interrupted.

Thank you to the other members of my committee, Tom Meade and Tom O'Halloran. I feel very lucky to have been provided with such knowledgeable and talented advisors. Thank you for asking the hard questions.

Thank you to my collaborators at AFRL, Wendy Goodson, Chia Hung, and Lloyd Nadeau. Thanks especially to Peter Mirau, for all of your hard work, insight, and mentorship over the past year. Thank you to taking the time to explain the physics behind NMR. Working with you over the past year has been a truly great experience.

To the Hardman Group, for making graduate school a reasonably enjoyable experience. In particular, thanks to Audrey, Kang, and Michael who have been with me from the beginning. No one else understands the unique pain of inventory after a lab move or sitting through three days of SQUID training.

Thank you to all of the instrumentation experts in IMSERC particularly Yuyang, Yongbo, Charlotte, Christos, and Habibi for all of your help with my experiments.

To the best parents anyone could ask for. You were always there to offer a love, support, or a really good meal exactly when I needed it most. Thanks for setting a fantastic example for how to live a full and happy life.

Ilya, thank you as well for your constant love and support. I really don't think I could have done this without you, for I would have died of malnutrition a year ago.

To my other friends and family in Chicago, Michigan and beyond, I can't wait to see you all a lot more frequently.

TABLE OF CONTENTS

TABLE OF FIGURES

1 INTRODUCTION

As the spin state (S) is a primary parameter governing molecular electronic structure, S is crucial to the design of transition metal compounds in a variety of applications, including catalysis,[1] magnetism,[2], and magnetic resonance imaging (MRI)[3] and is also of extreme importance to the function of protein cofactors.[4] Given this importance, an enormous amount of work in molecular inorganic chemistry has focused on manipulating the electronic spin state of transition metal-based molecular materials. My thesis work describes two ways to manipulate S towards two different applications.

One method of manipulating S is to introduce magnetic coupling between multiple paramagnetic metal ions and is particularly important for the development of molecule-based magnetic materials with high operating temperatures. Targeting molecules with high values of S is of particular focus in developing metal organic magnets with large relaxation barriers, as the relaxation barrier, U, is dependent on S^2. However as larger values of U are achieved, it becomes increasingly important to consider magnetic coupling in order to make such high spin states thermally stable. For example, the record ground-state spin number of $S = 45$ was achieved in a Fe_{42} cyanide bridged cluster, stemming from ferromagnetic superexchange coupling of 18 high-spin Fe^{3+} atoms through cyanide bridging ligands, but iron centers become decoupled above 5 K.[5] Strong coupling is also necessary for the high-temperature function of higher-dimensional magnets, as the relaxation barrier in single-chain magnets[6] and the ordering temperature in bulk magnets[7] are both proportional to the strength of magnetic exchange interactions between spin carriers.

The work described in Chapter 2 demonstrates that large values of S can be stabilized through strong double-exchange coupling,[8] providing a potential electronic coupling mechanism for the

development of metal-organic magnets. Indeed, several classes of mixed-valence Fe_2 complexes with $S = ^9/_2$ ground states mediated by double-exchange interactions have been isolated and studied, with Fe_2 cores supported by small or single-atom inorganic bridging ligands, which mediate the double-exchange interactions. As an alternative, the employment of organic bridging ligands could provide new synthetic opportunities for high-nuclearity molecules and high-dimensional solids with strong magnetic coupling and itinerant electrons, since these ligands can accommodate extensive chemical.

The work in Chapter 2 describes the synthesis and characterization of the mixed-valence $Fe^{2+}Fe^{3+}$ complex, $[(Me_3TPyA)_2Fe_2(L)]^{3+}$ (**2**) (see Figure 1.1). [9] Variable-temperature dc magnetic susceptibility data for **2** can be modelled considering double-exchange, with a fit to the data providing values of $J = +8.9(7)$ cm^{-1} and the double-exchange parameter, B, equal to 69(4) cm^{-1}. This work demonstrates that quinonoid bridging ligands can mediate electron hopping between metal centers through a double-exchange mechanism in mixed-valence Fe_2 complexes, thereby providing the first example of double-exchange through an organic ligand between Fe centers. Variable-temperature Mössbauer spectra for this complex reveal a thermally-induced transition from a valence-trapped to detrapped state, with an activation energy for electron hopping of 63(8) cm^{-1}. Finally, while the mixed-valence complex exhibits only tails in the ac magnetic susceptibility, a corresponding one electron-reduced Fe^{II}_2 complex displays single-molecule magnet behavior with a relaxation barrier of $U_{eff} = 14(1)$ cm^{-1}.
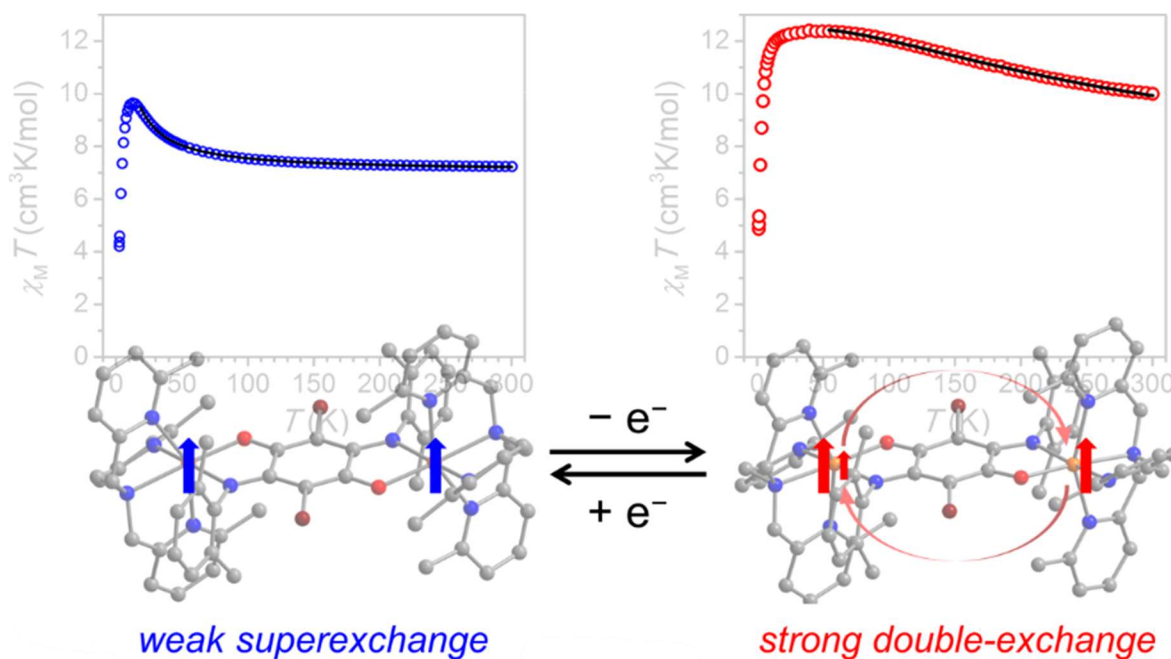
Figure 1.1| One electron oxidation of benzoquinoid-bridged Fe_2 complex yields and mixed-valence compound with an detrapped itinerant electron. dc magnetic susceptibility data confirm and S = $^9/_2$ ground state stabilized by double-exchange coupling.

Alternatively, *S* can also controlled via by designing complexes that can switch between low and high spin states in a process called spin-crossover. Such magnetically bistable molecules and materials have been explored as potential candidates for molecular switches[10] and chemical sensors,[11] as the spin transition can be controlled by a number of external stimuli, such as temperature,[12] pressure,[13] and light.[14] Recently, we and others have started to explore the potential for spin-switchable molecules as bioresponsive sensors for temperature,[15] anions,[16] and enzyme activity.[17] Given the relationship between tissue acidosis and diseases, including cancer[18] and ischemia,[19] a compound that undergoes a spin state transition as a function of pH could serve as a valuable tool for pH sensing. However, pH-induced spin state switching is rare, and the only

compounds that have demonstrated such behavior exhibit pK_a values that are unsuitable for biological sensing applications.[20]
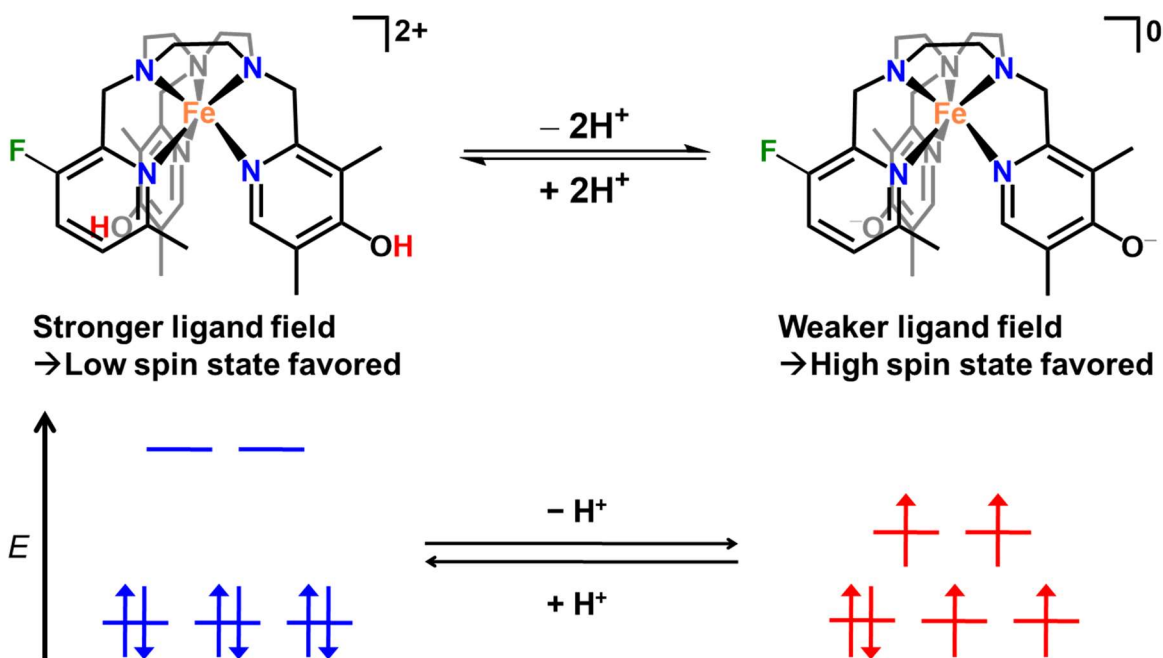
Figure 1.2 | Scheme depicting mechanism of pH-induced change in spin state population. Deprotonation of hydroxylpyridine groups decreases ligand field and stabilizes high-spin state.

As detailed in Chapter 3, I designed a Fe^{2+}-based molecule in which the spin state population can be controlled by deprotonation of the ligand and demonstrated that small changes in S may afford highly sensitive pH probes for ^{19}F magnetic resonance spectroscopy. ^{19}F MRS offers key advantages over the more commonly employed ^{1}H MRS, including most notably the absence of endogenous fluorine in living systems.[21] Furthermore, since both the contact and dipolar contributions to the paramagnetic chemical shift scale with $S(S+1)$,[22] small changes in the electronic spin, S, due to thermal population of the high-spin state afforded a dramatic increase in resonance frequency with temperature. Our group has previously used the relationship between S and chemical shift to make highly sensitive spin-crossover temperature sensors.[15] Building on

these results, I designed a spin-crossover Fe^{2+} complex that has pH-sensitive spin state population (see Figure 1.2). The sensitivity of S stems from deprotonation of hydroxylpyridine groups on the ligand, which decreases the ligand field strength. The molecular and electronic structure of this compound was analyzed *via* single crystal X-ray crystallography, variable-pH UV-Vis absorption spectroscopy as well as variable-pH and variable-temperature solution-phase magnetic susceptibility measurements. Variable pH ^{19}F NMR measurements revealed that the change in the population of S causes a 30.47 ppm shift in the ^{19}F resonance frequency of **3** at 37 °C, which is more pH-sensitive than the best lanthanide-based [19]F pH sensor.

2 ELECTRON HOPPING THROUGH DOUBLE-EXCHANGE COUPLING IN A MIXED-VALENCE FE$_2$ COMPLEX [*]

2.1 ABSTRACT

The ability of a benzoquinonoid bridging ligand to mediate double-exchange coupling in a mixed-valence Fe$_2$ complex is demonstrated. Metalation of the bridging ligand 2,5-di(2,6-dimethylanilino)-3,6-dibromo-1,4-benzoquinone (LH$_2$) with Fe^{II} in the presence of the capping ligand tris(2-(6-methyl)pyridylmethyl)amine (Me$_3$TPyA) affords the dinuclear complex [(Me$_3$TPyA)$_2$Fe^{II}$_2$(L)]$^{2+}$. Dc magnetic measurements, in conjunction with X-ray diffraction and Mössbauer spectroscopy, reveal the presence of weak ferromagnetic superexchange coupling between Fe^{II} centers through the diamagnetic bridging ligand to give an $S = 4$ ground state. Ac magnetic susceptibility measurements, collected in a small dc field, show this complex to behave as a single-molecule magnet with a relaxation barrier of $U_{eff} = 14(1)$ cm^{-1}. The slow magnetic relaxation in the Fe^{II}$_2$ complex can be switched off through one-electron oxidation to the mixed-valence congener [(Me$_3$TPyA)$_2$Fe$_2$(L)]$^{3+}$, where X-ray diffraction and Mössbauer spectroscopy indicate a metal-centered oxidation. Dc magnetic measurements show an $S = {}^9/_2$ ground state for the mixed-valence complex, stemming from strong ferromagnetic exchange coupling that is best described considering electron hopping through a double-exchange coupling mechanism, with a double-exchange parameter of $B = 69(4)$ cm^{-1}. In accordance with double-exchange, an intense feature is observed in the near infrared region and is assigned as an intervalence charge-transfer band. The rate of intervalence electron hopping is comparable to that of the Mössbauer timescale,

such that variable-temperature Mössbauer spectra reveal a thermally-activated transition from a valence-trapped to detrapped state and provide an activation energy for electron hopping of 63(8) cm^{-1}. These results demonstrate the ability of quinonoid ligands to mediate electron hopping between high-spin metal centers, by providing the first example of an Fe complex that exhibits double-exchange through an organic bridging ligand and the largest metal-metal separation yet observed in any metal complex with double-exchange coupling.

2.2 INTRODUCTION

Over the past two decades, a number of molecules have been shown to exhibit slow magnetic relaxation upon removal of an applied external magnetic field, thereby mimicking the behavior previously only associated with bulk magnets.[23] These discrete molecular complexes, which have come to be known as single-molecule magnets, may find use in applications such as high-density spin-based information storage and processing.[24] To date, single-molecule magnets have taken the form of multi- and mononuclear complexes containing transition metals,[25,26] lanthanides,[27,28] and actinides,[29,30] and have been shown to exhibit spin relaxation barriers of up to 652 cm^{-1} [28d] and magnetic blocking temperatures of up to 14 K.[27c] In an effort to further increase the relaxation barriers and blocking temperatures in single-molecule magnets, researchers have focused on maximizing the spin ground state (S) and the axial zero-field splitting parameter (D) of these molecules, as the magnitude of relaxation barrier is given as $U = S^2|D|$.

In addition to the critical parameters S and D, the strength of magnetic interaction between spin centers in a molecule should also be maximized, as this value is directly correlated to the energetic isolation of the ground state from excited states.[31] Moreover, strong coupling is also necessary for

the high-temperature function of higher-dimensional magnets, as the relaxation barrier in single-chain magnets[32] and the ordering temperature in bulk magnets[33] are both proportional to the strength of magnetic exchange interactions between spin carriers. One strategy toward this end is the installation of electron hopping between metal centers in a mixed-valence complex, which can give rise very strong ferromagnetic interactions between high-spin metal centers via a double-exchange mechanism.[34] Indeed, several classes of mixed-valence Fe_2 complexes with $S = {}^9/_2$ ground states mediated by double-exchange interactions have been isolated and studied, with Fe_2 cores supported by hydroxo,[35] phenoxo,[36] alkoxo,[37] and carboxylato[38] bridging ligands. Similarly, a number of iron-sulfur clusters in biology have been shown to exhibit double-exchange that is mediated through sulfido bridges in Fe_2 units.[39]

Notably, all of the above complexes and metalloproteins that exhibit double-exchange coupling feature direct Fe⋯Fe orbital interactions and/or single-atom inorganic bridging ligands, which serve to mediate the double-exchange interactions. As an alternative, the employment of organic bridging ligands would provide new synthetic opportunities for high-nuclearity molecules and high-dimensional solids with strong magnetic coupling and itinerant electrons, owing to the ability of these ligands to accommodate extensive chemical modification and to enable rational chemical design and synthesis. Despite this potential, to date no organic ligand-bridged Fe_2 complex has been shown to exhibit a high-spin ground state through double-exchange. In fact, an imidazolate-bridged $[V_2]^V$ complex provides the only example of organic ligand-based double-exchange in any metal complex, which was shown to exhibit a well-isolated $S = {}^5/_2$ ground state through a double-exchange interaction.[40]

When considering potential organic bridging ligands to mediate double-exchange in mixed-valence molecules, quinonoid-type ligands offer two key potential attributes. First, a number of dinuclear benzoquinonoid-bridged mixed-valence complexes have been shown to support electron delocalization, albeit only in low-spin molecules. [41-44] In addition, the extensive chemical modularity of these ligands offers the possibility to precisely tune the thermodynamics and kinetics of electron transfer. Herein, we report the synthesis and characterization of two redox isomers of a diiminobenzoquinone-bridged Fe_2 complex, $[(Me_3TPyA)_2Fe_2(L)]^{n+}$ ($n = 2, 3$). The latter isomer, which features a mixed-valence $[Fe_2]^V$ core, exhibits an $S = {}^9/_2$ ground state, with magnetic susceptibility and spectroscopic measurements indicating the presence of electron hopping between Fe centers. In addition, variable-temperature Mössbauer spectra reveal the transition from a valence-trapped to detrapped state with decreasing temperature. To the best of our knowledge, this mixed-valence molecule is the first example of an iron complex with double-exchange through an organic bridging ligand, and it features the largest metal-metal separation yet observed in any metal complex involving a double-exchange mechanism.

2.3 EXPERIMENTAL SECTION

2.3.1 General Considerations.

Unless otherwise noted, the manipulations described below were performed under a dinitrogen atmosphere in a Vacuum Atmospheres Nexus II glovebox. Glassware was oven-dried at 150 °C for at least 4 h and allowed to cool in an evacuated antechamber prior to use in the glovebox. Tetrahydrofuran, dichloromethane, and hexanes were dried using a commercial solvent purification system from Pure Process Technology and stored over 3 or 4 Å molecular sieves prior

to use. Deuterated solvents were purchased from Cambridge Isotope Labs or Sigma Aldrich, deoxygenated by three successive freeze-pump-thaw cycles, and stored over 3 or 4 Å molecular sieves prior to use. Hexanes and tetrahydrofuran were typically tested with a standard purple solution of sodium benzophenone ketyl in THF in order to confirm effective oxygen and moisture removal. The compounds $[Fe(MeCN)_6](BAr^F_4)_2$,[45] $[N(4-BrC_6H_4)_3](BAr^F_4)$,[46] tris(6-methyl-2-pyridylmethyl)amine (Me$_3$TPyA),[47] and lithium bis(trimethylsilyl)amide (Li[N(SiMe$_3$)$_2$])[48] were prepared according to literature procedures. All other reagents were purchased from commercial vendors and used without further purification.

2.3.2 2,5-di(2,6-dimethylanilino)-3,6-dibromo-1,4-benzoquinone (LH$_2$).

In air, 2,6-dimethylaniline (2.28 g, 18.8 mmol) was added dropwise to a slurry of 2,3,5,6-tetrabromo-1,4-benzoquinone (2.00 g, 4.72 mmol) and sodium acetate (1.54 g, 18.8 mmol) in 80 mL EtOH at 60 °C. The reaction mixture was then heated at reflux for 48 hours, resulting in the precipitation of a red solid. This solid was collected via vacuum filtration, washed with H_2O (10 mL), EtOH (10 mL), and hexanes (10 mL), and then was dried under reduced pressure for 12 h to yield LH$_2$ as a red solid (0.655 g, 28%). ^{1}H NMR (DMSO-d$_6$): 9.61 (s, 2H) 7.14 (t, 2H) 7.05 (d, 4H) 2.10 (s, 12H).

2.3.3 [(Me$_3$TPyA)$_2$Fe$_2$(L)](BAr$^F_4$)$_2$ (1).

Me$_3$TPyA (0.112 g, 0.337 mmol) was dissolved in THF (2 mL), and the resulting solution was added dropwise with stirring to a solution of $[Fe(MeCN)_6](BAr^F_4)_2$ (0.683 g, 0.337 mmol) in THF (3 mL). The resulting yellow solution was stirred for 5 minutes at ambient temperature, and to it was added a slurry of LH$_2$ (0.085 g, 0.19 mmol) in THF (2 mL). To this mixture, a solution of Li[N(SiMe$_3$)$_2$] (0.056 g, 0.34 mmol) in THF (2 mL) was added dropwise with stirring, resulting in

a dark green solution. After stirring at ambient temperature for 15 min, the solution was filtered through diatomaceous earth. Layering of the filtrate with hexanes produced a mixture of dark brown-green and colorless microcrystalline solid. This solid mixture was washed with cold EtOH (1 mL), and the residual dark green microcrystalline solid was dissolved in THF (4 mL). Layering of hexanes (16 mL) onto the resulting solution gave **1** (0.208 g, 21%) as dark green plate-shaped crystals suitable for single-crystal X-ray diffraction. Anal. Calcd. for $C_{128}H_{90}B_2Br_2F_{48}Fe_2N_{10}O_2$: C, 51.1; H, 3.05; N, 4.65%. Found: C, 51.25; H, 3.06; N, 4.56%.

2.3.4   [(Me3TPyA)2Fe2(L)](BArF4)3·CH2Cl2 (2).

A solution of $[N(4-BrC_6H_4)_3](BAr^F_4)$ (50 mg, 0.035 mmol) in CH_2Cl_2 (4 mL) was cooled to -78 °C and then was added dropwise with stirring to a solution of **1** (100 mg, 0.033 mmol) in CH_2Cl_2 (4 mL) at -78 °C to give a dark red-purple solution. This solution was filtered through diatomaceous earth, and then layered with hexanes (10 mL) at -78 °C to give dark red-purple plate-shaped crystals suitable for single-crystal X-ray diffraction. These crystals were collected *via* vacuum filtration and washed with cold 1:1 CH_2Cl_2/hexanes (20 mL) to afford 86 mg (63%) of 2. Anal. Calcd. for $C_{161}H_{104}B_3Br_2Cl_2F_{72}Fe_2N_{10}O_2$: C, 48.9; H, 2.65; N, 3.54%. Found: C, 49.74; H, 2.92; N, 3.46 %

2.3.5   X-ray Structure Determination.

Single crystals of **1** and **2** suitable for X-ray analysis were coated with deoxygenated Paratone-N oil and mounted on a MicroMounts^{TM} rod. Crystallographic data were collected at 100 K using a Bruker Kappa Apex II diffractometer equipped with an APEX-II detector, a Cu Kα microfocus source, and MX Optics. Raw data were integrated and corrected for Lorentz and polarization effects with SAINT v8.27B.[49] Absorption corrections were applied using SADABS for **1** and **2**.

Space group assignments were determined by examination of systematic absences, E-statistics, and successive refinement of the structures. Structures were solved with SHELXT[50] and further refined with SHELXL[51] operated with the Olex2 interface.[52] The SADI restraint was applied to all atoms of the $[BAr^F_4]^-$ counterions in **1** due to disorder. Positional disorder in several trifluoromethyl groups was modeled with partial occupancies. The enhanced rigid-bond restraint (SHELX keyword RIGU) was applied globally in **2**.[53] Positional disorder in the trifluoromethyl groups on the $[BAr^F_4]^-$ counterions were modeled with partial occupancies. All hydrogen atoms were placed at calculated positions using suitable riding models and refined using isotropic displacement parameters derived from their parent atoms. Thermal parameters were refined anisotropically for all non-hydrogen atoms. Crystallographic data and the details of data collection are listed in Table 2.1. Crystals of both **1** and **2** diffracted weakly, resulting in high R_1 values and

Table 2.1 | Crystallographic data for **1** and **2**

	1	**2**
formula	$C_{128}H_{90}B_2Br_2F_{48}Fe_2N_{10}O_2$	$C_{161}H_{104}B_3Br_2Cl_2F_{72}Fe_2N_{10}O_2$
fw (g/mol)	3005.23	3953.39
space group	$P-1$	$P-1$
wavelength (Å)	1.54178	1.54178
temp. (K)	100	100
a (Å)	12.2741(5)	16.461(6)
b (Å)	20.2397(8)	23.978(9)
c (Å)	26.2330(10)	46.22(2)
α (deg)	88.986(2)	74.978(12)
β (deg)	88.420(2)	89.070(15)
γ (deg)	78.267(2)	71.113(9)
V (Å^3)	6377.8(4)	16625(11)
Z	2	4
d_{calcd} (g cm^3)	1.565	1.579
R_{int}	0.0296	0.0986
$^aR_1$ ($I > 2\sigma(I)$)	0.0901	0.1286
$^bwR_2$ (all)	0.2594	0.3523
GoF	1.024	0.972

low precision on bond lengths. The data collection for **2** was further complicated by decomposition of the crystal during the data collection. Attempts to obtain better data sets for **1** and **2** have thus far been unsuccessful.

2.3.6   Magnetic Measurements.

Magnetic measurements of **1** and **2** were performed on polycrystalline samples sealed in polyethylene bags under a dinitrogen atmosphere. All data were collected using a Quantum Design MPMS-XL SQUID magnetometer from 1.8 to 300 K at applied dc fields ranging from 0 to +7 T. Ac magnetic susceptibility data were collected under a dc field of 750 Oe and an ac field of 4 Oe, oscillating at frequencies in the range 10-1500 Hz. Ac susceptibility data were used to construct Cole-Cole plots, which were then fit using a generalized Debye model[54] in the temperature range 1.8-2.4 K to estimate relaxation times. Dc susceptibility data were corrected for diamagnetic contributions from the sample holder and for the core diamagnetism of each sample estimated using Pascal's constants.[55] M vs H curves, constructed from data collected from 0 to 4 T at 100 K, confirmed the absence of ferromagnetic impurities.

2.3.7   Other Physical Measurements.

Elemental analyses of **1** and **2** were performed by the Midwest Microlab (Indianapolis, IN). Infrared spectra were recorded on a Bruker Alpha FTIR spectrometer equipped with an attenuated total reflectance accessory. UV/Vis/NIR spectra were obtained using a Varian Cary 5000 spectrophotometer. Cyclic voltammetry measurements were carried out in a standard one-compartment cell under dinitrogen, equipped with platinum wires as counter/working electrodes and a silver wire as reference electrode using a CHI 760c potentiostat. Analyte solutions were prepared with 0.1 M solutions of $(Bu_4N)PF_6$ in CH_2Cl_2. Ferrocene was used as an internal standard,

and all potentials were referenced to the $[Cp_2Fe]^{0/1+}$ couple. Zero-field iron-57 Mössbauer spectra were obtained between 5 and 260 K with a constant acceleration spectrometer and a cobalt-57 rhodium source. Prior to the measurements, the spectrometer was calibrated at 295 K with α-iron foil. Samples were prepared in a dinitrogen-filled glovebox and frozen in liquid nitrogen prior to handling in air. All spectra were analyzed using the WMOSS Mössbauer Spectral Analysis Software (www.wmoss.org).

2.4 RESULTS AND DISCUSSION

2.4.1 Syntheses, Structures, and Cyclic Voltammetry.

Reaction of $[Fe(MeCN)_6](BAr^F_4)_2$ with Me_3TPyA in MeCN, followed by treatment with a mixture of LH_2 and $Li[N(SiMe_3)_2]$, resulted in a dark green solution. Subsequent liquid diffusion of hexanes into this solution gave dark green plate-shaped crystals of $[(Me_3TPyA)_2Fe_2(L)](BAr^F_4)_2$ (1) in 21% yield. The asymmetric unit of the crystal structure of **1** features two halves of the $[(Me_3TPyA)_2Fe_2(L)]^{2+}$ cation, with the remainder of each cationic complex related through a crystallographic center of inversion (see Figure 2.1, upper), affording a structure with two crystallographically distinct dinuclear cationic complexes. Each Fe^{II} center resides in a distorted octahedral coordination environment, with nitrogen and oxygen donor atoms of L^{2-} occupying two cis oriented sites and the four nitrogen atoms of Me_3TPyA occupying the remaining sites. Within L^{2-}, the average C-O distance of 1.289(8) Å falls nearly midway between that expected for a single and a double bond (see Table 2.2). In addition, the average C-N distance of 1.30(1) is in close agreement with a double bond. Accordingly, L^{2-} is therefore best described by a resonance form comprising two hydroxo and two imino donors, as has been observed previously in related

complexes of iron, cobalt, and ruthenium.[56-60] The average Fe-O and Fe-N distances of 1.972(6) and 2.244(7) Å, respectively, are indicative of high-spin $S = 2$ Fe^{II} centers and support the above description of L^{2-}. Finally, the structure of **1** features a mean intramolecular Fe···Fe distance of 8.126(2) Å and a closest intermolecular Fe···Fe distance of 9.618(2) Å.

Table 2.2 | Selected mean interatomic distances (Å) in 1 and 2 at 100 K.

	1	**2**		**1**	**2**
Fe-N2	2.319(7)	2.23(2)	C1-C2	1.37(1)	1.38(3)
Fe-N3	2.303(7)	2.21(2)	C2-C3	1.43(2)	1.46(3)
Fe-N4	2.233(8)	2.25(2)	C3-C1A	1.51(1)	1.49(3)
Fe-N5	2.203(6)	2.15(2)	C-C_{avg}	1.43(1)	1.44(3)
Fe-N$_{TPyA, avg}$	2.264(7)	2.21(2)	N1-C2	1.30(1)	1.32(2)
Fe-N1	2.244(7)	2.13(2)	O1-C3	1.289(8)	1.28(2)
Fe-O1	1.972(6)	1.94(1)	Fe···Fe$_{intra}$	8.126(2)	8.029(4)
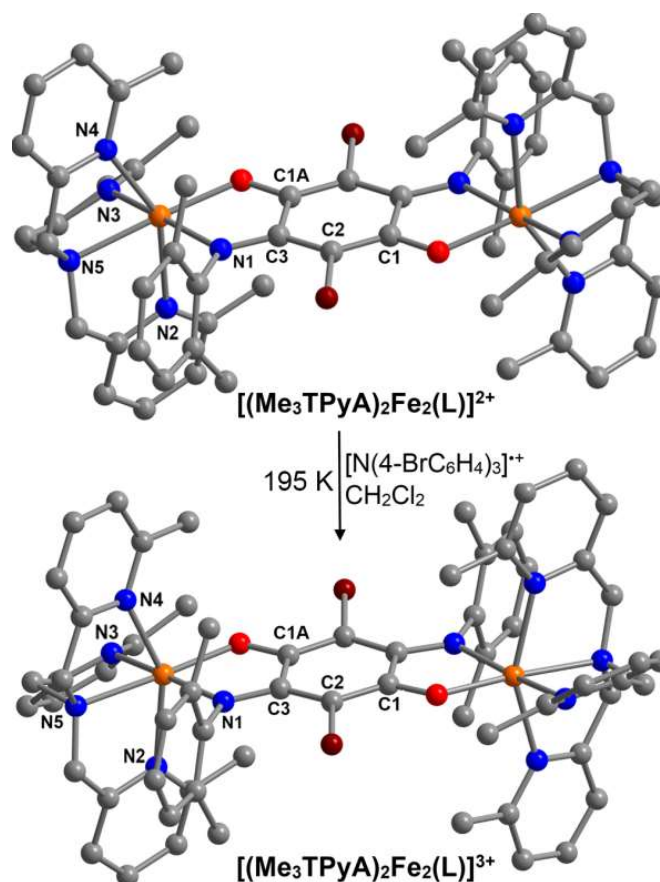
Figure 2.1| Oxidation of [(Me₃TPyA)₂Fe₂(L)]²⁺ (**1**) (upper) to give [(Me₃TPyA)₂Fe₂(L)]³⁺ (**2**) (lower). Orange, maroon, red, blue, and gray spheres represent Fe, Br, O, N, and C atoms, respectively; H atoms are omitted for clarity.

The cyclic voltammogram of a CH_2Cl_2 solution of 1, shown in Figure 2.2, exhibits three reversible redox processes, centered at $E_{1/2}$ = +0.704, +0.364, and −1.45 V vs [Cp₂Fe]⁰ᐟ¹⁺, with an open-circuit voltage of −0.83 V. Based on precedent in other benzoquinonoid-bridged Fe complexes, we assign the wave at negative potential to a ligand-based $L^{2-/3-\bullet}$ process and the two waves at positive potential to metal-based $Fe^{II/III}$ processes.[43h] The potential separation of $\Delta E_{1/2}$ = 0.340 V between the metal-based waves corresponds to a comproportionation constant of K_c =5.52 × 10⁵ for the reaction [(Me₃TPyA)₂Fe₂(L)]²⁺ + [(Me₃TPyA)₂Fe₂(L)]⁴⁺ → 2[(Me₃TPyA)₂Fe₂(L)]³⁺, which suggests that the mixed-valence species [(Me₃TPyA)₂Fe₂(L)]³⁺ can be chemically isolated. Toward

this end, a solution of **1** in CH_2Cl_2 was treated at −78 °C with one equivalent of the iminium radical cation-containing oxidant $[N(4\text{-}BrC_6H_4)_3](BAr^F_4)$[46, 61] to give a dark red-purple solution. Monitoring of this reaction in CD_2Cl_2 by ^1H NMR revealed the complete consumption of **1** with concomitant formation of a new paramagnetic species (see Figure 2.3). Layering of cold hexanes onto this solution afforded dark red-purple plate-shaped crystals of $[(Me_3TPyA)_2Fe_2(L)](BAr^F_4)_3 \cdot CH_2Cl_2$ (**2**) in 63% yield upon storage at −78 °C.
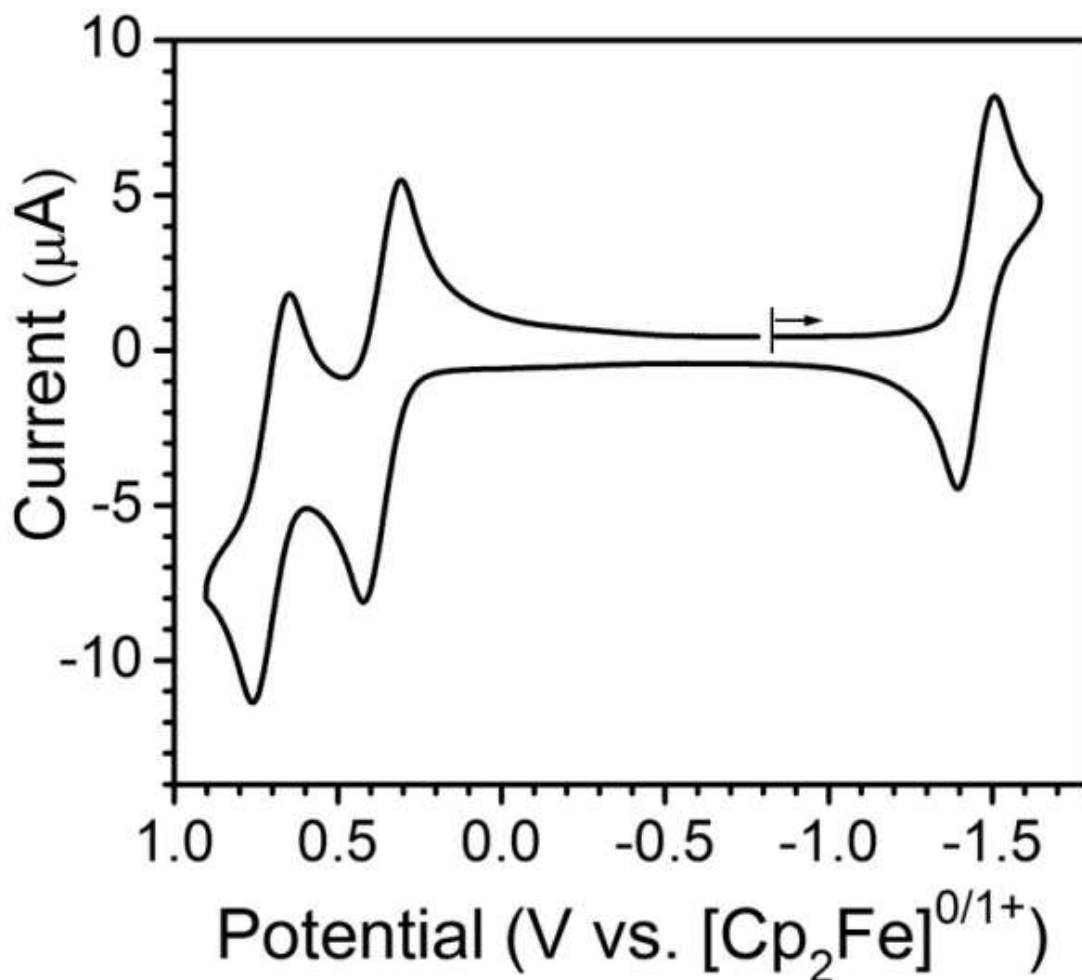
Figure 2.2 | Cyclic voltammogram obtained for a CH_2Cl_2 solution of **1** using a glassy carbon working electrode, 50 mV/s scan rate, and 0.1 M $(Bu_4N)PF_6$ supporting electrolyte.
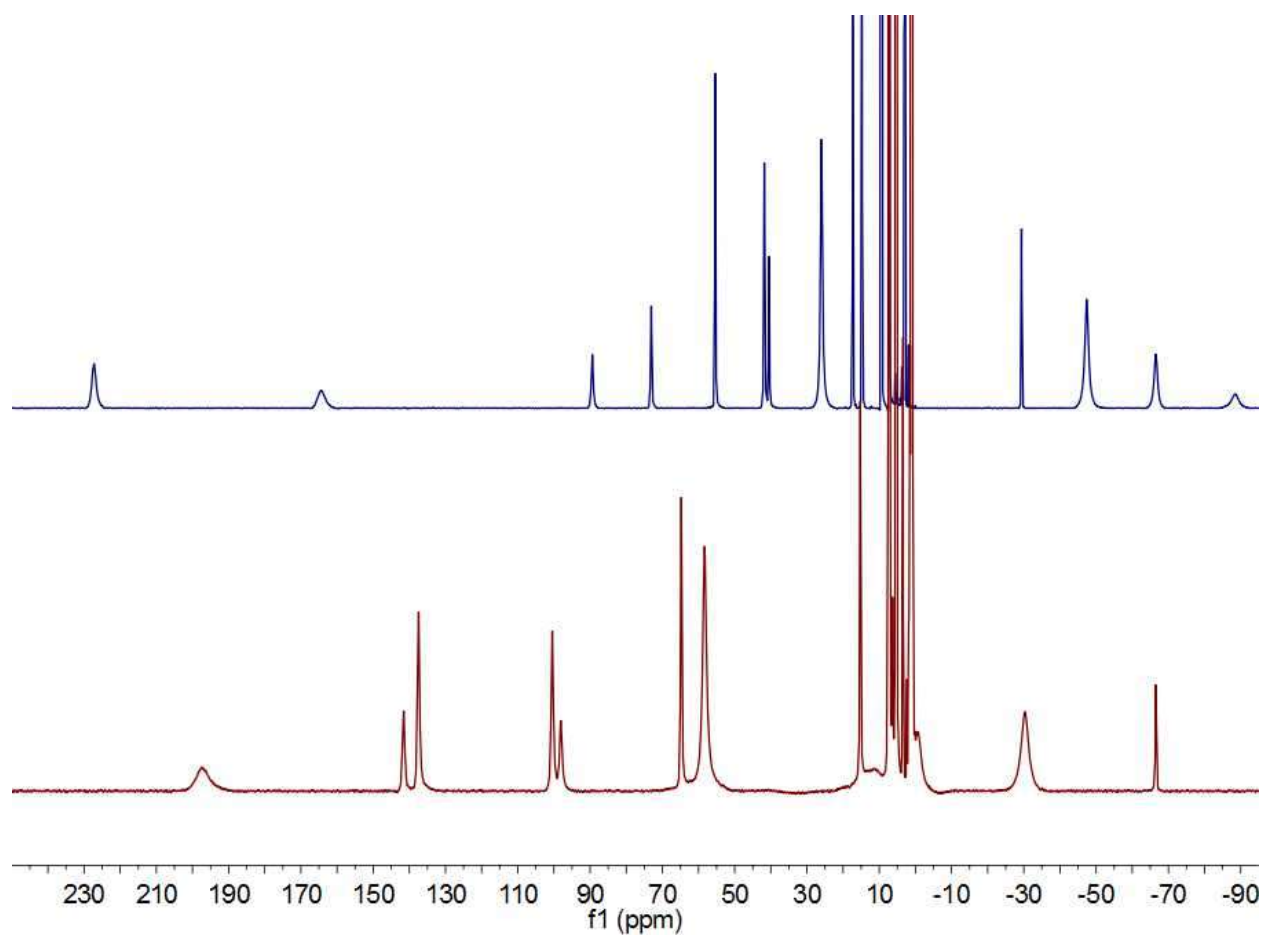
Figure 2.3 | NMR spectrum for 1 (top, blue) and 2 (bottom, red) in CD_2Cl_2 at −35 °C.

The crystal structure of **2** at 100 K exhibits an asymmetric unit that contains one full molecule of $[(Me_3TPyA)_2Fe_2(L)]^{3+}$, where the two iron centers are crystallographically inequivalent, along with two halves of different molecules of $[(Me_3TPyA)_2Fe_2(L)]^{3+}$, with the remaining half of each molecule related through a crystallographic inversion center (see Figure 2.1, lower). Despite the presence of four crystallographically unique Fe centers in the structure of 2, the individual Fe-$N_{Me3TPyA}$ and Fe-N_L distances are nearly identical, although the Fe-O distances range from 1.900(9) to 1.97(2) Å. While the different Fe-O distances indicate valence-trapping, the collective low

variation in bond distances at the independent Fe sites suggests that the asymmetry of the structure may also partially arise due to crystal packing of the $[BAr^F_4]^-$ counteranions.

Table 2.2 summarizes the key comparisons in mean interatomic distances between the cationic complexes in **1** and 2. In moving from **1** and **2**, the mean Fe-$N_{Me3TPyA}$ distance decreases by 2.5%, from 2.264(7) to 2.21(2) Å. In addition, the mean Fe-N_L distance decreases by 5.2%, from 2.244(7) to 2.13(2) Å, and the Fe-O distance decreases by 1.5%, from 1.972(6) to 1.94(1) Å. These decreases in bond lengths at Fe upon oxidation are consistent with an oxidation of a single Fe center from Fe^{II} to Fe^{III}. In further support of this assignment, no statistically significant differences are observed for the C-C_L, N-C_L, or C-O bond distances. In sum, this structural comparison provides strong evidence that the oxidation of **1** to **2** involves a primarily metal-based redox event. Finally, the structure of **2** features a mean intramolecular Fe···Fe distance of 8.029(4) Å and a closest intermolecular Fe···Fe distance of 14.360(6) Å.

2.4.2 Mössbauer Spectroscopy.

In order to confirm the presence of a metal-based oxidation and to probe the nature of mixed valency in $[(Me_3TPyA)_2Fe_2(L)]^{3+}$, Mössbauer spectra were collected for solid samples of **1** and **2** under zero applied field. At 5 and 80 K, the spectrum for **1** consists of a slightly broadened quadrupole doublet. Each of these spectra is best fit considering two symmetric quadrupole doublets with equal areas and linewidths, consistent with the presence of two crystallographically inequivalent Fe centers, with an average isomer shift and quadrupole splitting of $\delta = 1.095(2)$ mm/s and $\Delta E_Q = 2.152(4)$ mm/s, respectively, and a linewidth of $\Gamma = 0.270(3)$ mm/s (see Figure 2.4 and Table 2.3). These parameters are typical of high-spin Fe^{II} and are close to those previously reported for diiminobenzoquinone- and azophenine-bridged Fe^{II}_2 complexes.[60,62]

Table 2.3 | Mössbauer Spectral Parameters[a] of [(Me₃TPyA)₂Fe₂(L)](BArᶠ₄)₂ (**1**)

T, K	*δ,* mm/s[b]	*ΔE_Q,* mm/s	*Γ,* mm/s	*Area,* %	c^2	Site Assignment
80	1.095(1)	2.152(1)	0.338(2)	100	1.776	Fe(II)
	1.163(1)	2.148(2)	0.270(3)	50	0.705	Fe1, Fe(II)
	1.027(1)	2.155(2)	0.270(3)	50	-	Fe2, Fe(II)
5	1.126(2)	2.217(4)	0.384(6)	100	0.535	Fe(II)
	1.16(1)	2.22(1)	0.37(1)	50	0.535	Fe1, Fe(II)
	1.09(1)	2.21(1)	0.37(1)	50	-	Fe2, Fe(II)

[a]Statistical fitting errors are given in parenthesis. The actual errors are approximately two to three times as large. [b]The isomer shifts are reported relative to *a*-iron foil measured at 295 K.
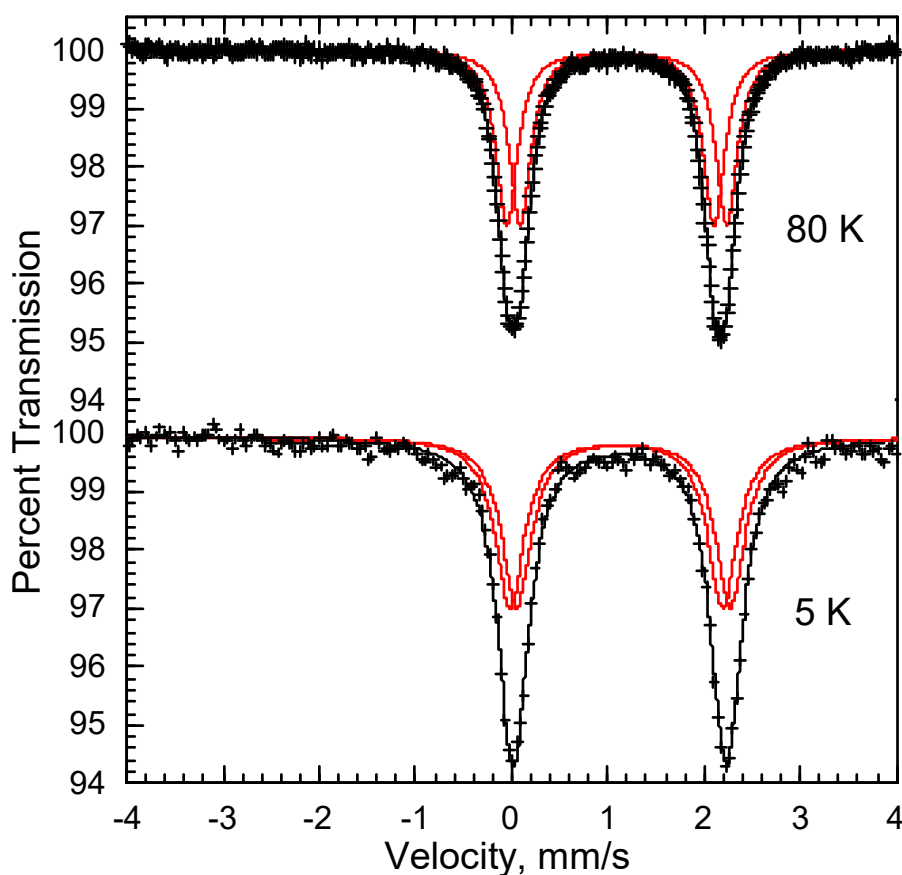
Figure 2.4 | Mössbauer spectra of [(Me3TPyA)2Fe2(L)](BArF4)2, 1, obtained at the indicated temperatures and fit with two symmetric quadrupole doublets.
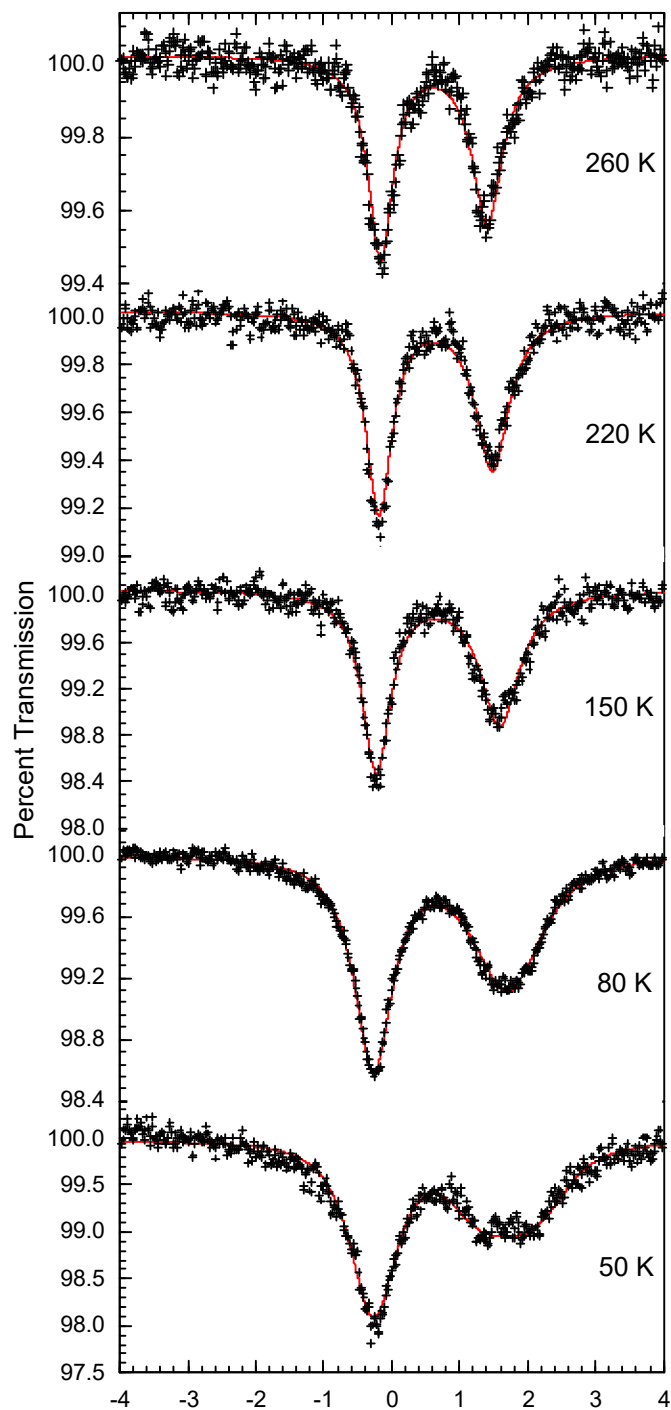
Figure 2.5 | Mössbauer spectra for **2**, measured at the indicated temperatures between 50 and 260 K. Black crosses represent experimental data, and red lines correspond to fits considering electron hopping between Fe^{II} and Fe^{III}, as described in the text.

The Mössbauer spectra for **2** were measured from 50 to 260 K and at 5 K (see Figure 2.5). The former spectra reveal a spectral profile as a function of temperature that is typical of a Class II/III mixed-valence, high-spin Fe^{II}Fe^{III} complex that is undergoing relaxation as the result of electron hopping on the Mössbauer time scale of 10^{-8} s. The spectra from 50 to 260 K were fit with a model [63] involving relaxation between a high-spin Fe^{II} and a high-spin Fe^{III} quadrupole doublet (see Appendix, and Table 2.3). Note that these fits are made difficult because of an absence of knowledge of the Fe^{II} and Fe^{III} doublet hyperfine parameters, first, in the slow relaxation limit that is unknown because of the onset of slow paramagnetic relaxation below ca. 40 to 50 K and, second, of the average Fe$^{II/III}$ doublet in the fast relaxation limit, presumably somewhat above ca. 300 K and unobtainable because of the thermal instability of **2** above ca. 260 K. Furthermore, it is difficult to surmise the best intrinsic line

width to use in the relaxation fits owing to the presence of three crystallographically distinct Fe_2 complexes in **2**, which involve electron hopping between Fe1···Fe1, Fe2···Fe2, and Fe3···Fe4, each of which may possibly have slightly different limiting hyperfine parameters. To overcome this difficulty, a $\Gamma = 0.40$ mm/s, the narrowest absorption observed near 0 mm/s at 220 K, was used to represent an upper limit of the intrinsic line width of the limiting quadrupole doublets.

Despite these difficulties, the observed spectral profiles are well fit considering an electron hopping mechanism. The fits clearly reveal that both limiting quadrupole doublets must have the same sign of ΔE_Q, a sign that is most likely positive based on a fit of the 5 K spectrum discussed below. An Arrhenius plot of the logarithm of the electron hopping frequency, n, yields an activation energy for the electron hopping of 63(8) cm^{-1}, a value that is consistent with the upper limit of activation energy obtained from optical spectroscopy (see Figure 2.6).
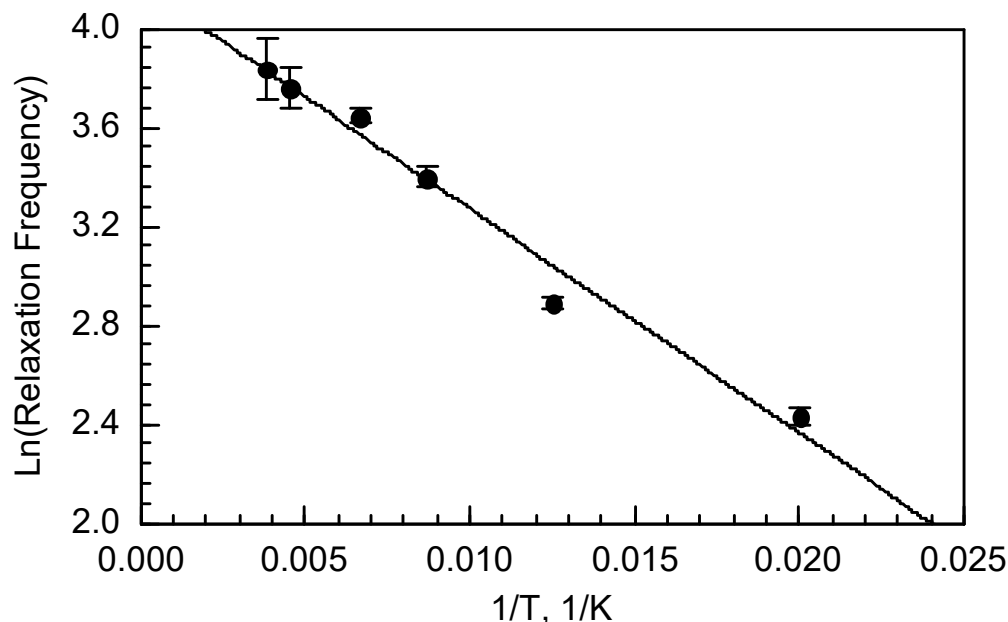
Figure 2.6 | An Arrhenius plot of the logarithm of the electron hopping frequency, ν, obtained between 50 and 260 K. The line yields an activation energy for the electron transfer of 90(10) K or 63(8) cm^{-1}.

The presence of a very asymmetric quadrupole doublet with decreasing temperature is indicative of an intervalence charge transfer, or electron hopping, between the Fe^{II} and Fe^{III} ions at a rate similar to that of the Mössbauer timescale. Similar behavior has been observed in $Fe^{II}Fe^{III}$-containing cationic biferrocene[64] and oxo-centered, carboxylato-bridged $Fe^{II}Fe^{III}_2$[65] complexes. Importantly, heat capacity measurements have shown that the onset of valence detrapping in these complexes usually stems from a phase transition involving intermolecular interactions, rather than simple thermal effects on the kinetics of electron hopping.[66] In these cases, the absence of any line broadening with changing temperature provided key evidence of such lattice effects. In contrast, the spectra of **2** unambiguously exhibit asymmetric line broadening with decreasing temperature as would be expected as the rate of electron hopping decreases with decreasing thermal energy. Moreover, to our knowledge, **2** represents the second example of a molecule with a high-spin ground state that exhibits changes in electron hopping rate observable by Mössbauer spectroscopy, which was first reported in a phenoxo-bridged $[Fe_2]^V$ complex with an $S = {}^9/_2$ ground state.[67]

Below 50 K, the spectrum for **2** undergoes further broadening and splitting until broadened sextets indicative of slow paramagnetic relaxation are observed at 5 K (see Appendix). This behavior suggests that **2** is a single-molecule magnet at zero-field on the Mössbauer timescale (see below for further discussion of ac magnetic susceptibility measurements). Analysis of the 5 K Mössbauer spectrum of **2** is complicated because it requires at least three broadened sextets and, apparently, a small amount of Fe^{III} impurity. Nevertheless, the data can be modeled assuming that at 5 K **2** is a Class I mixed-valence complex with no electron hopping, but in which the Fe^{II} and Fe^{III} ion moments undergo $\pm z$ anisotropic slow paramagnetic relaxation with a frequency of 6.8(3) MHz, similar to the Larmor precession frequency (see Appendix).

Table 2.4 | Mössbauer spectral parameters[a] for **2**.

T (K)	$\delta_{Fe(II)}$ (mm/s)[b]	$\Delta E_{Q,Fe(II)}$ (mm/s)	$\delta_{Fe(III)}$ (mm/s)[b]	$\Delta E_{Q,Fe(III)}$, (mm/s)	ν (MHz)	*Area* (%ε) (mm/s)
260	0.738(9)	2.39(2)	0.506(9)	0.74(2)	46(6)	0.75(1)
220	0.783(7)	2.58(1)	0.515(7)	0.75(2)	43(3)	1.19(1)
150	0.820(5)	2.89(1)	0.546(4)	0.74(1)	38(1)	2.40(3)
115	0.845(5)	3.00(1)	0.551(4)	0.77(1)	30(1)	3.40(3)
80	0.861(4)	3.15(1)	0.576(4)	0.80(1)	18.0(3)	3.85(1)
50	0.880(7)	3.17(2)	0.570(8)	0.81(2)	11.4(3)	4.12(5)

[a]Statistical fitting errors are given in parentheses. The actual errors may be two to three times as large. The iron(II) to iron(III) area ratio was fixed to 1:1 and the linewidth to 0.40 mm/s. [b]The isomer shifts are reported relative to α-iron foil measured at 295 K.

2.4.3 UV/Vis/NIR Spectroscopy.

To further probe the electronic structure of **1** and **2**, the UV/Vis/NIR absorption spectra were collected for solution samples of **1** and **2** in CD_2Cl_2 at 298 K. The UV/Vis/NIR spectrum for **1**, as depicted in Figure 2.7, exhibits an intense band at $\nu_{max} = 26737$ cm^{-1} with a shoulder at 27548 cm^{-1}. Considering the reduction of intensity upon oxidation (see below), we tentatively assign these features to metal-to-ligand charge transfer (MLCT) transitions. The sharp peaks in the low energy region likely correspond to vibronic overtones of CH_2Cl_2 impurities in the solvent that are too intense for an accurate background subtraction.
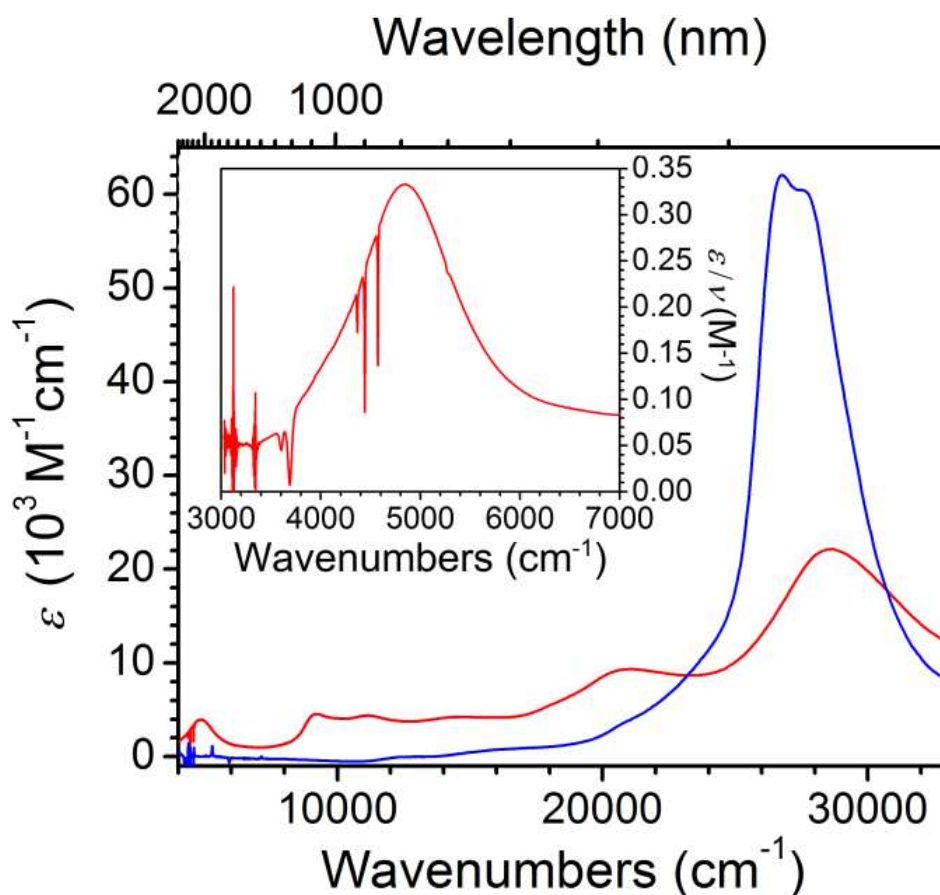
Figure 2.7 | UV/Vis/NIR spectra for CD_2Cl_2 solutions of **1** (blue) and **2** (red). Inset: Expanded view of the NIR region for **2**.

The spectrum obtained for **2** exhibits a markedly different profile than that of **1**. The MLCT bands broaden and decrease in intensity, with the maximum shifted to $\nu_{max} = 28409$ cm^{-1}. Additionally, new bands appear at $\nu_{max} = 20703$, 13986, 10952, and 4810 cm^{-1}. Of the new bands, we assign the lowest energy feature, positioned in the NIR region with a molar absorption coefficient of $\varepsilon_{max} = 3950$ M^{-1}cm^{-1}, to an intervalence charge transfer (IVCT) band. This feature exhibits a bandwidth of $\Delta\nu_{1/2} = 1403$ cm^{-1}, which is much lower than the theoretical bandwidth of $\nu^{\circ}_{1/2,} = (2310(\nu_{max}))^{1/2} = 3333$ cm^{-1} obtained considering a classical two-state model.[68] Accordingly, this result suggests the presence of at least some degree of valence detrapping in the mixed-valence compound **2**.

Further, the ratio between the experimental and the theoretical bandwidth gives the parameter $\Gamma = 1 - v_{1/2}/v°_{1/2} = 0.58$, which is close to the value of $\Gamma = 0.50$ expected at the Class II-Class III transition.[69] Moreover, the relatively symmetric shape of the IVCT band lacks a cutoff on the lower energy side that is commonly observed in delocalized, Class III mixed-valence compounds (see Figure 2.7, inset).[70] Taken together with the variable- temperature Mössbauer spectra and crystal structure, these results suggest that **2** may be best described as a Class II-III mixed-valence compound.[71] Note that an examination of the solvent dependence of the IVCT transition was precluded due to the low stability of **2** in other solvents that have high transparency in the NIR region. Nevertheless, the solid-state spectrum of **2** was investigated by diffuse reflectance spectroscopy (see Figure 2.8). Although the detector limit did not allow full analysis of the IVCT band, the position and relative intensity of the NIR features are similar to those observed in solution.
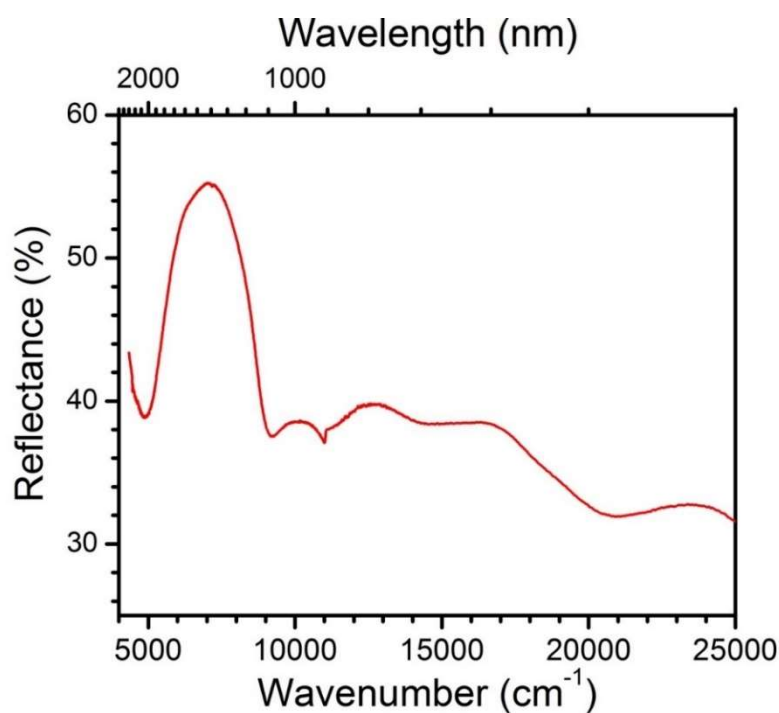
Figure 2.8 | Diffuse reflectance spectrum of **2** diluted with KBr powder at ambient temperature

To quantify the extent of electronic coupling and the energy of activation, the IVCT band was further analyzed. In the case of a delocalized Class III system, the electronic coupling parameter, is given as $H_{AB} = 0.5\nu_{max} = 2405$ cm^{-1}, which provides an upper limit of the coupling. Alternatively, H_{AB} may be calculated using the classical two-site model considering the electron transfer distance in Å, r_{AB},[70, 72] which gives $H_{AB} = 419$ cm^{-1} in the case of **2**. Here, the value of H_{AB} represents a lower bound, as the electron transfer distance in the presence of significant electronic mixing with the ligand orbitals and/or between metal centers across the ligand can be considerably shorter than the geometrical distances obtained from the structural analysis. Furthermore, the energies of the thermal and optical processes are directly related, and the activation energy for thermal electron transfer in a Class II system is given as $E_a = \nu_{max}/4 - H_{AB} + H_{AB}^2/\nu_{max} = 820$ cm^{-1}.[68] As the value of $H_{AB} = 419$ cm^{-1} represents the lower limit of electronic coupling, the true value of E_a in **2** should be smaller than 820 cm^{-1}, which is consistent with the observation of a thermally-activated transition from a trapped to detrapped valence in the Mössbauer spectra.

The double-exchange parameter B can also be extracted from the IVCT band. In the case of a delocalized Class III system, the most intense energy of the IVCT transition, ν_{max}, is equated with the spin state transition in the ground state, $10B$.[73] This gives a double-exchange parameter of $B = 481$ cm^{-1} for **2**, which is nearly seven times larger than that extracted from the magnetic data (see below). The observed discrepancy arises due to the fact that this analysis assumes full electronic delocalization and neglects vibronic coupling and the role of the bridging ligand. Finally, note that the classical two-state theory cannot adequately describe electronic exchange for compounds near the Class II-Class III transition, and as such a complete understanding of the electronic structure of **2** requires a detailed theoretical analysis that is beyond the scope of this work

2.4.4   Static Magnetic Properties.

To assess potential magnetic interactions in **1** and **2**, variable-temperature dc magnetic susceptibility data were collected for solid samples under an applied field of 1 T. The resulting plots of $\chi_M T$ vs T for both compounds are shown in Figure 2.9. In the case of 1, $\chi_M T = 6.65$ cm^3 K mol^{-1} at 300 K, corresponding to two magnetically isolated $S = 2$ Fe^{II} centers with $g = 2.08$. As the temperature is decreased, the value of $\chi_M T$ increases gradually down to 100 K and then more steeply, reaching a maximum value of 8.9 cm^3 K mol^{-1} at 12 K. This increase in $\chi_M T$ with decreasing temperature indicates weak ferromagnetic superexchange coupling between high-spin Fe^{II} centers through the diamagnetic bridging ligand, resulting in an S coupling between high-spin Fe^{II} centers through the diamagnetic bridging ligand, resulting in an $S = 4$ ground state. Below 12 K, $\chi_M T$ decreases sharply to a value of 3.86 cm^3 K mol^{-1} at 1.8 K, stemming from Zeeman splitting, zero-field splitting, and potentially weak intermolecular interactions. In order to quantify the ferromagnetic superexchange in **1**, the data were fit in the temperature range 18-300 K to the Van Vleck equation according to the spin Hamiltonian $\hat{H} = -2J(\hat{S}_{Fe1} \cdot \hat{S}_{Fe2})$, giving an exchange constant of $J = +1.21(1)$ cm^{-1} and $g = 2.08(1)$. Here, the magnitude of J is consistent with other examples of benzoquinonoid-bridged Fe$^{II}_2$ complexes. More specifically, $|J|$ is larger than that of 0.70 cm^{-1} reported for a tetraoxolene-bridged complex,[74] but smaller than that of 2.90(2) cm^{-1} reported for a tetraazalene-bridged complex.[62] This intermediate value is expected, given the presence of two hydroxo and two imino donors on the bridging ligand of 1. Finally, low-temperature magnetization data collected for **1** confirm the presence of an $S = 4$ ground state, with a fit to the data giving parameters of $D = -4.9$ cm^{-1} and $g = 2.1$ (see Figure 2.10).

In contrast, the plot of $\chi_M T$ vs T for **2** exhibits a markedly different profile. The value of $\chi_M T$ at 300 K of 9.97 cm^3 K mol^{-1} is considerably higher than that expected for isolated $S = 2$ Fe^{II} and $S = ^5/_2$ Fe^{III} centers with $g = 2.00$. As the temperature is decreased, $\chi_M T$ undergoes a nearly monotonic increase to reach a maximum value of 12.38 cm^3 K mol^{-1} at 40 K, very close to that expected for exclusive population of an $S = ^9/_2$ ground state. Indeed, low-temperature magnetization data confirm this ground state, with a fit to the data giving parameters of $D = +3.4$ cm^{-1} and $g = 2.1$ (see Figure 2.11).[75] Considering the evidence for electron hopping in 2, as ascertained from Mössbauer and UV/Vis/NIR spectra, the data were modeled using the Van Vleck equation according to the Hamiltonian $\hat{H} = -2J(\hat{S}_{Fe1} \cdot \hat{S}_{Fe2} \hat{O}_{Fe1} + \hat{S}_{Fe1} \cdot \hat{S}_{Fe2} \hat{O}_{Fe2}) + BT_{AB}$, where J and B are the Heisenberg and double-exchange constants, respectively.[76] Accordingly, fits to the data
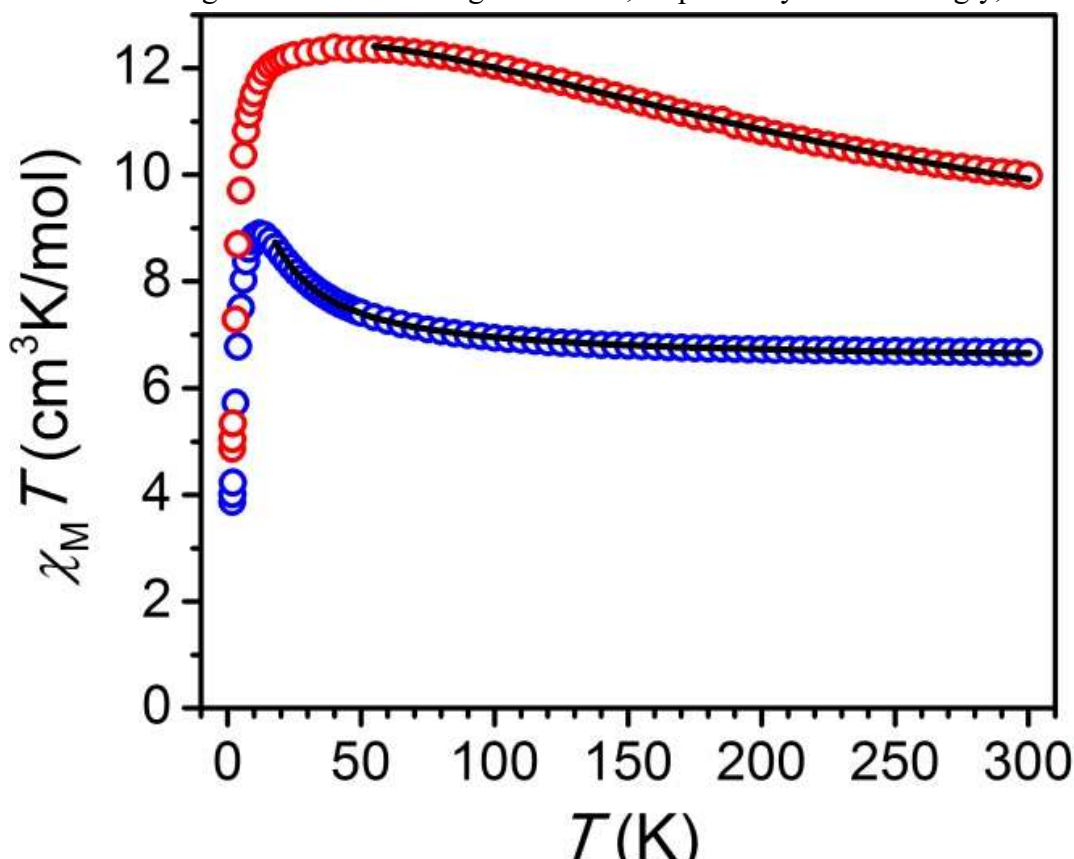
Figure 2.9 | Variable-temperature dc magnetic susceptibility data for 1 (blue) and 2 (red), collected under an applied field of 1 T. The black lines correspond to fits of the data

in the temperature range 65-300 K give values of $J = +8.9(7)$ cm^{-1}, $B = 69(4)$ cm^{-1}, and $g = 2.01(1)$. Note that small changes to the low-temperature limit of data included in fitting leads to large variation in J and B, likely owing to the lack of significant temperature dependence of the $\chi_M T$ vs T data. Moreover, these parameters represent the average values of the three crystallographically distinct intramolecular Fe$\cdots$Fe contacts. As such, these values should be regarded as estimates. Below 50 K, the data undergo a sharp downturn as a result of zero-field and Zeeman splitting.

The value of $B = 69(4)$ cm^{-1} obtained for **2** is smaller than those previously reported in other double-exchange complexes. Previously reported mixed-valence [Fe$_2$]^V complexes exhibit values of $B = 943$**Error! Bookmark not defined.**[a]-1320[25b] cm^{-1}, while a [V$_2$]^V complex was shown to feature a double-exchange parameter of $B = 122$ cm^{-1}.[40]40,[77] This difference likely stems in part from the large intramolecular Fe$\cdots$Fe distance of 8.029(4) Å in 2, compared to those of 2.509(6)[35b]-2.7485(5)[37] Å and 6.188 Å[40]40 previously observed in the [Fe$_2$]^V complexes and [V$_2$]^V complex noted above, respectively. Indeed, to the best of our knowledge, **2** features the largest intramolecular metal-metal separation yet observed in a complex the exhibits a double-exchange mechanism, although we note that a radical-radical separation of ca. 22 Å has been observed for an $S = {}^3/_2$ organic molecule with electron delocalization between two nitronyl nitroxide centers mediated through a bridging Co^{III} *bis*(semiquinonate) unit.[78] Nevertheless, the present result demonstrates the ability of quinonoid bridging ligands to mediate electron hopping through double-exchange coupling between high-spin metal centers.
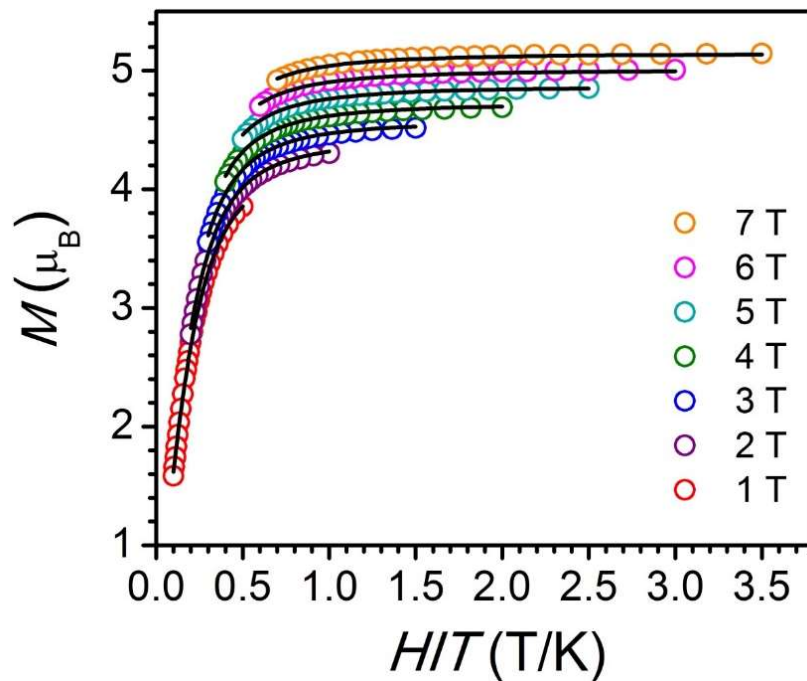
Figure 2.10 | Low-temperature magnetization data for **1** at selected fields. Black lines indicate fits to data.
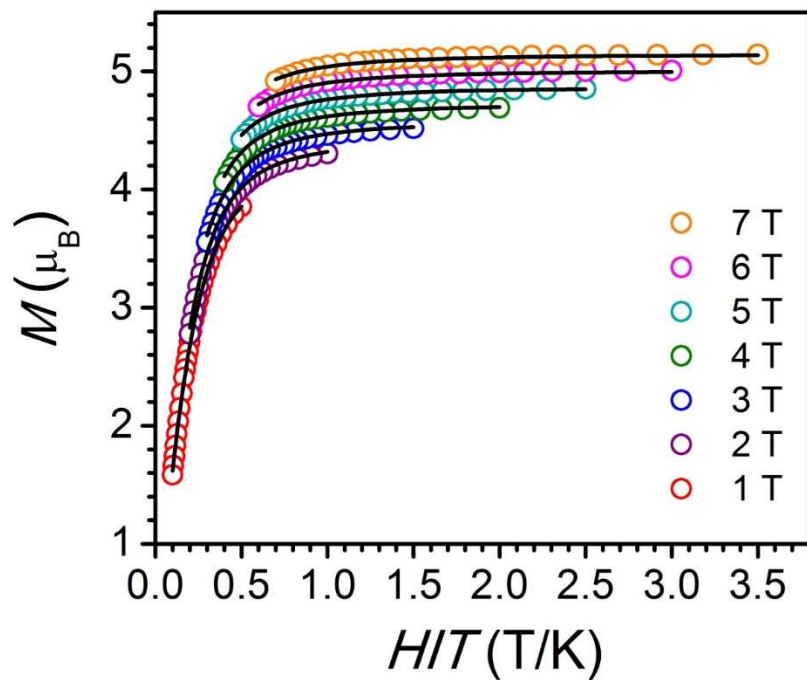
Figure 2.11 | Low-temperature magnetization data for 2 at selected fields. Black lines indicate fits to data

2.4.5 Dynamic Magnetic Properties.

Finally, in order to probe for slow magnetic relaxation in **1** and **2**, variable-frequency ac magnetic susceptibility data were collected on solid samples. Under zero applied dc field, neither compound exhibits slow magnetic relaxation above 1.8 K and below 1500 Hz. However, upon application of a 750 Oe dc field, which provides the slowest dynamics as confirmed by field dependence of variable-frequency ac susceptibility data, temperature-dependent features are observed for **1** in the plot of χ_M'' vs ν (see Figure 2.12). These isotherms were used to construct Cole-Cole plots, which were fit considering a generalized Debye model to extract a relaxation time at each temperature.[544] As depicted in the inset of Figure 2.12, the relaxation time of **2** exhibits thermally-activated behavior at high temperature, with a linear fit to the data in the temperature range 2.2-2.4 K providing a relaxation barrier of 14(1) cm^{-1}. Note that, owing to the weak intramolecular Fe···Fe exchange of $J = +1.21(1)$ cm^{-1} in **1**, this slow relaxation may involve spin excited states in addition to the $S = 4$ ground state.

Under an applied dc field of 750 Oe, **2** exhibits only tails at high frequency above 1.8 K, and therefore features a much smaller relaxation barrier than **1**. Accordingly, the complex $[(Me_3TPyA)_2Fe^{II}_2(L)]^{n+}$ can be described as a redox-switchable single-molecule magnet, where one-electron redox chemistry can be employed to significantly modulate magnetic relaxation time. To date, very few redox-switchable single-molecule magnets have been reported,[79] including a cyano-bridged Mn_4Re cluster,[80] a nindigo-bridged Co_2 complex,[81] and an azophenine-bridged Fe_2 complex.[62] This class of molecules could find use in devices such as single-molecule transistors, where a gate voltage can be used to reversibly switch spin state and relaxation dynamics.[82] Interestingly, the presence of tails in the plot of χ_M'' vs ν for **2** suggests slow magnetic relaxation,

albeit corresponding to a miniscule relaxation barrier, in spite of a positive D value extracted from magnetization data. As fitting magnetization data is often an unreliable method for obtaining the sign of zero-field splitting parameters, we cannot rule out the possibility that D is in fact negative. Nevertheless, recent work has uncovered a number of single-molecule magnets with positive D values confirmed by high-field EPR measurements.[26 c,83]
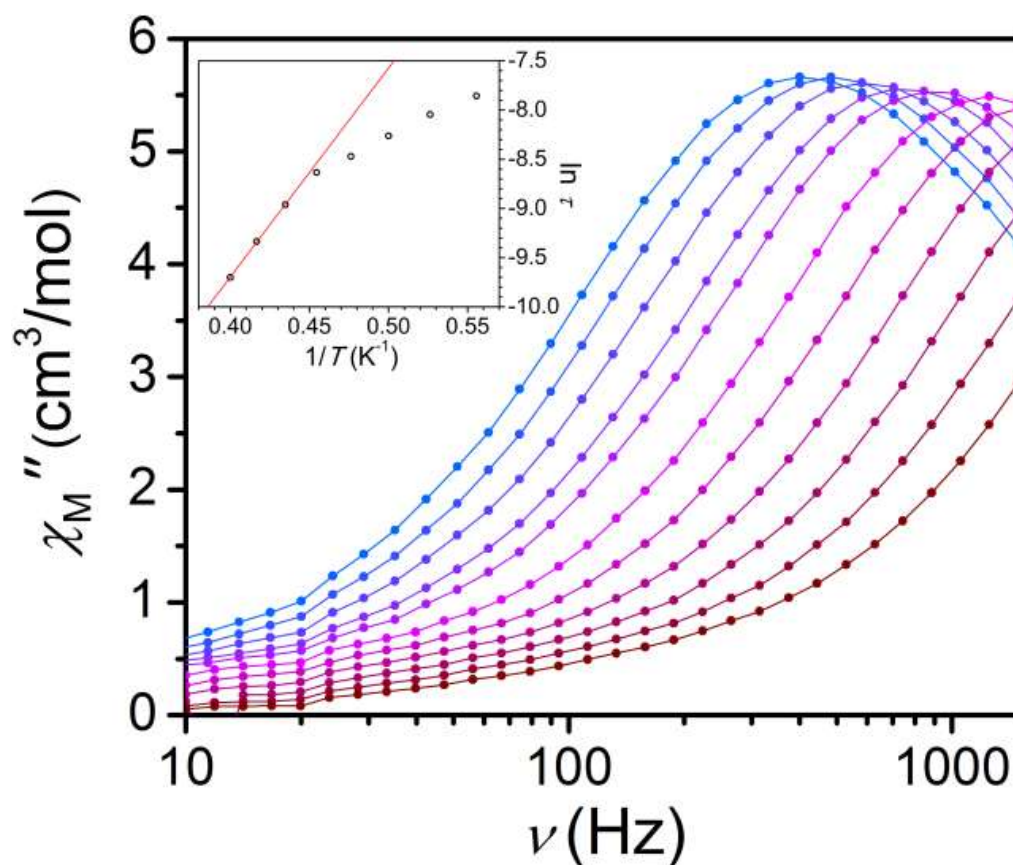
Figure 2.12 | Variable-frequency ac susceptibility data for **1**, collected under an applied dc field of 750 Oe in the temperature range 1.8 (blue) to 2.7 (red) K. Inset: Arrhenius plot of relaxation time, with a linear fit giving U_{eff} = 14(1) cm⁻¹.

The presence of slow magnetic relaxation in **2** is consistent with the Mössbauer spectra presented above, which reveal slow paramagnetic relaxation at 5 K even at zero field, because Mössbauer spectroscopy probes a much faster timescale, and therefore higher temperature range, than ac

magnetic susceptibility. As such, we hypothesize that fast relaxation processes, such as quantum tunneling or spin-spin relaxation, are operative in **2** at the low temperatures probed by ac susceptibility. Indeed, a similar phenomenon, where slow magnetic relaxation is evident from zero-field Mössbauer spectra but only from ac susceptibility under an applied dc field, has been reported in mononuclear trigonal pyramidal[84] and linear, two-coordinate[85] Fe^{II} complexes.

2.5   SUMMARY AND OUTLOOK

The foregoing results demonstrate that quinoid bridging ligands can mediate electron hopping between metal centers through a double-exchange mechanism in mixed-valence Fe_2 complexes, as exemplified in the $S = {}^9/_2$ complex $[(Me_3TPyA)_2Fe_2(L)]^{3+}$, thereby providing the first example of double-exchange through an organic ligand between Fe centers. Accordingly, variable-temperature dc magnetic susceptibility data can be modelled considering double-exchange, with a fit to the data providing values of $J = +8.9(7)$ cm^{-1} and $B = 69(4)$ cm^{-1}. Moreover, variable-temperature Mössbauer spectra for this complex reveal a thermally-induced transition from a valence-trapped to detrapped state, with an activation energy for electron hopping of 63(8) cm^{-1}. Finally, while the mixed-valence complex exhibits only tails in the ac magnetic susceptibility, a corresponding one electron-reduced Fe^{II}_2 complex displays single-molecule magnet behavior with a relaxation barrier of $U_{eff} = 14(1)$ cm^{-1}. Work is underway to elucidate the role of benzoquinone substitution in governing double-exchange and to incorporate benzoquinone bridges into mixed-valence extended solids.

3 PH-DEPENDENT SPIN-STATE POPULATION AND 19F NMR CHEMICAL SHIFTS VIA REMOTE LIGAND PROTONATION IN AN IRON(II) COMPLEX

3.1 ABSTRACT

The synthesis and characterization of an Fe^{II} complex, $[(LH_2)Fe]^{2+}$ (**3**), which undergoes a deprotonation-induced change in spin state population is described. Variable temperature solution phase magnetic susceptibility data collected *via* the Evans method demonstrate spin-crossover behavior at pH 4.47, while at pH 7.78 the high spin state almost completely stabilized more stabilized. We attribute this shift toward greater population of the $S = 2$ state with increasing pH to a decreased ligand field strength of L^{2-} vs H_2L, owing to the weaker π acidity of the latter. This change in the population of S causes a 30.47 ppm shift in the ^{19}F resonance frequency of **3** at 37 °C. To the best of our knowledge, $[(LH_2)Fe]^{2+}$ represents the first example of an ^{19}F MRS pH probe that employs a pH-induced spin state change

3.2 INTRODUCTION

The development of transition metal-based molecules and materials that can be switched between low-spin and high-spin electronic states has constituted a highly active area of research over the past several decades.[86] Indeed, the magnetic bistability of such spin-crossover compounds make them potential candidates for molecular switches[87] and chemical sensors,[88] as the spin transition can be controlled by a number of external stimuli, such as temperature,[89] pressure,[90] and light.[91] Recently, we and others have begun to explore the potential for spin-switchable molecules as bioresponsive sensors for temperature,[92] anions,[93] and enzyme activity.[94] Given the relationship between tissue acidosis and diseases, including cancer[95] and ischemia,[96] a compound that

undergoes a spin state transition as a function of pH could serve as a valuable tool for pH sensing. Nevertheless, pH-induced spin state switching is rare, and the only compounds that have demonstrated such behavior exhibit pK_a values that are unsuitable for biological sensing applications.[97]

One approach toward biological pH sensing is to employ pH-induced changes in the chemical shift of ^{19}F resonances, typically caused by an interconversion between species of different protonation states. Here, the use of ^{19}F magnetic resonance spectroscopy (MRS) offers key advantages over the more commonly employed ^{1}H MRS, including most notably the absence of endogenous fluorine in living systems.[98] Furthermore, the resonance frequency of the ^{19}F nucleus is highly sensitive to its chemical environment so that small changes in spin density lead to drastic changes in chemical shift.[99] Indeed, diamagnetic ^{19}F MRS pH sensors with values near p$K_a = 7$ have been developed for *in vivo* applications, where over 12 ppm variation in ^{19}F chemical shift was observed between the protonated and deprotonated forms.[100] In addition, the sensitivity of ^{19}F MRS sensors can be further improved by incorporating paramagnetic metal ions, as the difference in resonance frequency between the protonated and deprotonated forms is amplified by the presence of contact (through-bond) and dipolar (through-space) contributions to the chemical shift.[101]

We previously demonstrated that spin-crossover Fe^{II} complexes can facilitate chemical shift-based MR thermometry.[99a] Here, since both the contact and dipolar contributions to the paramagnetic chemical shift scale with $S(S+1)$,[102] small changes in the electronic spin, S, due to thermal population of the high-spin state afforded a dramatic increase in resonance frequency with temperature. Building on these results, we sought to develop a spin-crossover Fe^{II} complex that undergoes a deprotonation-induced spin state change near biological pH for ^{19}F chemical shift-

based pH sensing. Herein, we report the synthesis and characterization of an Fe^{II} complex that features a new 1,4,7-triazacyclononane (TACN) ligand appended with three 2-picolyl donors, and demonstrate that pH-induced spin state switching can engender highly sensitive ^{19}F MRS pH probes. To our knowledge, this work provides the first example of a ^{19}F MR pH sensor that employs a pH-induced spin-crossover.

In order to develop an ^{19}F MR probe that undergoes a pH-induced spin state transition, we set out to design a ligand that (1) forms a water-soluble complex with Fe^{II}, (2) features an ^{19}F reporter group, and (3) affords a ligand field that changes dramatically with pH. Toward this end, we selected 4-hydroxy-3,5-dimethyl-2-pyridyl groups as the pH sensing moieties, because the ability of hydroxylpyridines to engender significant changes in the electronic structure of transition metal compounds upon protonation or deprotonation has been demonstrated in Fe-,[103] Co-,[104] Re-,[105] Ru-,[106] and Ir-based[107] compounds. We thus hypothesized that incorporating hydroxylpyridine groups into a spin-crossover complex would create a compound with a pH-sensitive spin state population (see Figure 3.1). Along these lines, we targeted the ligand LH_2, based on a modification of our previously reported ^{19}F spin-crossover temperature sensor[99a] with hydroxylpyridine substituents.

decreasing ligand field and thus increasing population of high-spin
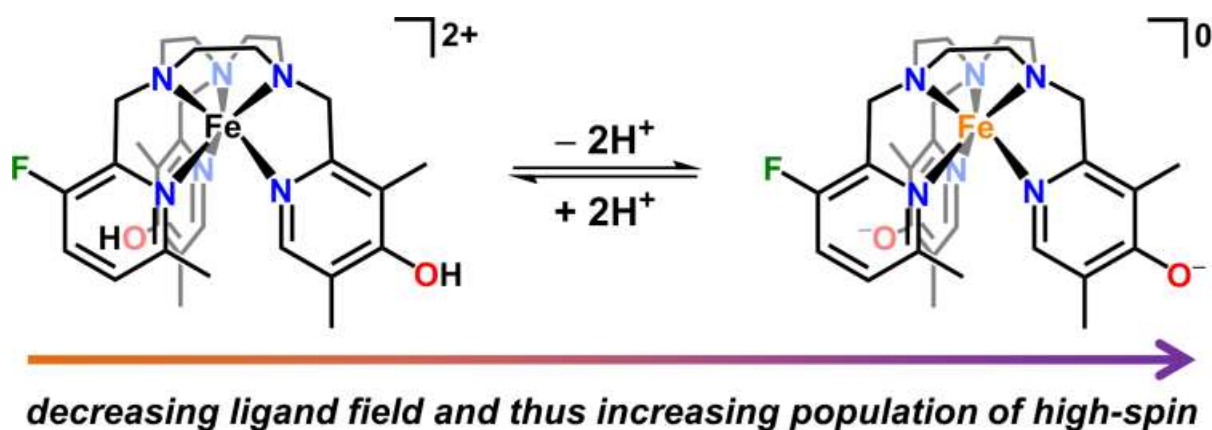
Figure 3.1 | Scheme depicting the mechanism for pH sensing using the Fe^{II} complex $[(LH_x)Fe]^{x+}$ where x = 0–2. With increasing pH, the pendent hydroxylpyridine groups become deprotonated, and the resulting weaker ligand field leads to a higher population of the S = 2 spin state. This spin state dependence gives a dramatic change in the ^{19}F resonance frequency as a function of pH.

3.3   EXPERIMENTAL SECTION

3.3.1   General Considerations.

Unless otherwise specified, the manipulations described below were carried out under a dinitrogen atmosphere in a glovebox or using standard Schlenk line techniques. For water-free manipulations, glassware was oven-dried at 150 °C for at least 4 h and allowed to cool under vacuum prior to use. Acetonitrile (MeCN), dichloromethane (CH_2Cl_2), diethyl ether (Et_2O) and methanol (MeOH) were dried using a commercial solvent purification system from Pure Process Technology and stored over 3 or 4 Å molecular sieves prior to use. Water was obtained from a purification system from EMD Millipore. Elemental analysis was conducted by Midwest Microlab Inc. Deuterated solvents were purchased from Cambridge Isotope Laboratories. The compounds H_2Ts-TACN and 3-fluoro-2-formyl-6-methylpyridine were synthesized following literature procedures.[92a] All other compounds were purchased from commercial vendors and used without further purification.

3.3.2 Synthesis of *N, N'*-di(4-methoxy-3,5-dimethyl-2-picoyl)-*N''*-monotosyl-1,4,7-triazacyclononane.
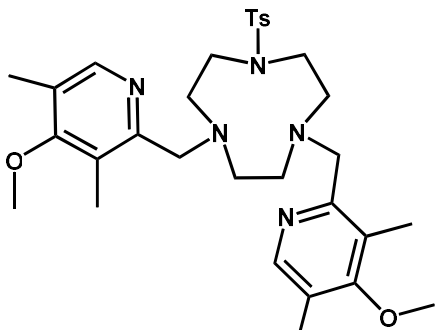
Ts-TACN (1.8 g, 6.4 mmol) and 2-(chloromethyl)-4-methoxy-3,5-dimethylpyridine hydrochloride (2.82 g, 12.7 mmol) were dried for 12 h under vacuum before being added to a flame-dried 200 mL Schlenk flask along with dry DIPEA (8.4 g, 65 mmol) and dry MeCN (50 mL). The reaction mixture was stirred and heated at 60 °C under a dinitrogen atmosphere. The reaction was followed by ESI-MS, which indicated a complete reaction after 16 h. The resulting white suspension was cooled to room temperature and evaporated to dryness to give an orange oil and white crystalline solid. The crude mixture was dissolved in 1M aqueous NaOH solution (30 mL) and extracted with CH_2Cl_2 (4 × 50 mL). The organic layer was dried with $MgSO_4$(s), filtered and evaporated to dryness under reduced pressure to give an orange oil. The crude product was purified by column chromatography using silica gel. The column was loaded with 5% triethylamine (TEA) in hexanes and initially run with 1.5% TEA in 1:1 EtOAc/hexanes to remove excess 2-(chloromethyl)-4-methoxy-3,5-dimethylpyridine starting material. Then the solvent mixture was changed to 2% TEA in EtOAc to elute the title compound, which was obtained as a white oily solid after removing the solvent under reduced pressure (2.2 g, 3.8 mmol, 59%). ESI-MS (*m/z*): Calcd. for $C_{31}H_{42}N_5O_4S$ (M+H)$^+$: 582.30, found 582.30. ^{1}H NMR (500 MHz, CDCl$_3$, 25 °C): δ 8.10 (s, 2H), 7.54 (d, *J* = 8.2 Hz, 2H), 7.22 (d, *J* = 7.9 Hz, 2H), 3.70 (s, 4H), 3.70 (s, 6H), 3.01 (d, *J* = 8.4 Hz, 8H), 2.62 (s, 4H), 2.38 (s, 3H), 2.28 (s, 6H), 2.21 (s, 6H).

3.3.3 Synthesis of *N, N'*-di(4-hydroxy-3,5-dimethyl-2-picoyl)- 1,4,7-triazacyclononane.
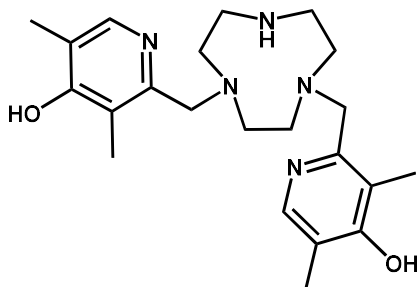
N, N'-di(4-methoxy-3,5-dimethyl-2-picoyl)-*N''*-monotosyl-1,4,7-triazacyclononane (1.9 g, 3.3 mmol) and a magnetic stir bar were introduced into a 25 mL round bottom flask. To this, concentrated H_2SO_4 solution (10 mL) was slowly added and the resulting orange-yellow mixture was placed under vacuum for 1 h to remove all traces of oxygen. Afterwards, the reaction flask was connected to a reflux condenser and the homogeneous orange solution was heated to 160 °C under a dinitrogen atmosphere with stirring temperature for 16 h. The resulting black reaction mixture was cooled to room temperature and then added to stirring EtOH (60 mL) at −20 °C. Subsequent addition of Et_2O (300 mL) resulted in the formation of a pale brown suspension, which was filtered to give a black hygroscopic solid. The solid was dissolved in saturated aqueous K_2CO_3 solution (10 mL) and EtOH (200 mL) was added to create a biphasic mixture, which was stirred at 25 °C for 30 min. The EtOH layer was collected and filtered to give an orange solution which was evaporated to dryness to give an orange oil. The crude product was dissolved in MeCN (50 mL) and concentrated AcOH solution (1 mL) was added to generate the neutral species. The resulting solution was evaporated to dryness to give a mixture of brown oil and a white crystalline solid. This mixture was triturated with CH_2Cl_2 (100 mL) and the supernatant was filtered and evaporated to dryness to give the product as an orange oil (0.75 g, 1.9 mmol, 58%). ESI-MS (*m/z*): Calcd. for $C_{22}H_{33}N_5O_2$ (M+H)$^+$: 400.27, found 400.28. ^{1}H NMR (500 MHz, CD_3OD, 25 °C): δ 7.49 (s, 2H), 3.65 (s, 4H), 2.91 − 2.76 (m, 8H) 2.47 (broad s, 4H), 1.97 (s, 6H), 1.96 (s, 6H).

3.3.4 Synthesis of *N, N'*-di(4-hydroxy-3,5-dimethyl-2-picoyl)-*N''*-mono(3-fluoro-6-methyl-2-picolyl)-1,4,7-triazacyclononane (LH$_2$)
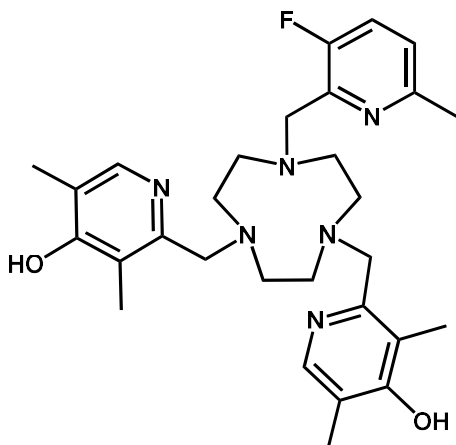
N,   N'-di(4-hydroxy-3,5-dimethyl-2-picoyl)-1,4,7-triazacyclononane (0.75 g, 1.9 mmol) and 3-fluoro1-2-formyl-6-methylpyridine (0.28 g, 2.0 mmol) were added to a 100 mL Schlenk flask in a dinitrogen atmosphere glove box. To this, dry CH$_2$Cl$_2$ (40 mL) was added and the flask sealed with a septum. This yellow solution was stirred at 40 °C for 1 h in the glove box. Next, solid NaHB(OAc)$_3$ (1.3 g) was added and the reaction was followed by ESI-MS. After stirring for 1 h, the reaction was 85% complete and did not improve upon further heating. Therefore, the reaction mixture was cooled to room temperature, brought out of the glove box, and quenched with concentrated aqueous K$_2$CO$_3$ solution (20 mL). The resulting solution was extracted with CH$_2$Cl$_2$ (3 × 50 mL). The organic layers were collected, dried with MgSO$_4$(s), and filtered. The solvent was removed under reduced pressure to give a pale yellow powder. This powder was dissolved in MeCN (4 mL) and concentrated AcOH solution (1 mL) was added. This solution was evaporated to dryness to give an orange oil which was triturated with CH$_2$Cl$_2$ (5 mL) and filtered through diatomaceous earth. The filtrate was evaporated to dryness to give the crude product as a yellow solid. The ligand was purified by column chromatography using aluminum oxide basic and 0–10% H$_2$O in MeCN as eluent. The ligand was obtained as a yellow solid after removing the solvent under reduced pressure (0.12g, 0.22 mmol, 12%). ESI-MS (*m/z*): Calcd. for C$_{29}$H$_{39}$FN$_6$O$_2$ (M+H)$^+$: 523.32, found 523.33. ^{1}H NMR (500 MHz, CDCl$_3$, 25 °C):

δ 7.29 (s, 2H), 7.24 – 7.13 (m, 1H), 6.99 (dd, J = 8.5, 3.6 Hz, 1H), 3.83 (s, 2H), 3.64 (s, 4H), 2.87

– 2.76 (m, 4H), 2.72 – 2.65 (m, 4H), 2.62 (s, 4H), 2.34 (s, 3H), 1.95 (s, 6H), 1.94 (s, 6H). ^{19}F NMR

(376 MHz, CDCl$_3$, 25 °C): δ −129.91 (d, J = 7.2 Hz).

3.3.5 Synthesis of [(LH$_2$)Fe](BF$_4$)$_2$.

Under an inert atmosphere of dinitrogen, a pale pink suspension of [Fe(H$_2$O)$_6$](BF$_4$)$_2$ (0.097 g,

0.29 mmol) in MeCN (2 mL) was added dropwise to a stirring light orange solution of LH$_2$ (0.15

g, 0.29 mmol) in MeCN (6 mL). The resulting dark green solution was stirred at ambient

temperature for 3 h and then filtered. The dark green filtrate was concentrated under reduced

pressure to give a dark green-brown film. This film was dissolved in deionized H$_2$O at 60 °C and

upon cooling to room temperature, light green-yellow crystalline solid formed. This solid was

washed with cold deionized H$_2$O (1 mL) and dried under vacuum for 16 h to give the title

compound (0.11 g, 0.15 mmol, 52%). Anal. Calcd. for C$_{29}$H$_{39}$B$_2$F$_9$FeN$_6$O$_2$: C, 46.31%; H, 5.23%;

N, 11.17%. Found: C, 45.79%; H, 5.33%; N, 11.17%. Yellow-green block-shaped crystals of

[(LH$_2$)Fe](BF$_4$)$_2$ suitable for X-ray diffraction analysis were grown by slow cooling of a

concentrated H$_2$O solution of the compound.

3.3.6 X-ray Structure Determination.

Single crystals of [(LH$_2$)Fe](BF$_4$)$_2$ were directly coated with deoxygenated Paratone-N oil,

mounted on a MicroMounts rod and frozen under a stream of dinitrogen during data collection.

Crystallographic data were collected at 100 K using a Bruker Kappa Apex II diffractometer

equipped with a Triumph detector, a MoKα source, and MX Optics. Raw data were integrated and

corrected for Lorentz and polarization effects with SAINT v8.27B.[108] Absorption corrections were

applied using SADABS.[109] Space group assignments were determined by examination of

systematic absences, E-statistics, and successive refinement of the structures. Structures were solved with SHELXT [110] and further refined with SHELXL [111] operated within the OLEX2 interface.[112] Positional disorder of the $(BF_4)^-$ anions was modeled with partial occupancies. All non-acidic hydrogen atoms were placed at calculated positions using suitable riding models and refined using isotropic displacement parameters derived from their parent atoms. The hydroxylpyridine protons were found in the Fourier difference map and were freely refined. Thermal parameters were refined anisotropically for all non-hydrogen atoms. Crystallographic data and the details of data collection are listed in Table 3.1.

3.3.7 Solution magnetic measurements.

The solution magnetic moments of $[(LH_x)Fe]^{x+}$ were determined using the Evans method,[113] by collecting variable-temperature ^1H NMR spectra using an Agilent DD2 500 MHz (11.7 T) spectrometer. Samples for measurements were prepared according to the following protocol. A 50 μL aliquot of a 14.0 mM stock solution of $[(LH_2)Fe](BF_4)_2$ in deoxygenated H_2O was dissolved in 0.45 mL of deoxygenated 100 mM phosphate buffer solutions containing 2% (v/v) dimethylsulfoxide (DMSO) as a reference. The pH of the phosphate buffer solutions ranged from 5.4 to 7.8. Blank samples containing 50 μL water and 0.45 mL of the same DMSO/phosphate buffer solutions were also created for each pH value. The samples were added to NMR tubes equipped with flame-sealed capillaries containing 2% (v/v) TFA and 5% (v/v) DMSO in D_2O reference solutions. The frequency differences of the DMSO resonance in the sample and reference solutions from the blank samples were subtracted from the analogous DMSO frequency differences of the $[(LH_2)Fe](BF_4)_2$ samples. The average of three measurements afforded the resulting data. All data were corrected for diamagnetic contributions (determined from elemental

analysis) from the core diamagnetism of each sample (estimated using Pascal's constants).[114] The paramagnetic molar susceptibility χ_M^{para} (cm^3 mol^{-1}) was calculated using the following equation: [113]

$$\chi_M^{para} = (3\Delta\nu M_w)/(4\pi\nu_0 m) - \chi_M^{dia} \tag{1}$$

In this equation, $\Delta\nu$ is the frequency difference (Hz) between the *tert*-butyl resonance of *tert*-butanol in the sample and reference solutions, M_w is the molecular mass of the paramagnetic compound (g mol^{-1}), ν_0 is the operating frequency of the NMR spectrometer (Hz), m is the concentration of the paramagnetic compound (g cm^{-3}), and χ_M^{dia} is the diamagnetic contribution to the molar susceptibility (cm^3 mol^{-1}).

3.3.8   NMR spectroscopy.

^{1}H and ^{19}F NMR spectra of ligand LH$_2$ and ligand precursors were collected at 25 °C on either an Agilent DD2 500 MHz (11.7 T) system, at 500 and 470 MHz frequencies respectively, or on an automated Agilent DD MR 400 MHz (9.40 T) system equipped with Agilent 7600 96-sample autosampler, at 400 and 376 MHz frequencies respectively. Variable-temperature ^{19}F NMR spectra of [(LH$_2$)Fe](BF$_4$)$_2$ were collected on an Agilent DD2 500 MHz (11.7 T) system at 470 MHz. NMR spectra of samples in 100 mM phosphate buffer solutions containing 2% (v/v) DMSO at various pH values were acquired using 1% solutions of trifluoroacetic acid (TFA) in D$_2$O in an inner capillary to lock the sample. Chemical shift values (δ) are reported in ppm and referenced to residual proton signals from the deuterated solvents for all ^{1}H NMR spectra (7.26 ppm for CDCl$_3$ and 3.31 ppm for CD$_3$OD). ^{19}F NMR chemical shift values for spectra recorded in CDCl$_3$ were referenced to trichlorofluoromethane (CFCl$_3$) at 0 ppm. For variable-pH NMR spectra of

$[(LH_x)Fe]^{x+}$ in 100 mM phosphate buffer solutions, the ^{19}F NMR chemical shift values are referenced to TFA at 0 ppm. All coupling constants (J) were measured in Hertz (Hz). The MestReNova 10.0 NMR data processing software was used to analyze and process all recorded NMR spectra.

3.3.9   UV-Visible absorption measurements.

UV-Visible experiments were carried out on an Agilent Cary 5000 UV-Vis-NIR spectrometer. Spectra were collected in the 200–800 nm range for 70 μM samples of $[(LH_x)Fe]^{x+}$ in 100 mM phosphate buffer solutions containing 2% (v/v) DMSO at various pH values.

3.4   RESULTS AND DISCUSSION
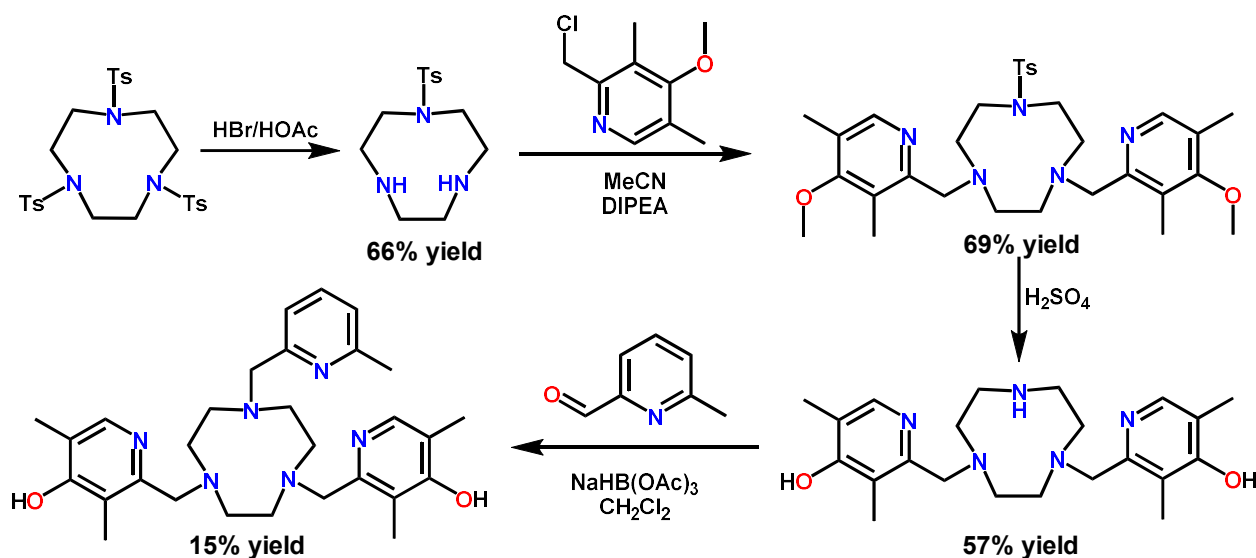
Figure 3.2 | Synthesis of ligand LH₂.

3.4.1   Synthesis and X-Ray Crystallography.

The ligand LH_2 was prepared following a four-step synthesis outlined in Figure 3.2. Incorporation of two 4-methoxy-3,5-dimethyl-2-picolyl donors onto a tosylated 1,4,7-triazacyclononane

(TACN) macrocycle via nucleophilic substitution reaction, followed by deprotection with H_2SO_4 and reductive amination with 3-fluoro-6-methyl-2-pyridinecarboxaldehyde, afforded LH_2 as a yellow solid. Under anaerobic conditions, reaction of LH_2 with one equivalent of $[Fe(H_2O)_6](BF_4)_2$ in MeCN yielded a green-brown film. Subsequent trituration with CH_2Cl_2 and THF, followed by slow cooling of an aqueous solution, afforded yellow-green block-shaped crystals of $[(LH_2)Fe](BF_4)_2$ (**3**).

Single-crystal X-ray diffraction analysis for **3** was carried out at 100 K (see Figure 3.3 and Table 3.1). The compound crystallized in the orthorhombic space group *Pbca*, with one $[(LH_2)Fe]^{2+}$ cation and two $[BF_4]^-$ anions in the asymmetric unit. The two acidic protons on the hydroxylpyridine moieties were located in the Fourier difference map and were freely refined. The coordination environment at the Fe^{II} center in $[(LH_2)Fe]^{2+}$ is highly distorted from octahedral geometry. The Fe–N bond distances range from 2.109(5) to 2.223(5) Å with an average distance of 2.165(5) Å, and the N–Fe–N angles range from 75.1(2) to 111.3(2)° with an average angle of 90.8(2)°. These structural metrics indicate the presence of high-spin Fe^{II} in the solid state at 100 K. Considering the observation of low-spin Fe^{II} in related compounds at 100 K, [7b,115] we surmise the high-spin Fe^{II} in **3** likely results from crystal packing effects.

Table 3.1 | Crystallographic data for [(LH$_2$)Fe](BF$_4$)$_2$.

Empirical formula	C$_{29}$H$_{39}$B$_2$F$_9$FeN$_6$O$_2$
Formula weight, g mol^{-1}	752.13
Temperature, K	100.0
Crystal system	Orthorhombic
Space group	*Pbca*
a, Å	15.049(11)
b, Å	14.809(10)
c,Å	29.11(2)
α ,°	90
β, °	90
γ, °	90
V, Å^3	6486(8)
Z	8
ρ_{calc}, g cm^{-3}	1.540
μ, mm^{-1}	0.556
F(000)	3104.0
Crystal size, mm^3	0.256 × 0.103 × 0.076
Radiation	MoKα (λ = 0.71073 Å)
Reflections collected	51003
Independent reflections	5963 [R_{int} = 0.0720, R_{sigma} = 0.0415]
Goodness-of-fit on F^2	1.032
Final R indexes (*I* > 2σ(*I*))	R_1 = 0.0786,[a] wR_2 = 0.1887 [b]
Final R indexes (all)	R_1 = 0.1199,[a] wR_2 = 0.2141[b]
Largest diff. peak/hole, e$^-$ Å^{-3}	1.36 / −0.61

3.4.2 UV-Visible Absorption Measurements.

We next examined the effects of pH on the electronic structure of **3** in aqueous solution. UV-Visible absorption spectra were collected in 100 mM phosphate buffer solutions containing 2% (v/v) DMSO between pH 5.39 and 7.94 at 25 °C (see Figure 3.4). At pH 7.94, the UV-Vis spectrum displays an intense absorption band at 271 nm (ε_{max} = 27,000 M^{-1} cm^{-1}) and three less intense bands at 334 (ε_{max} = 2,300 M^{-1} cm^{-1}), 416 (ε_{max} = 960 M^{-1} cm^{-1}), and 453 nm (ε_{max} = 1,200 M^{-1} cm^{-1}). We assign these features to $\pi-\pi^*$ and metal-ligand charge transfer (MLCT) transitions, respectively, as observed in similar compounds.[115,116] As the pH was decreased to 5.39, the intensity of the $\pi-\pi^*$ absorption decreased (ε_{max} = 12,000 M^{-1} cm^{-1}), while the intensities of the MLCT bands increased significantly with a concomitant shift to 383 (ε_{max} = 2,800 M^{-1} cm^{-1}) and 451 nm (ε_{max} = 1,600 M^{-1} cm^{-1}). This increase in MLCT band intensity with decreasing pH suggests that the low-spin state becomes more populated when the ligand is fully protonated.[92a,117] Furthermore, the presence of two isosbestic points at 325 and 472 nm indicates an equilibrium between different protonation states of $[(LH_x)Fe]^{x+}$ (x = 0–2) in the biological pH range.
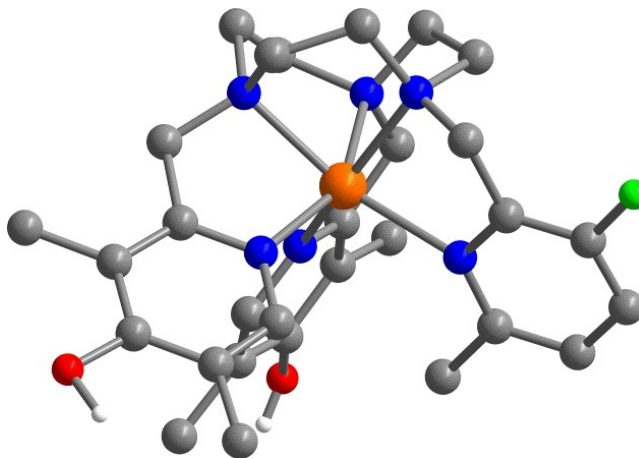
Figure 3.3 | Crystal structure of the complex cation in **1**. Orange, green, red, blue, gray, and white spheres represent Fe, F, O, N, C, and H atoms respectively; non-hydroxyl H atoms are omitted for clarity.
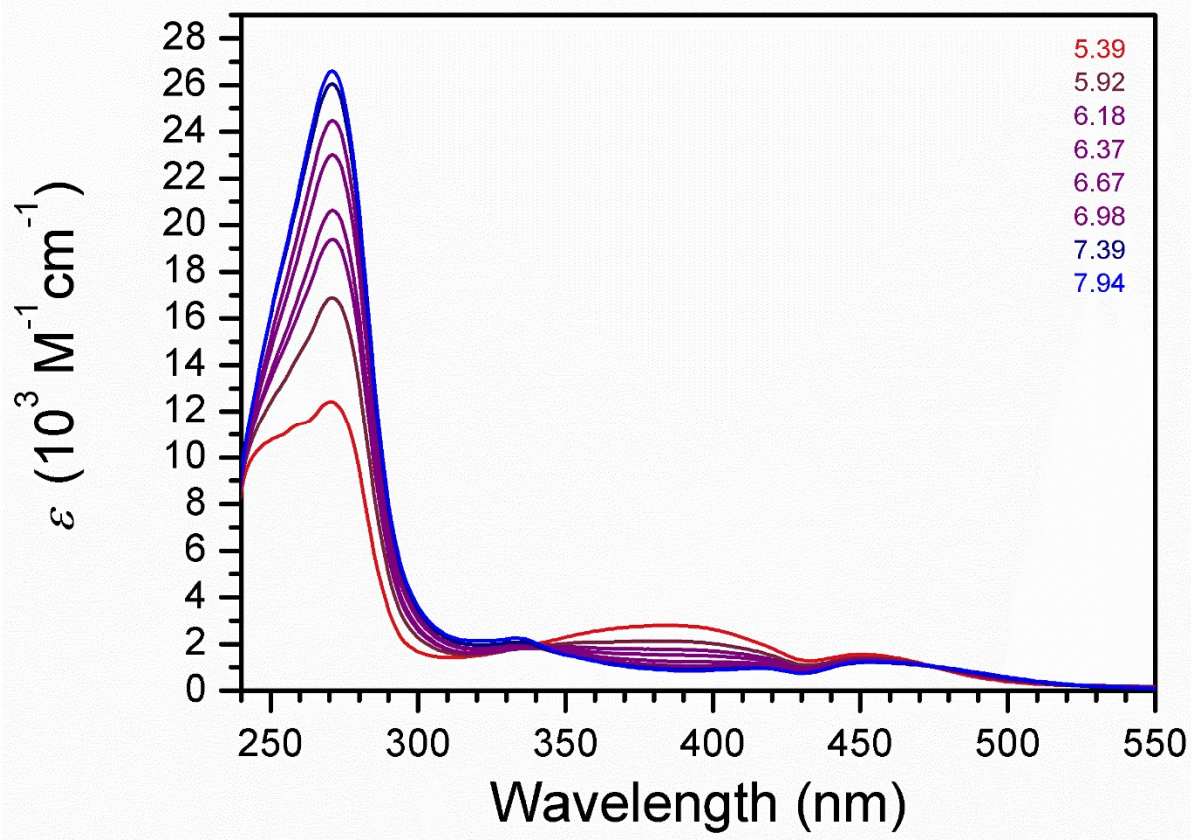
Figure 3.4 | Variable-pH UV-Vis spectra for $[(LH_x)Fe]^{x+}$ in 100 mM phosphate buffer solutions containing 2% (v/v) DMSO. Spectra were measured at 25 °C in the pH range 5.39–7.94. Colored numbers in the legend denote the pH of the solutions measured with a pH electrode.

3.4.3   Solution-Phase Magnetic Susceptibility.

To probe the magnetic properties and solution electronic structure of **3** as a function of pH, variable-temperature dc magnetic susceptibility data were collected using the Evans method[113] in the temperature range 5–60 °C, in 100 mM phosphate buffer solutions with 2% (v/v) DMSO added as a reference (see Figure 3.5). At pH 4.74, the value of $\chi_M T$ increases with increasing temperature from 1.78(1) cm^3 K mol^{-1} at 5 °C to 2.40(1) cm^3 K mol^{-1} at 60 °C. This temperature dependence indicates the presence of thermally-induced spin-crossover, with significant population of both an $S = 0$ ground state and $S = 2$ excited state in this temperature range. Assuming a value of $g = 2$ for

the $S = 2$ state, insertion into the Curie equation gives percentages of high-spin molecules (%HS) of 59% at 5 °C and 80% at 60 °C.[118] In contrast, the variable-temperature magnetic susceptibility for an analogous solution of **3** at pH 7.82 show much less temperature dependence. Here, $\chi_M T$ increases only slightly with increasing temperature, from 2.62(1) $cm^3 K\ mol^{-1}$ at 5 °C to 2.70(1) $cm^3 K\ mol^{-1}$ at 60 °C, corresponding to %HS = 87% at 5 °C and 90% at 60 °C. We attribute this shift toward greater population of the $S = 2$ state with increasing pH to a decreased ligand field strength of L^{2-} vs H_2L, owing to the weaker π acidity of the latter.
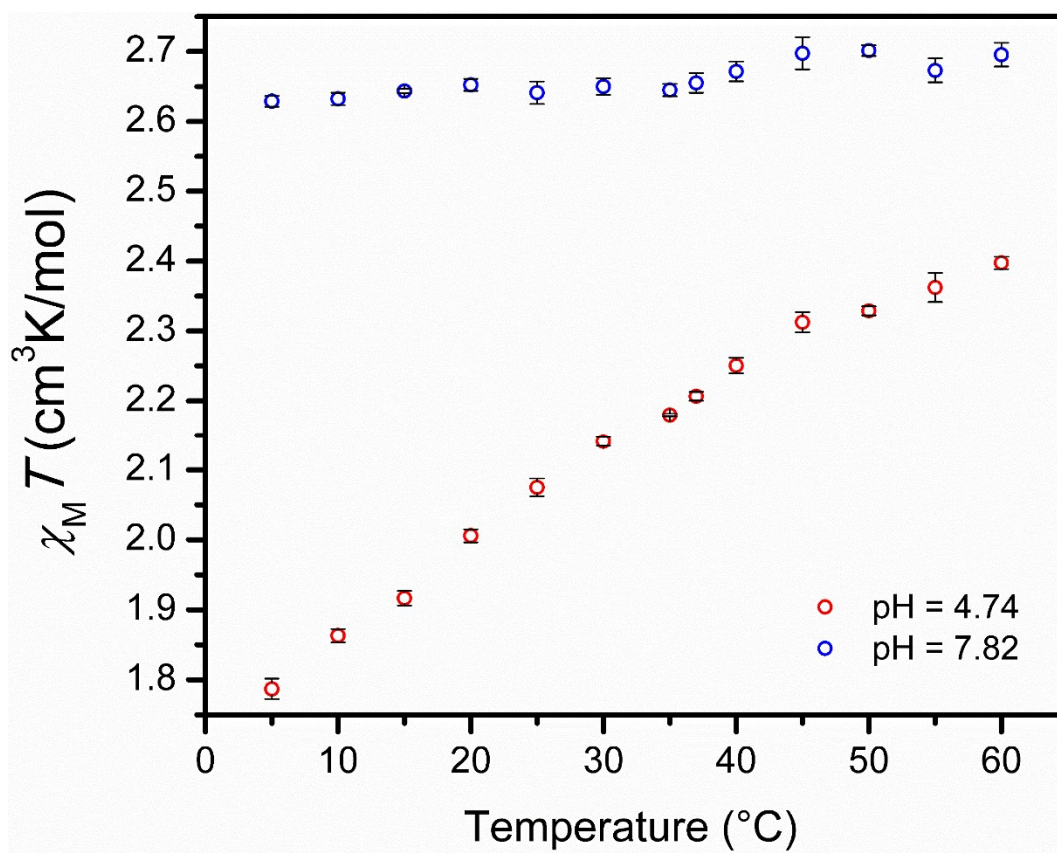
Figure 3.5 | Variable temperature Evans method magnetic susceptibility data for [(LH₂)Fe]²⁺ in a 100 mM phosphate buffer with 2% v/v DMSO at pH 4.74 and pH 7.82.

To further probe the pH dependence of the spin state of **3**, dc magnetic susceptibility data were collected as a function of pH at 25 and 37 °C (see Figure 3.6). At 25 °C, $\chi_M T$ rapidly increases

with increasing pH, from a value $\chi_M T = 2.07(1)$ cm^3 K mol^{-1} at pH 4.74 to $\chi_M T = 2.64(1)$ cm^3 K mol^{-1} at pH 7.82, corresponding to %HS = 69% at pH 4.74 and 88% at pH 7.82. The plot of $\chi_M T$ vs pH at 37 °C exhibits similar behavior, albeit with less pronounced pH dependence, where $\chi_M T$ increases from 2.20(1) cm^3 K mol^{-1} at pH 4.74 (%HS = 73%) to 2.65(1) cm^{3}K mol^{-1} at pH 7.82 (%HS = 88%). These results are in accord with the variable-pH behavior observed in the UV-Vis analysis described above, and confirm the pH dependence of the spin state population in **3**.
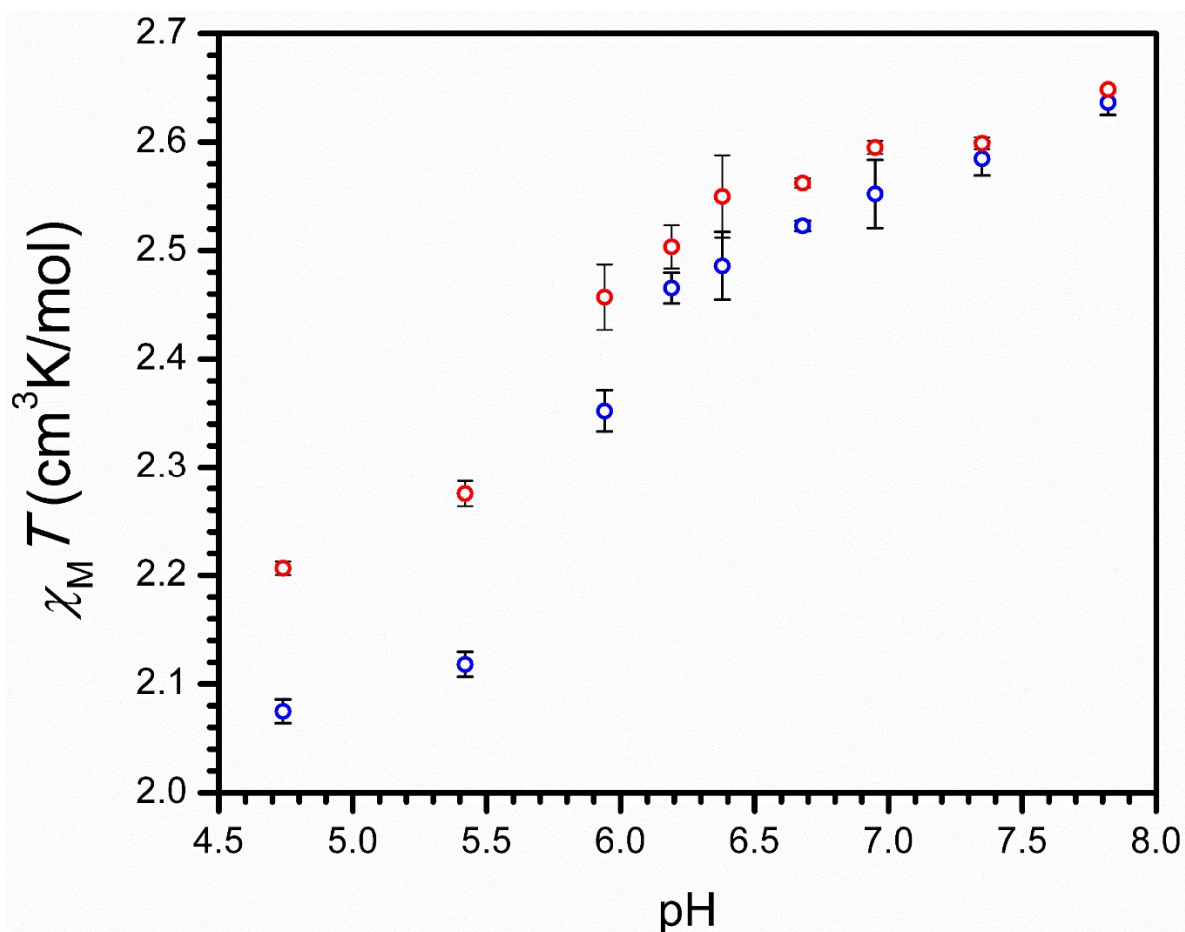
Figure 3.6 | Variable pH Evans method magnetic susceptibility data for [(LH$_2$)Fe]$^{2+}$ in a 100 mM phosphate buffer with 2% v/v DMSO at 25 °C (blue) and 37 °C (red).
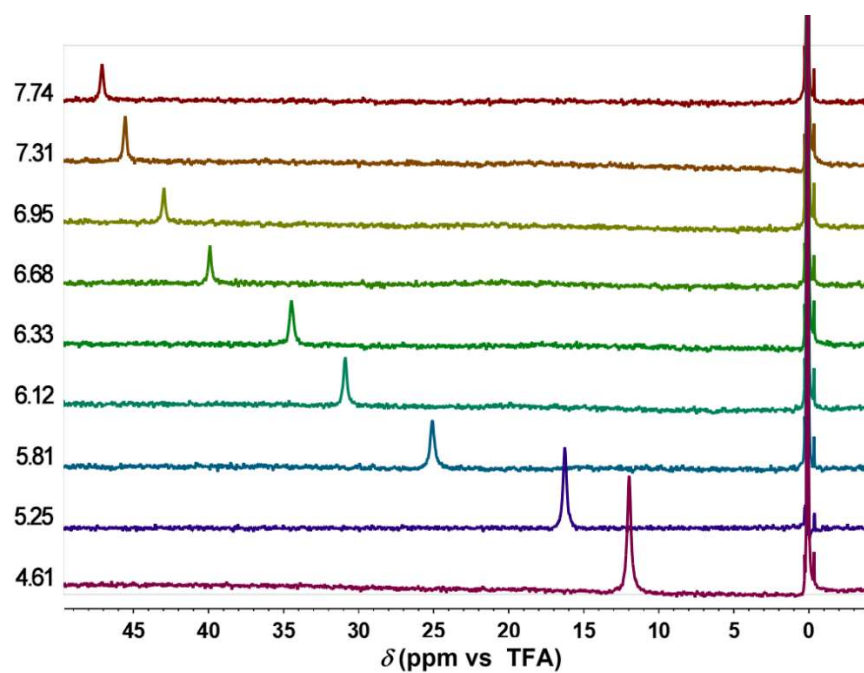
Figure 3.7 | | Variable-pH ^{19}F NMR spectra of [(LH$_x$)Fe]$^{x+}$ in 100 mM phosphate buffer solutions containing 2% (v/v) DMSO at 25 °C. The ^{19}F chemical shift of all spectra are referenced to TFA at 0 ppm. Black numbers on the left denote the pH of the solutions measured with a pH electrode.
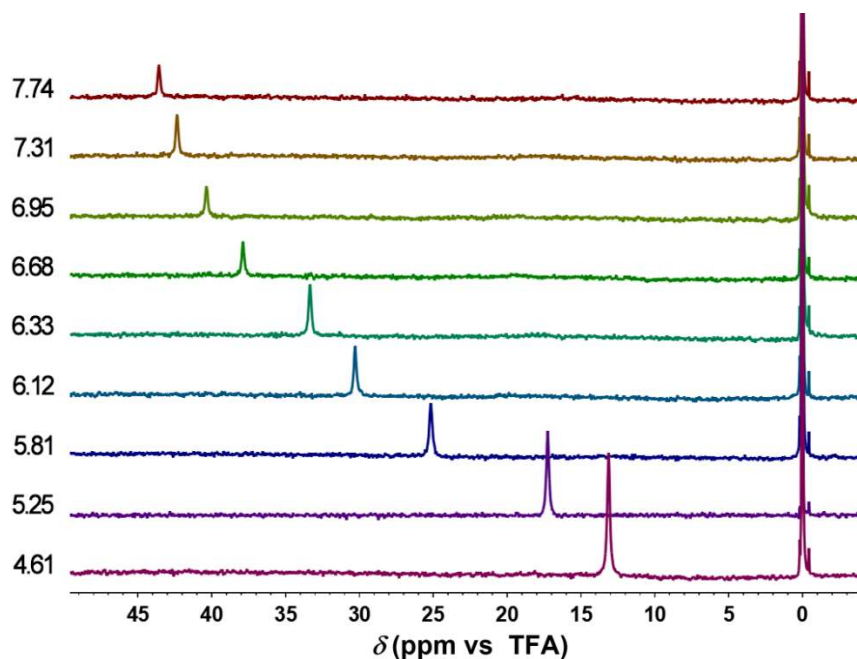
Figure 3.8 | Variable-pH ^{19}F NMR spectra of [(LH$_x$)Fe]$^{x+}$ in 100 mM phosphate buffer solutions containing 2% (v/v) DMSO at 37 °C. The ^{19}F chemical shift of all spectra are referenced to TFA at 0 ppm. Black numbers on the left denote the pH of the solutions measured with a pH electrode.

3.4.4 Variable-pH ^{19}F NMR Spectroscopy.

Finally, we aimed to determine the effect of the pH-dependent spin state population on the ^{19}F NMR resonance frequency of **3**. Variable-pH ^{19}F NMR spectra were collected on 2 mM solutions of **3** in 100 mM phosphate buffers with 2% (v/v) DMSO at 25 and 37 °C (see Figures 3.7 and 3.8). In the pH range 4.61–7.74, these spectra display a single ^{19}F resonance from the metalated ligand. At pH 4.61, when the hydroxylpyridine groups are predominantly protonated, the ^{19}F resonance appears at 11.89 ppm vs trifluoroacetic acid (TFA) at 25 °C. As the pH is increased, this resonance frequency shifts downfield, following sigmoidal behavior to a maximum value of 47.03 ppm at pH = 7.74. The data at 37 °C exhibit a similar pH profile, albeit with a slightly smaller pH dependence, where the ^{19}F chemical shift increases from 13.10 to 43.57 ppm from pH 4.61 to 7.74 (see Figure 3.9). These data were fitted to a Boltzmann sigmoidal function according to Equation 2:[119]

$$\delta = A_2 + (A_1 - A_2)/(1 + \exp((pH - pK_a)/dx)) \tag{2}$$
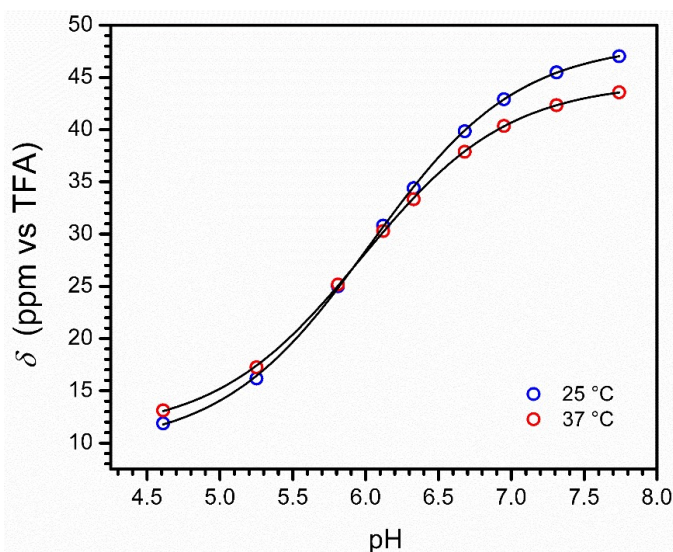
Figure 3.9 | Plot of variable pH ^{19}F NMR resonances of [(LH$_2$)Fe]$^{2+}$ in a 100 mM phosphate buffer with 2% v/v DMSO at 25 °C and 37 °C. All were spectra are referenced TFA which was set to 0 ppm.

Table 3.2 | Parameters obtained from sigmoidal fits of the ^{19}F chemical shift vs pH data for $[(LH_x)Fe]^{x+}$ to Equation 1

	25 °C	37 °C
Adj. R^2	0.99981	0.99988
A_1	9.5(3)	11.0(2)
A_2	48.3(2)	44.5(1)
pK_a	6.03(1)	5.97(1)
dx	0.51(1)	0.50(1)

where δ is the observed ^{19}F chemical shift, A_2 is the theoretical chemical shift of the fully deprotonated species, A_1 is the theoretical chemical shift of the fully protonated species, dx is a parameter describing the steepness of the curve, and pK_a is obtained as the inflection point of the curve. Fits to the data provided estimated pK_a values of 6.03(1) at 25 °C and 5.97(1) at 37 °C. Further, rearranging Equation 1 and inserting the values obtained from the sigmoidal fit of each curve (see Table 3.2) gives Equations 3 and 4 for the data at 25 and 37 °C, respectively, which relate chemical shift to pH:

$$pH = 6.03 + 0.51 \ln(-38.8 / (\delta - 48.3) - 1) \tag{3}$$

$$pH = 5.97 + 0.50 \ln(-33.6 / (\delta - 44.5) - 1) \tag{4}$$

In addition, by applying a linear fit to the data between pH 5.25 and 6.95, the change in ^{19}F chemical shift affords a pH sensitivity of 16.0(4) ppm per pH unit at 25 °C and 13.9(5) ppm per pH unit at 37 °C (see Figure 3.10). While this pH sensitivity may partially stem from electrostatic effects and/or small changes in geometry at Fe^{II} upon deprotonation, the dramatic change in ^{19}F resonance frequency with pH strongly resembles the variable-pH $\chi_M T$ data discussed above. This similarity suggests that the primary cause of the pH-induced change in ^{19}F resonance frequency is an increase in population of the $S = 2$ state owing to deprotonation of the hydroxylpyridine donors.
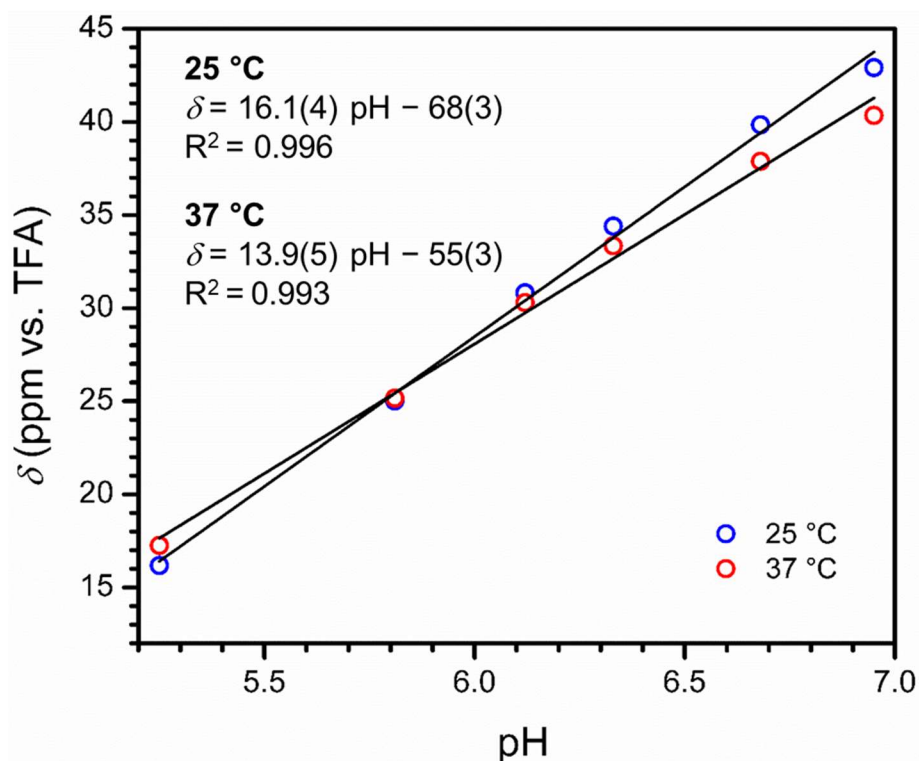
Figure 3.10 | pH dependence of the ^{19}F chemical shift of $[(LH_x)Fe]^{x+}$ vs TFA in 100 mM phosphate buffer solutions containing 2% (v/v) DMSO at 25 °C (blue) and 37 °C (red) between pH 5.25 and 6.95. Circles represent experimental data and black solid lines denote linear fits to the data (see equations on the graph).

3.5   Summary and Outlook

The foregoing results demonstrate the potential utility of a pH-induced spin state change for pH sensing using ^{19}F MRS. We show that a change in spin state upon deprotonation of $[(LH_2)Fe]^{2+}$ dramatically affects its ^{19}F resonance frequency, which can be employed to quantitate pH. Indeed, this complex displays greater pH sensitivity than the current most-sensitive lanthanide-based ^{19}F MRS sensors[101b] and the only reported transition metal-based ^{1}H MRS pH sensor.[120] To the best of our knowledge, $[(LH_2)Fe]^{2+}$ represents the first example of an ^{19}F MRS pH probe that employs a pH-induced spin state change. While the oxygen sensitivity of this compound precludes it from *in vivo* experiments, the principles outlined here could inform the design of resonance frequency-

based MR pH sensors. Future efforts will focus on developing similar compounds with higher stability under biological conditions.

4 Utilizing PARACEST NMR pH Sensors to Image Microbial-Induced Corrosion

4.1 Introduction

Microbial induced corrosion of fuels and materials poses a serious impediment to the operation and maintenance of the US Air Force fleet and its supporting infrastructure.[121] In particular, a number of corrosive microbes have been found to grow at the fuel-water interface in underground fuel storage tanks. These organisms consume alkanes in fuel, breaking down long-chain hydrocarbons into less combustible compounds, and releasing particulate matter into the fuels, which can interfere with engine performance.[122] Furthermore, as these organisms grow, they efflux protons, leading to acidification of the surrounding media, which can increase the rate of fuel and material corrosion.[123] While microbial acidification is a well-known phenomenon, quantitative, time resolved studies of microbial pH gradient formation are unreported in a many of the microbial species that are most responsible for corrosion of fuels and materials.

The lack of longitudinal pH studies on microbial induced corrosion is likely due to the difficulty of quantitatively measuring pH with high spatial and temporal resolution in living system. Traditional potentiometric pH
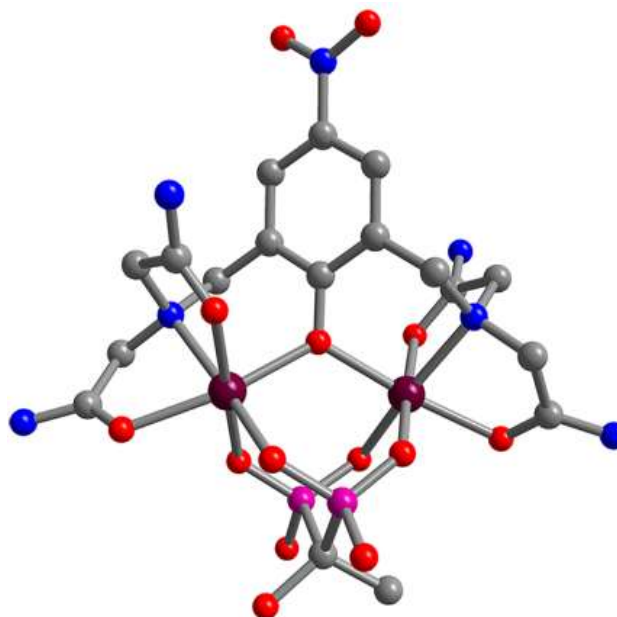
Figure 4.1 │ Crystal structure of Co$_2$. Purple, green, magenta, red, blue, and gray spheres represent Co, Cl, P, O, N, and C atoms, respectively; H atoms are omitted for clarity.
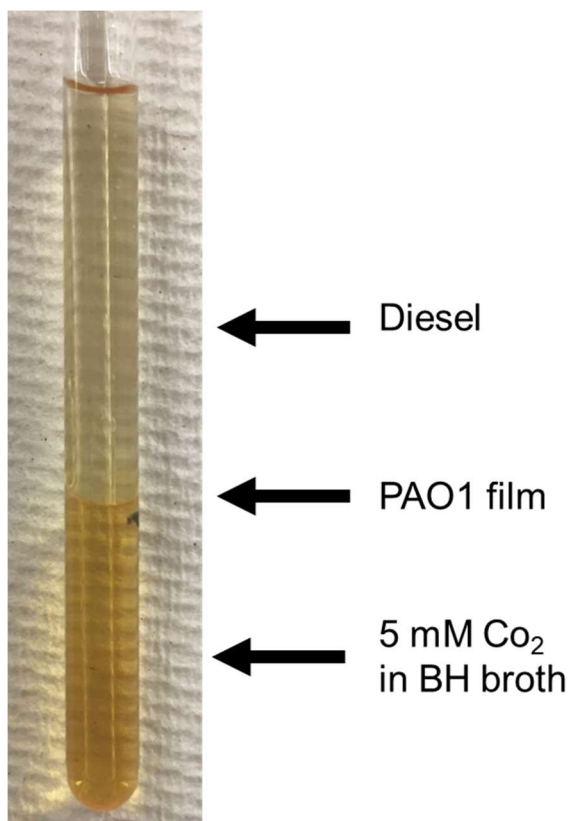
Figure 4.2 | Photograph of PAO1 biofilm sample growing at the interface of 5mM Co_2 in BH broth and biodiesel.

measurements rely on the use of point detecting pH probes, which do not provide spatial resolution and which necessarily disturb pH gradients upon insertion of the probe. Furthermore, fluorescence-based pH indicators cannot be easily used to due to significant background fluorescence from the microbial films.

Magnetic resonance imaging (MRI) could be an excellent candidate for measuring the pH of biofilms and their surrounding environment in three dimensions with excellent spatial resolution. Though the MR properties of water are necessarily pH dependent, the measurement of pH with MRI in biological systems commonly employs pH-sensing exogenous agents in order to obtain greater pH sensitivity.[124] Among these are paramagnetic chemical exchange saturation transfer (PARACEST) agents which generate image contrast *via* selective radiation of a proton on the contrast agent which is in exchange with bulk water.[125] PARACEST agents are particularly suited to measuring pH as the exchange rate of the contrast agent proton with the bulk water is inherently pH sensitive.[126] Our group has recently developed a highly pH-sensitive PARACEST probe, Co_2 (see Figure 4.1), which can be used to detect pH by measuring the ratio of the CEST intensity at 106 ppm vs 64 ppm.[127] The aim of this project is to use Co_2 to study the pH gradients

formed by living microbial films with high spatial resolution. By incubating these films in a solution of Co_2 we can monitor the pH gradient over time without disturbing the solution with the goal to learn more about the rate and mechanism of microbial acid metabolism.

While it would be ideal to measure these pH gradients in their natural environment, the MR imaging of an actual fuel tank system has several insurmountable problems, including the size and metal content of the fuel storage tanks. In this project, we will aim to recreate the fuel tank conditions on a much smaller scale, in an NMR tube (see Figure 4.2) Each sample will contain biodiesel layered on top of an aqueous solution of Co_2 and will be inoculated with a strain of bacteria or yeast that is known to grow biofilms on the fuel water interface of fuel storage tank. As these films grow, we will employ a technique called slice-selective NMR to measure the pH along the vertical axis of the NMR tube.[128] Slice-selective imaging is accomplished by applying a gradient pulse along the 1 cm active volume of the NMR coil. This changes the resonance frequency of the nuclei by changing he magnetic field as a function of position. By then applying a frequency-selective pulse, we can image a small slice of the NMR tube at various positions throughout the active volume of the NMR coil. While there are several reports of using slice-selective ^{1}H NMR to monitor reaction gradients, this technique has not yet been applied toward the study of microbes, nor has a pulse sequence yet been developed to allow for slice-selective PARACEST NMR. This chapter outlines the preliminary results of our PARACEST slice-selective imaging experiments and cell viability studies.

4.2   EXPERIMENTAL SECTION

4.2.1   General considerations.

All experiments were performed at the Air Force Research Lab in Dayton, OH. The synthesis of Co_2 was performed as previously described.[71] The preparation of all samples was performed in air at ambient temperatures unless otherwise stated. All materials for the preparation of microbial samples were autoclaved or sterilized with 70% isopropanol before inoculation.

4.2.2   Cell viability studies

Cells cultures of *Pseudomonas Protogens*, *Wickerhamomyces,* and *Candida Haemolens* were grown overnight in tryptic soy broth (TSB), diluted by 1:10,000 in TSB, then dispensed into microwell plates. Co_2 was added to the well in serial dilution so that the final concentration ranged from 5 to 0.005 mM. The plates were incubated at 27 °C then the absorption at 600 nm was measured using a plate reading UV-Vis spectrometer.

4.2.3   *In vitro* NMR sample preparation.

Co_2 was dissolved in BH broth to form a 5 mM solution. The pH was adjusted with HCl and NaOH to create samples at 5 different pH. These samples were then transferred to an NMR tube fitted with a D_2O-filled capillary.

4.2.4   Biofilm NMR sample preparation.

NMR tubes with 250 μL BH broth and 250 μL were inoculated with PAO1 allowed to grow at 27 °C for 24 days and formed a film at the fuel/water interface. A 13 in. long Pasteur pipet was used to remove the BH broth solution, which was replaced with 250 μL of 5 mM Co_2 in BH broth and

a D_2O capillary was added. A long pipet was used to ensure that the film settled at the fuel-water interface. After the initial slice-selective experiment, the PAO1-Co$_2$ samples were stored in a 27 °C incubator.

4.2.5   NMR CEST spectroscopy.

CEST experiments were carried out on an Bruker 400 MHz (9.4 T) spectrometer at 37 °C. Z-spectra (CEST spectra) were obtained according to the following protocol: ^{1}H NMR spectra were acquired from −130 to 130 ppm with a step increase of 1 ppm using a presaturation pulse applied for 2 s at a power level (B_1) of 13.8 μT. D_2O was placed in an inner capillary within the NMR sample tube to lock the sample. The normalized integrations of the H_2O signal from the obtained spectra were plotted against frequency offset to generate a Z-spectrum.
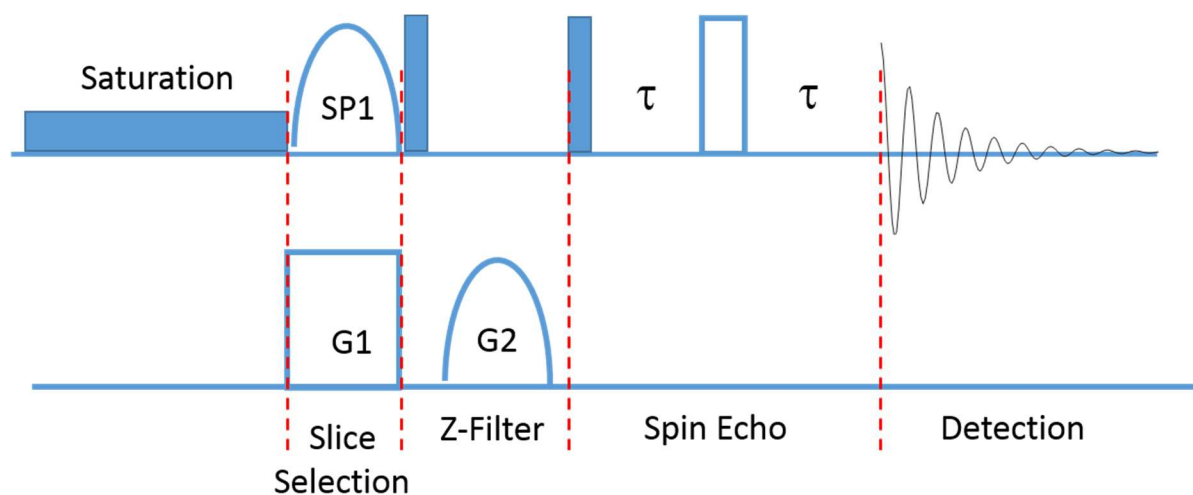
Figure 4.3 | The pulse sequence diagram for PARACEST with slice-selective imaging, a z-filter and spin-echo detection.

4.2.6   Slice-selective CEST imaging.

Slice-selective CEST experiments were carried out on an Bruker 400 MHz (9.4 T) spectrometer using similar samples as described above. The pulse sequence is outlined in Figure 4.3. First, a 2

s, 30 µT presaturation pulse was applied to the whole sample volume. Slice selection was accomplished by applying a 90° Gaussian cascade pulse[129] concurrently with a rectangular gradient pulse with a power of 10.5 G/cm. A non-selective 90° pulse was used to tip the magnetization along the –z axis and any residual signals or out-of-phase signals are removed with a 1 ms gradient pulse (7 G/cm). The signal was then detected with a spin echo. The normalized integrations of the H_2O signal from the obtained spectra were plotted against frequency offset to generate a Z-spectrum.

4.3   RESULTS AND DISCUSSION

4.3.1   PARACEST Titration Curve in Busnell-Haas (BH) Broth

In order to measure the pH gradients of bacteria growing in NMR tubes, we must first ensure that Co_2 demonstrates the same variable pH behavior in the microbe growth medium as it does in tris buffer. Bushnell-Haas (BH) broth is a minimal growth medium that provide only essential inorganic minerals to a microbial culture. In our experiment, BH broth also mimics the composition of water that leaches into fuel storage tanks. Since the small amount of paramagnetic $FeCl_3$ in the broth could change the chemical shift and electronic relaxation time of Co_2 and water protons, it was necessary to perform a control CEST titration experiment. A 5 mM solution of Co_2 in BH broth was titrated with 1 M HCl solution and the CEST spectra were collected between pH 6.31 and 7.15 (see Figure 4.4). As expected from our previous studies in tris buffer,[92a] the CEST peak at 65 ppm increased with pH while the peak at 106 demonstrated the opposite behavior. Taking the $\log_{10}$ of the ratio between these peaks vs pH gives a linear curve, which has the same slope as the data in tris buffer (see Figure 4.5). This experiment confirms that our compound does
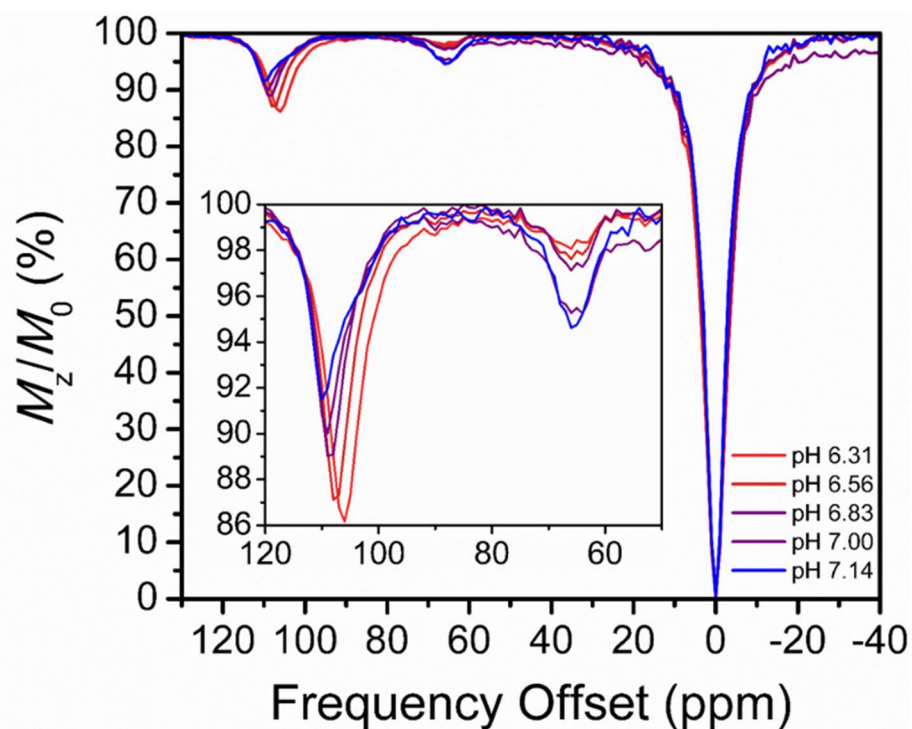
Figure 4.4 | Variable pH CEST spectra of 5 mM Co_2 in BH broth
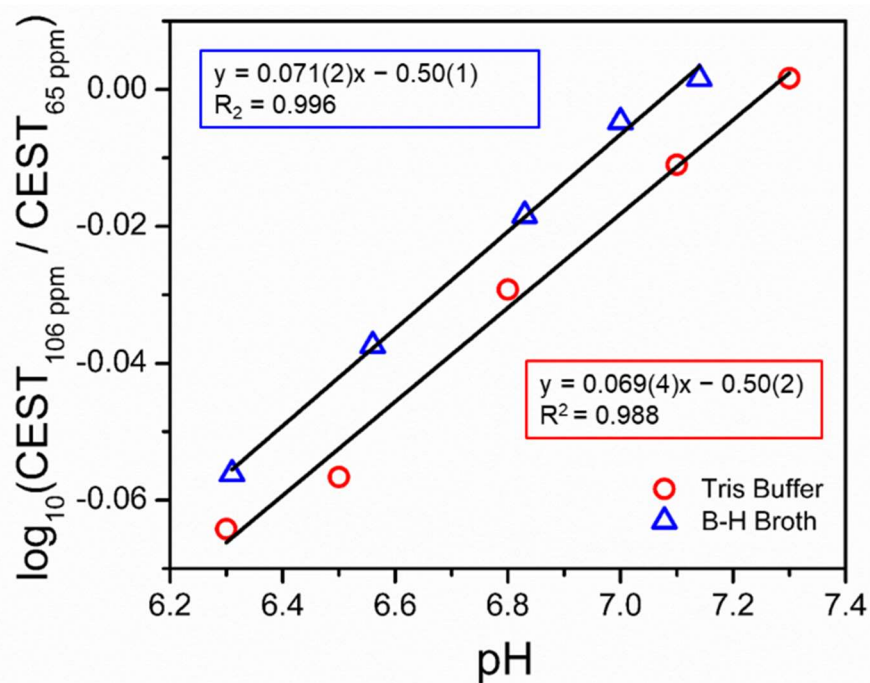
Figure 4.5 | Log_{10} of CEST peak ratio vs pH. Data were collected in BH broth and tris buffer demonstrate nearly identical variable pH behavior.

indeed have the same sensitivity in BH broth and is a good candidate for imaging experiments on biofilms.

As an initial test of PARACEST imaging, a pH gradient was prepared by layering a pH 4 solution of Co_2 in Busnell-Haas (BH) broth on the top of a similar pH 7 solution in a 5 mm NMR tube and PARACEST spectra were acquired for 2 slices (see Figure 4.6). While some spectrometer issues led to unusual noise in the spectra, there is a clear difference between the spectrum acquired at the center of the probe (blue) and the spectrum taken slightly above (green). Taking the ratio between the peaks at 106 and 65 ppm at $z = 0$ gives an approximate pH of 7.0. The offset spectrum, on the other hand, shows no signal intensity at 65 ppm, corresponding to a pH of less than 6. The collection of slices at other off sets on this sample was attempted, but fast diffusion of the acidic and basic solutions gave identical spectra for each slice. This experiment needs to be repeated using layered agar samples slow down diffusion.
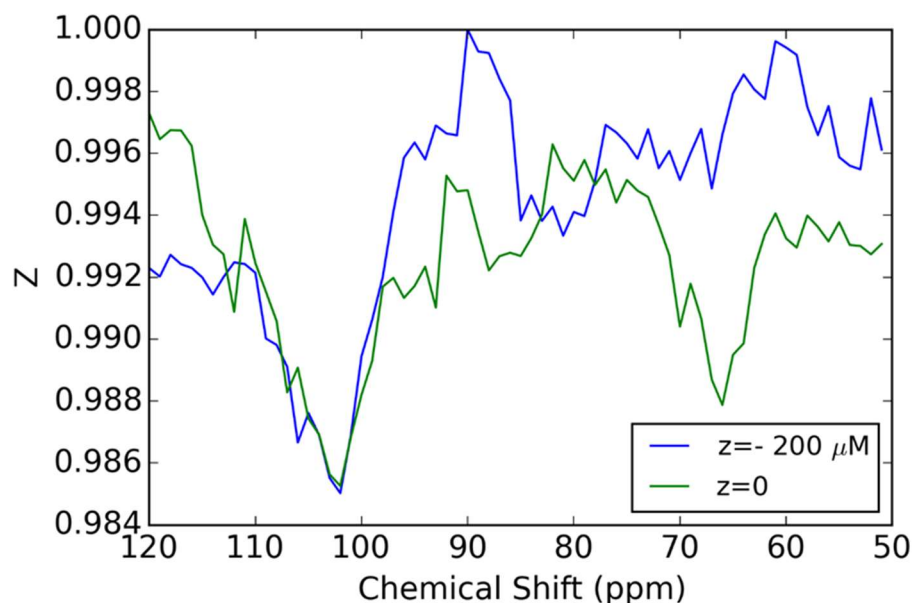
Figure 4.6 | PARACEST spectra collected via slice selective imagining of an artificial pH gradient made by layering pH 4 and pH 7 solutions of Co_2.

4.3.2 Cell Viability Studies

Cell viability studies were performed on three microbial strains. Cell cultures of *Pseudomonas Protogens*, *Wickerhamomyces,* and *Candida Haemolens* were diluted in tryptic soy broth (TSB) and dispensed into microwell plates. CO_2 was then added in concentration of 0–10 mM. and the cells were incubated in at 27 °C. Growth

Figure 4.8 | OD600 cell viability studies of *Pseudomonas Protogens* in TSB broth with CO_2.

was estimated by measuring optical density (OD) at 600 nm. The results of these studies are shown in Figures 4.7–4.8. CO_2 was best tolerated by the bacterial microbe, *Pseudomonas Protogens* (Figure 4.8). After 24 h, the OD 600 studies showed ~50% less biomass than the control cells.
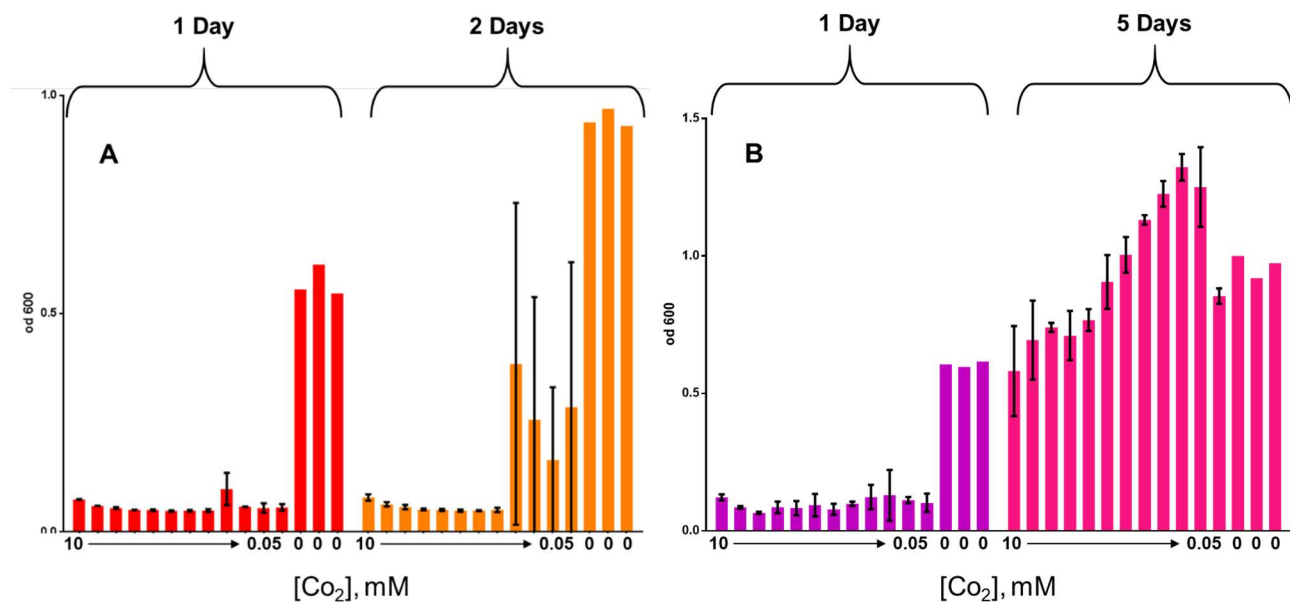
Figure 4.7 | OD600 cell viability studies of fungal strains in TSB broth with CO_2. A) *Wickerhamomyces* B) *Candida haemolens*.

Similar behavior was observed in another bacterial strain, PAO1. Co_2 also slowed the growth of two yeast strains, *Wickerhamomyces* and *Candida Haemolens* (Figure 4.7). While OD 600 studies show almost no growth for these organisms with any concentration of Co_2, the amount of biomass increased to near control levels after several days. Over all, these studies suggest that cell metabolism is active in the presence of Co_2 and will likely generate a pH gradient during imaging experiments.
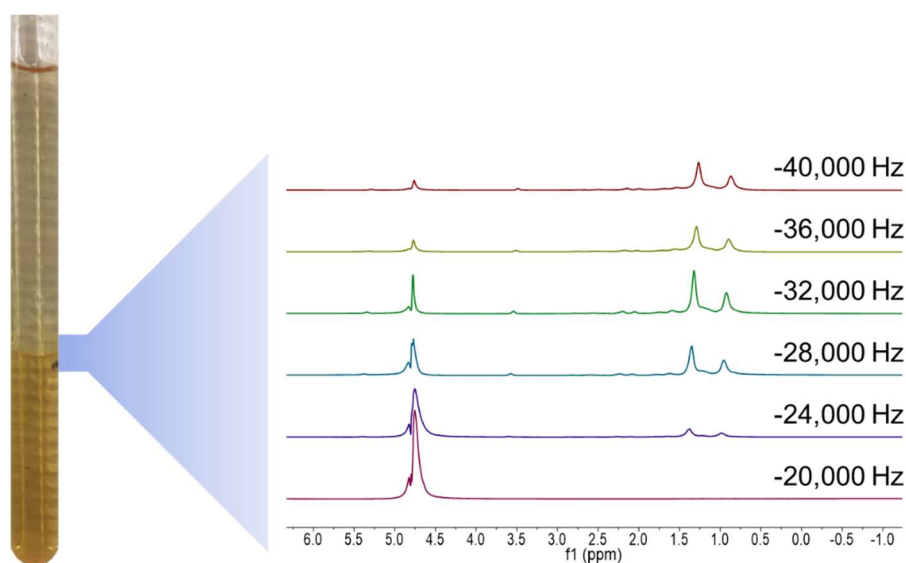
Figure 4.9 | Slice-selective ^1H NMR spectra of biofilm growing in a fuel/BH broth mixture. Numbers on the right indicate the offset frequency of the slice secretive pulse.

4.3.3 Biofilm Imaging Experiments.

Given the success of our biocompatibility studies and CEST experiments in BH broth, we next attempted chemical shift imaging experiments on a *pseudomonas aeruginosa* (PAO1) biofilm sample. These films were grown in NMR tubes in a biphasic solution of BH broth and biodiesel. To perform PARACEST imaging, the BH broth in each sample was removed and replaced with a pH = 7 solution of 5mM Co_2 in BH broth such that the biofilm and the aqueous/organic interface was centered near the middle of the active volume of the NMR probe. The fuel water interface was

located in the spectrometer by taking a series of ^{1}H spectra at locations along the NMR tube and comparing the intensity between the water peak (4.5 ppm) and the two broad fuel signals at 0.9 and 1.3 ppm. As the slice-selective pulse frequency offset was scanned from -40,000 Hz to -20,000 Hz, the intensity of the aliphatic resonances decreased while the H_2O intensity increased (see Figure 4.9).
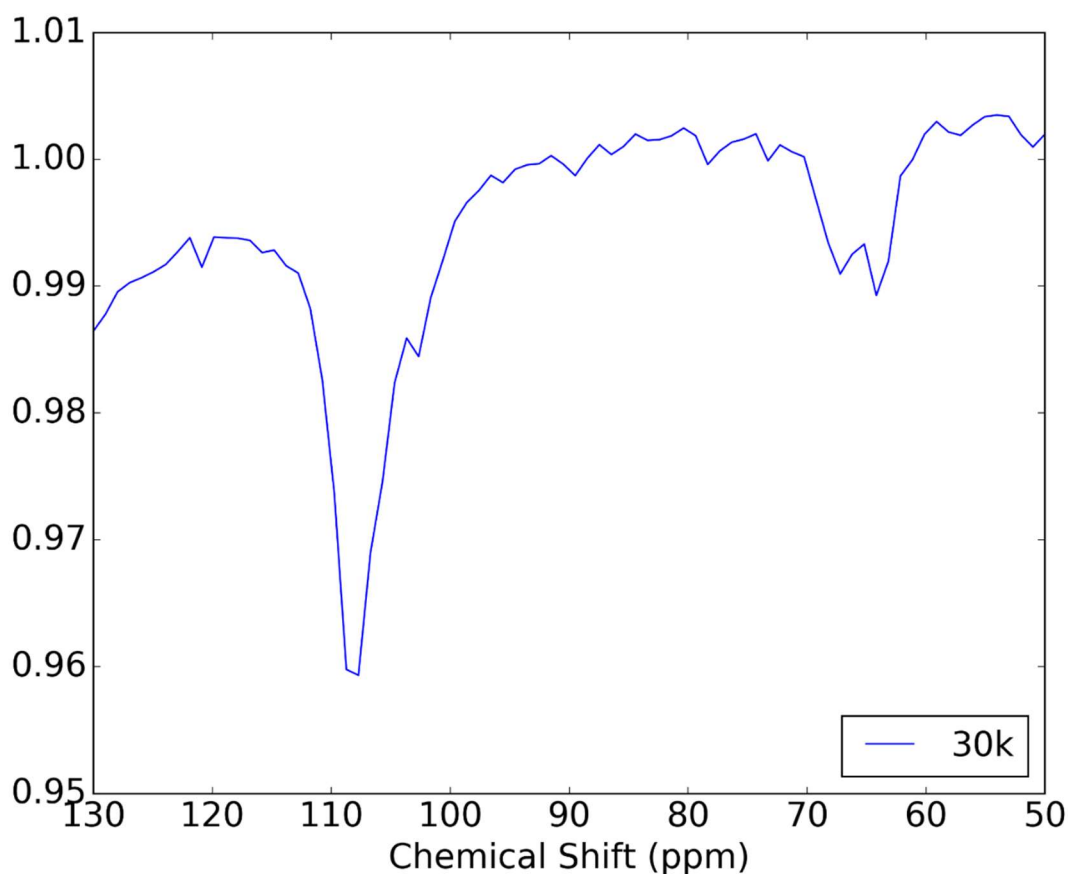
Figure 4.10 | CEST spectrum of a slice at the fuel-water interface of a PAO1 biofilm sample.

 These results determined that the fuel-water interface was observed using a selective pulse offset of -30 kHz, which corresponds to a z position located 670 μm above the center of the NMR coil. The slice-selective CEST spectrum was collected at this offset is shown in Figure 4.10. The peaks in the slice have significantly lower intensity than in the standard curve samples, which is expected

considering a smaller amount of sample is being measured. The ratio of the CEST effect at 106 vs 65 ppm gave a calculated pH of 6.85 ppm which agreed well the pH of the Co_2 solution as measured with a potentiometric pH meter.

4.4 SUMMARY AND OUTLOOK

The results above represent our preliminary efforts toward using a PARACEST pH sensor to measure acid-producing biofilms. We have concluded that several microbes of interest do indeed grow in the presence of 5 mM Co_2. Of equal importance is our progress in developing the slice-selective PARACEST NMR pulse sequence that allows us to take PARACEST spectra at specific locations along the z axis of an NMR sample. Future work will focus on obtaining slice-selective PARACEST spectra for the four biofilms above, at various locations in the NMR sample over a period of several weeks. Doing so will allow us to compare the acidification rate of a variety of microbes, and to relate acid generation to microbial growth and metabolism.

REFERENCES

Chapter 1: Introduction.

(1)   R. H. Crabtree, *Organometallic Chemistry of the Transition Metals*, John Wiley & Sons, Inc., Hoboken, New Jersey, 5th edn., 2009.

(2)   (a) Winpenny, R. E. P. *Single Molecule Magnets and Related Phenomena.* Springer: Berlin, 2006; Vol. 122. (b) Gatteschi, D.; Sessoli, R.; Villain, J. *Molecular Nanomagnets*; Oxford University Press: Oxford, 2006.

(3)   (a) S. Laurent, C. Henoumont, D. Stanicki, S. Boutry, E. Lipani, S. Belaid, R. N. Muller and L. Vander Elst, *MRI Contrast Agents*, Springer Singapore, Singapore, 2017. (b) A. Merbach, L. Helm and É. Tóth, Eds., *The Chemistry of Contrast Agents in Medical Magnetic Resonance Imaging*, John Wiley & Sons, Ltd, Chichester, UK, 2013.

(4)   I. Bertini, H. B. Gray, E. I. Stiefel and J. S. Valentine, Eds., *Biological Inorganic Chemistry: Structure and Reactivity*, 1st edn., 2007.

(5)   O. Sato, J. Tao and Y. Z. Zhang, *Angew. Chemie - Int. Ed.*, 2007, **46**, 2152–2187.

(6)   (a) Coulon, C.; Miyasaka, H.; Clérac, R. *Struct. Bond.* **2006**, *122*, 163. (b) Feng, X.; Harris, T. D.; Long, J. R. *Chem. Sci.* **2011**, *2*, 1688. (c) Gatteschi, D. In *Molecular Magnets*; Bartolome, J., Luis, F., Fernández, J., Eds.; Springer-Verlag: Berlin, 2014; Vol. 1, p 191. (d) Coulon, C.; Pianet, V.; Urdampilleta, M.; Clérac, R. *Struct. Bond.* **2015**, *164*, 143.

(7)   Domb, C. In *Phase transition and critical phenomena*; Domb, C., Green, M. S., Eds.; Academic Press: London, New York, 1974; Vol. 3, Chapter 6, p 357.

(8)   (a) Zener, C. *Phys. Rev.* **1951**, *82*, 403. (b) Girerd, J.-J. *J. Chem. Phys.* **1983**, *79*, 1766.

(9)   A. I. Gaudette, I.-R. Jeon, J. S. Anderson, F. Grandjean, G. J. Long and T. D. Harris, *J. Am. Chem. Soc.*, 2015, **137**, 12617.

(10)   C. Lefter, V. Davesne, L. Salmon, G. Molnár, P. Demont, A. Rotaru and A. Bousseksou, *Magnetochemistry*, 2016, **2**, 18.

(11)   K. Senthil Kumar and M. Ruben, *Coord. Chem. Rev.*, 2017, **346**, 176.

(12)   (a) M. A. Halcrow, *Chem. Lett.*, 2014, **43**, 1178. (b) M. A. Halcrow, *Chem. Soc. Rev.*, 2011, **40**, 4119.

(13)   V. Ksenofontov, A. B. Gaspar and P. Gütlich, in *Spin Crossover in Transition Metal Compounds III*, Springer Berlin Heidelberg, Berlin, Heidelberg, 2004, 23.

(14)   (a) A. Cannizzo, C. J. Milne, C. Consani, W. Gawelda, C. Bressler, F. van Mourik and M. Chergui, *Coord. Chem. Rev.*, 2010, **254**, 2677. (b) A. Hauser, in *Spin Crossover in Transition Metal Compounds II*, Springer Berlin Heidelberg, Berlin, Heidelberg, 2004, 155.

(15)   (a) A. E. Thorarinsdottir, A. I. Gaudette and T. D. Harris, *Chem. Sci.*, 2017, **8**, 2448. (b) I.-R. Jeon, J. G. Park, C. R. Haney and T. D. Harris, *Chem. Sci.*, 2014, **5**, 2461.

(16)   (a) A. M. McDaniel, C. M. Klug and M. P. Shores, *Eur. J. Inorg. Chem.*, 2013, **2013**, 943; (b) S. A. Barrett and M. A. Halcrow, *RSC Adv.*, 2014, **4**, 11240.

(17)   (a) F. Touti, P. Maurin and J. Hasserodt, *Angew. Chemie Int. Ed.*, 2013, **52**, 4654; (b) J. Hasserodt, *New J. Chem.*, 2012, **36**, 1707; (c) C. Gondrand, F. Touti, E. Godart, Y. Berezhanskyy, E. Jeanneau, P. Maurin and J. Hasserodt, *Eur. J. Inorg. Chem.*, 2015, **2015**, 1376; (d) V. Stavila, M. Allali, L. Canaple, Y. Stortz, C. Franc, P. Maurin, O. Beuf, O. Dufay, J. Samarut, M. Janier and J. Hasserodt, *New J. Chem.*, 2008, **32**, 428; (e) J. Wang, C. Gondrand, F. Touti and J. Hasserodt, *Dalt. Trans.*, 2015, **44**, 15391.

(18)   (a) B. Y. R. J. Gillies, N. Raghunand, M. L. Garcia-martin, R. A. Gatenby and R. Gillies, *IEEE Eng. Med. Biol. Mag.*, 2004, **23**, 57; (b) R. J. Gillies, N. Raghunand, G. S. Karczmar and Z. M. Bhujwalla, *J. Magn. Reson. Imaging*, 2002, **16**, 430; (c) R. A. Gatenby and R. J. Gillies, *Nat. Rev. Cancer*, 2004, **4**, 891; (d) P. Vaupel, F. Kallinowski and P. Okunieff, *Cancer Res.*, 1989, **49**, 6449; (e) I. F. Tannock and D. Rotin, *Cancer Res.*, 1989, **49**, 4373; (f) F. Kallinowski, K. H. Schlenger, S. Runkel, M. Kloes, M. Stohrer, P. Okunieff and P. Vaupel, *Cancer Res.*, 1989, **49**, 3759.a

(19)   (a) J. J. Lemasters, J. M. Bond, E. Chacon, I. S. Harper, S. H. Kaplan, H. Ohata, D. R. Trollinger, B. Herman and W. E. Cascio, *EXS*, 1996, **76**, 99; (b) T. Kalogeris, C. P. Baines, M. Krenz and R. J. Korthuis, in *Int. Rev. Cell Mol. Biol.*, 2012, **32**, 229; (c) K. Katsura, A. Ekholm, B. Asplund and B. K. Siesjö, *J. Cereb. Blood Flow Metab.*, 1991, **11**, 597.

(20)   (a) R. Nowak, E. A. Prasetyanto, L. De Cola, B. Bojer, R. Siegel, J. Senker, E. Rössler and B. Weber, *Chem. Commun.*, 2017, **53**, 97;. (b) M. Enamullah, W. Linert, V. Gutmann and R. F. Jameson, *Chem. Mon.*, 1994, **125**, 1301.

(21)   J. Ruiz-Cabello, B. P. Barnett, P. A. Bottomley and J. W. M. Bulte, *NMR Biomed.*, 2011, **24**, 114.

(22)   I. Bertini and C. Luchinat, *NMR of Paramagnetic Molecules in Bilogical Systems*, The Benjamin/Cummins Publishing Company, Inc., Menlo Park, CA, 1986.

Chapter 2: Electron Hopping through Double-Exchange Coupling in a Mixed-Valence Fe₂ Complex.

(23)   (a) Gatteschi, D.; Sessoli, R.; Villain, J. *Molecular Nanomagnets*; Oxford University Press: Oxford, 2006. (b) Winpenny, R. E. P. *Single Molecule Magnets and Related Phenomena.* Springer: Berlin, 2006; Vol. 122.

(24)   (a) Leuenberger, M. N.; Loss, D. *Nature* **2001**, *410*, 789. (b) Rocha, A. R.; García-suárez, V. M.; Bailey, S. W.; Lambert, C. J.; Ferrer, J.; Sanvito, S. *Nat. Mater.* **2005**, *4*, 335. (c) Bogani, L.; Wernsdorfer, W. *Nat. Mater.* **2008**, *7*, 179. (d) Stamp, P. C. E.; Gaita-Arino, A. *J. Mater. Chem.* **2009**, *19*, 1718. (e) Ardavan, A.; Blundell, S. J. *J. Mater. Chem.* **2009**, *19*, 1754.

(25)   Multinuclear complexes: (a) Caneschi, A.; Gatteschi, D.; Sessoli, R.; Barra, A. L.; Brunel, L. C.; Guillot, M. *J. Am. Chem. Soc.* **1991**, *113*, 5873. (b) Sessoli, R.; Tsai, H.-L.; Schake, A. R.; Wang, J. B.; Folting, K.; Gatteschi, D.; Christou, G.; Hendrickson, D. N. *J. Am. Chem. Soc.* **1993**, *115*, 1804. (c) Sessoli, R.; Gatteschi, D.; Caneschi, A.; Novak, M. A. *Nature* **1993**, *365*, 141. (d) Sokol, J. J.; Hee, A. G.; Long, J. R. *J. Am. Chem. Soc.* **2002**, *124*, 7656. (e) Berlinguette, C. P.; Vaughn, D.; Cañada-Vilalta, C.; Galán-Mascarós, J. R.; Dunbar, K. R. *Angew. Chem., Int. Ed.* **2003**, *42*, 1523. (f) Parsons, S.; Perlepes, S. P.; Christou, G.; Brechin, E. K. *J. Am. Chem. Soc.* **2007**, *129*, 2754. (g) Bagai, R.; Christou, G. *Chem. Soc. Rev.* **2009**, *38*, 1011.

(26)   Mononuclear complexes: (a) Freedman, D. E.; Harman, W. H.; Harris, T. D.; Long, G. J.; Chang, C. J.; Long, J. R. *J. Am. Chem. Soc.* **2010**, *132*, 1224-1225. (b) Zadrozny, J. M.;

Long, J. R. *J. Am. Chem. Soc.* **2011**, *133*, 20732. (c) Craig, G. A.; Murrie, M. *Chem. Soc. Rev.* **2015**, *44*, 2135.

(27)   Multinuclear complexes: (a) Tang, J.; Hewitt, I. J.; Madhu, N. T.; Chastanet, G.; Wernsdorfer, W.; Anson, C. E.; Benelli, C.; Sessoli, R.; Powell, A. K. *Angew. Chem. Int. Ed.* **2006**, *45*, 1729. (b) Lin, P.-H.; Burchell, T. J.; Clérac, R.; Murugesu, M. *Angew. Chem. Int. Ed.* **2008**, *47*, 8848. (c) Rinehart, J. D.; Fang, M.; Evans, W. J.; Long, J. R. *J. Am. Chem. Soc.* **2011**, *133*, 14236.

(28)   Mononuclear complexes: (a) Ishikawa, N.; Sugita, M.; Ishikawa, T.; Koshihara, S.-y.; Kaizu, Y. *J. Am. Chem. Soc.* **2003**, *125*, 8694. (b) AlDamen, M. A.; Clemente-Juan, J. M.; Coronado, E.; Marti-Gastaldo, C.; Gaita-Arino, A. *J. Am. Chem. Soc.* **2008**, *130*, 8874. (c) Rinehart, J. D.; Long, J. R. *Chem. Sci.* **2011**, *2*, 2078. (d) Ganivet, C. R.; Ballesteros, B.; de la Torre, G.; Clemente-Juan, J. M.; Coronado, E.; Torres, T. *Chem. Eur. J.* **2013**, *19*, 1457. (e) Liddle, S. T.; van Slageren, J. *Chem. Soc. Rev.* DOI: 10.1039/c5cs00222b.

(29)   Multinuclear complexes: (a) Magnani, N.; Colineau, E.; Eloirdi, R.; Griveau, J. C.; Caciuffo, R.; Cornet, S. M.; May, I.; Sharrad, C. A.; Collison, D.; Winpenny, R.E.P. *Phys. Rev. Lett.* **2010**, *104*, 197202. (b) Mills, D. P.; Moro, F.; McMaster, J.; van Slageren, J.; Lewis, W.; Blake, A. J.; Liddle, S. T. *Nat. Chem.* **2011**, *3*, 454.

(30)   Mononuclear complexes: (a) Rinehart, J. D.; Long, J. R. *J. Am. Chem. Soc.* **2009**, *131*, 12558. (b) Magnani, N.; Apostolidis, C.; Morgenstern, A.; Colineau, E.; Griveau, J.-C.; Bolvin, H.; Walter, O.; Caciuffo, R. *Angew. Chem. Int. Ed.* **2011**, *50*, 1696.

(31)   (a) Kahn, O.; *Molecular Magnetism;* VCH: New York, 1993. (b) Demir, S.; Jeon, I.-R.; Long, J. R.; Harris, T. D. *Coord. Chem. Rev.* **2015**, *289*, 149.

(32)   (a) Coulon, C.; Miyasaka, H.; Clérac, R. *Struct. Bond.* **2006**, *122*, 163. (b) Feng, X.; Harris, T. D.; Long, J. R. *Chem. Sci.* **2011**, *2*, 1688. (c) Gatteschi, D. In *Molecular Magnets*; Bartolome, J., Luis, F., Fernández, J., Eds.; Springer-Verlag: Berlin, 2014; Vol. 1, p 191. (d) Coulon, C.; Pianet, V.; Urdampilleta, M.; Clérac, R. *Struct. Bond.* **2015**, *164*, 143.

(33)   Domb, C. In *Phase transition and critical phenomena*; Domb, C., Green, M. S., Eds.; Academic Press: London, New York, 1974; Vol. 3, Chapter 6, p 357.

(34)   (a) Zener, C. *Phys. Rev.* **1951**, *82*, 403. (b) Girerd, J.-J. *J. Chem. Phys.* **1983**, *79*, 1766.

(35)   (a) Drüeke, S.; Chaudhuri, P.; Pohl, K.; Wieghardt, K. ; Ding, X.-Q.; Bill, E.; Sawaryn, A.; Trautwein, A. X.; Winkler, H.; Gurman, S. J. *Chem. Commun*. **1989**, 59. (b) Gamelin, D. R.; Bominaar, E. L.; Kirk, M. L.; Wieghardt, K.; Solomon, E. I. *J. Am. Chem. Soc.* **1996**, *118*, 8085.

(36)   (a) Dutta, S. K.; Ensling, J.; Werner, R.; Flörke, U.; Haase, W.; Gütlich, P.; Nag, K. *Angew*. *Chem*. *Int*. *Ed*. **1997**, *36*, 152. (b) Hazra, S.; Sasmal, S.; Fleck, M.; Grandjean, F.; Sougrati, M. T.; Ghosh, M.; Harris, T. D.; Bonville, P.; Long, G. J.; Mohanta, S. *J. Chem. Phys.* **2011**, *134*, 174507.

(37)   Hagadorn, J. R.; Que, Jr., L.; Tolman, W. B.; Prisecaru, I.; Münck. *J. Am. Chem. Soc.* **1999**, *121*, 9760.

(38)   (a) Lee, D.; Krebs, C.; Huynh, B. H.; Hendrich, M. P.; Lippard, S. J. *J. Am. Chem. Soc.* **2000,** *122,* 5000. (b) Lee, D.; DuBois, J. L.; Pierce, B.; Hedman, B.; Hodgson, K. O.; Hendrich, M. P.; Lippard, S. J. *Inorg. Chem.* **2002**, *41*, 3172.

(39)   (a) Noodleman, L.; Baerends, E. J. *J. Am. Chem. Soc.* **1984**, *106*, 2316. (b) Münck, E.; Papaefthymiou, V.; Surerus, K. K.; Girerd, J.-J. *Metal Clusters in Proteins*; Que, L., Jr., Ed.; American Chemical Society: Washington, DC, 1988; pp 302-325. (c) Noodleman, L.;

Case, D. A. *Adv. Inorg. Chem.* **1992**, *38*, 423. (d) Borshch, S. A.; Bominaar, E. L.; Blondin, G.; Girerd, J.-J. *J. Am. Chem. Soc.* **1993**, *115*, 5155. (e) Achim, C.; Golinelli, M.-P.; Bominaar, E. L.; Meyer, J.; Münck, E. *J. Am. Chem. Soc.* **1996**, *118*, 8168.

(40)   Bechlars, B.; D'Alessandro, D. M.; Jenkins, D. J.; Iavarone, A. T.; Glover, S. D.; Kubiak, C. P.; Long, J. R. *Nat. Chem.* **2010**, *2*, 362.

(41)   Co: Heinze, K.; Huttner, G.; Walter, O. *Eur. J. Inorg. Chem.* **1999**, 593.

(42)   Ni: Siri, O.; Taquet, J. P.; Collin, J. P.; Rohmer, M. M.; Bénard, M.; Braunstein, P. *Chem. Eur. J.* **2005**, *11*, 7247.

(43)   Ru: (a) Kar, S.; Sarkar, B.; Ghumaan, S.; Janardanan, D.; van Slageren, J.; Fiedler, J.; Puranik, V. G.; Sunoj, R. B.; Kaim, W.; Lahiri, G. K. *Chem. Eur. J.* **2005**, *11*, 4901. (b) Ghumaan, S.; Sarkar, B.; Maji, S.; Puranik, V. G.; Fiedler, J.; Urbanos, F. A.; Jimenez-Aparicio, R.; Kaim, W.; Lahiri, G. K. *Chem. Eur. J.* **2008**, *14*, 10816. (c) Das, H. S.; Das, A. K.; Pattacini, R.; Hübner, R.; Sarkar, B.; Braunstein, P. *Chem. Commun.* **2009**, 4387. (d) Das, H. S.; Weisser, F.; Schweinfurth, D.; Su, C. Y.; Bogani, L.; Fiedler, J.; Sarkar, B. *Chem. Eur. J.* **2010**, *16*, 2977. (e) Weisser, F.; Huebner, R.; Schweinfurth, D.; Sarkar, B. *Chem. Eur. J.* **2011**, *17*, 5727. (f) Sommer, M. G.; Schweinfurth, D.; Weisser, F.; Hohloch, S.; Sarkar, B. *Organometallics* **2013**, *32*, 2069. (g) Das, H. S.; Schweinfurth, D.; Fiedler, J.; Khusniyarov, M. M.; Mobin, S. M.; Sarkar, B. *Chem. Eur. J.* **2014**, *20*, 4334. (h) Sarkar, B.; Schweinfurth, D.; Deibel, N.; Weisser, F. *Coord. Chem. Rev.* **2015**, *293*, 250.

(44)   Os: Gupta, P.; Das, A.; Basuli, F.; Castineiras, A.; Sheldrick, W. S.; Mayer-Figge, H.; Bhattacharya, S. *Inorg. Chem.* **2005**, *44*, 2081.

(45)   Buschmann, W. E.; Miller, J. S. *Chem. Eur. J.* **1998**, *4*, 1731.

(46)   Rosokha, S. V.; Stern, C. L.; Ritzert, J. T. *Cryst. Eng. Comm* **2013**, *15*, 10638.

(47)   Beni, A.; Dei, A.; Laschi, S.; Rizzitano, M.; Sorace, L. *Chem. Eur. J.* **2008**, *14*, 1804.

(48)   Amonoo-Neizer, E. H.; Shaw, R. A.; Skovlin, D. O.; Smith, B. C. *Inorg. Synth.* **1966**, *8*, 19.

(49)   *SAINT: Software for the Integration of CCD Detector System*, version 8.27B; Bruker AXS Inc.: Madison, WI, **2007**.

(50)   Sheldrick, G. M. *Acta Crystallogr. Sect. A: Found. Adv.* **2015**, *71*, 3.

(51)   Sheldrick, G. M. *Acta Crystallogr., Sect. A: Found. Crystallogr*. **2008**, 64, 112.

(52)   Dolomanov, O. V.; Bourhis, L. J.; Gildea, R. J.; Howard, J. A. K.; Puschmann, H. *J. Appl. Cryst.* **2009.** *42*, 339.

(53)   Thorn, A.; Dittrich, B.; Sheldrick, G. M. *Acta Crystallogr. Sect. A: Found. Crystallogr.* **2012**, *68*, 448.

(54)   (a) Cole, K. S.; Cole, R. H. *J. Chem. Phys.* **1941**, *9*, 341. (b) Boettcher, C. J. F. *Theory of Electric Polarisation*; Elsevier: Amsterdam, 1952. (c) Aubin, S. M.; Sun, Z.; Pardi, L.; Krzysteck, J.; Folting, K.; Brunel, L.-J.; Rheingold, A. L.; Christou, G.; Hendrickson, D. N. *Inorg. Chem.* **1999**, *38*, 5329.

(55)   Bain, G. A.; Berry, J. F. *J. Chem. Ed.* **2008**, *85*, 532.

(56)   (a) Das, H. S.; Weisser, F.; Schweinfurth, D.; Su, C-Y.; Bogani, L.; Fiedler, J.; Sarkar, B. *Chem. Eur. J.* **2010**, *16*, 2977. (b) Sommer, M. G.; Schweinfurth, D.; Weisser, F.; Hohloch, S.; Sarkar, B. *Organometallics* **2013**, *32*, 2069. (c) Das, H. S.; Schweinfurth, D.; Fiedler, J.; Khusniyarov, M. M.; Mobin, S. M.; Sarkar, B. *Chem. Eur. J.* **2014**, *20*, 4334.

(57)   (a) Schweinfurth, D.; Khusniyarov, M. M.; Bubrin, D.; Hohloch, S.; Su, C-Y.; Sarkar, B. *Inorg. Chem.* **2013**, *52*, 10332. (b) Schweinfurth, D.; Rechkemmer, Y.; Hohloch, S.; Deibel,

N.; Peremykin, I.; Fiedler, J.; Marx, R.; Neugebauer, P.; van Slageren, J.; Sarkar, B. *Chem. Eur. J.* **2014**, *20*, 3475.

(58)   Zhang, D.; Jin, G-X. *Organometallics* **2003**, *22*, 2851.

(59)   Jia, W-G.; Han, Y-F.; Lin, Y-J.; Weng, L-H.; Jin, G-X. *Organometallics* **2009**, *28*, 3459.

(60)   Park, J. G.; Jeon, I.-R.; Harris, T. D. *Inorg. Chem.* **2015**, *54*, 359.

(61)   Connelly, N. G.; Geiger, W. E. *Chem. Rev.* **1996**, *96*, 877.

(62)   Jeon, I.-R.; Park, J. G.; Xiao, D. J.; Harris, T. D. *J. Am. Chem. Soc.* **2013**, *135*, 16845.

(63)   (a) Litterst, F. J.; Amthauer, G. *Phys. Chem. Min*. **1984**, *10,* 250. (b) Tjon, J. A.; Blume, M. *Phys. Rev*. **1968**, *165*, 456.

(64)   (a) Dong, T.-Y.; Cohn, M. J.; Hendrickson, D. N.; Pierpont, C. G. *J. Am. Chem. Soc.* **1985**, *107*, 4777. (b) Cohn, M. J.; Dong, T.-Y.; Hendrickson, D. N.; Geib, S. J.; Rheingold, A. L. *J. Chem. Soc., Chem. Commun.* **1985**, 1095. (c) Dong, T.-Y.; Hendrickson, D. N.; Iwai, K.; Cohn, M. J.; Rheingold, A. L.; Sano, H.; Motoyama, I.; Nakashima, S. *J. Am. Chem. Soc.* **1985**, *107*, 7996. (d) Moore, M. F.; Wilson, S. R.; Cohn, M. J.; Dong, T.-Y.; Mueller-Westerhoff, U. T.; Hendrickson, D. N. *Inorg. Chem.* **1985**, *24*, 4559. (e) Dong, T.-Y.; Hendrickson, D. N.; Pierpont, C. G.; Moore, M. F. *J. Am. Chem. Soc.* **1986**, *108*, 963. (f) Dong, T. Y.; Kambara, T.; Hendrickson, D. N. *J. Am. Chem. Soc.* **1986**, *108*, 5857. (g) Dong, T. Y.; Schei, C. C.; Hsu, T. L.; Lee, S. L.; Li, S. J. *Inorg. Chem.* **1991**, *30*, 2457. (h) Manago, T.; Hayami, S.; Oshio, H.; Osaki, S.; Hasuyama, H.; Herber, R. H.; Maeda, Y. *Dalton Trans.* **1999**, 1001. (i) Oda, T.; Nakashima, S.; Okuda, T. *Bull. Chem. Soc. Jpn.* **2003**, *76*, 2129. (j) Venkatasubbaiah, K.; Doshi, A.; Nowik, I.; Herber, R. H.; Rheingold, A. L.; Jäkle, F. *Chem. Eur. J.* **2008**, *14*, 444.

(65)   (a) Cannon R. D.; Montri, L.; Brown, D. B.; Marshall, K. M.; Elliott, C. M. *J. Am. Chem. Soc.* **1984**, *106*, 2591. (b) Oh, S. M.; Hendrickson, D. N.; Hassett, K. L.; Davis, R. E. *J. Am. Chem. Soc.* **1984**, *106*, 7984. (c) Oh, S. M.; Hendrickson, D. N.; Hassett, K. L.; Davis, R. E. *J. Am. Chem. Soc.* **1985**, *107*, 8009. (d) Sorai, M.; Kaji, K.; Hendrickson, D. N.; Oh, S. M. *J. Am. Chem. Soc.* **1986**, *108*, 702. (e) Woehler, S. E.; Wittebort, R. J.; Oh, S. M.; Kambara, T.; Hendrickson, D. N.; Inniss, D.; Strouse, C. E. *J. Am. Chem. Soc.* **1987**, *109*, 1063. (f) Cannon, R. D.; White, R. P. *Prog. Inorg. Chem.* **1988**, *36*, 195. (g) Kaneko, Y.; Nakano, M.; Sorai, M.; Jang, H. G.; Hendrickson, D. N. *Inorg. Chem.* **1989**, *28*, 1067. (h) Jang, H. G.; Geib, S. J.; Kaneko, Y.; Nakano, M.; Sorai, M.; Rheingold, A. L.; Montez, B.; Hendrickson, D. N. *J. Am. Chem. Soc.* **1989**, *111*, 173. (i) Cannon, R. D.; Jayasooria, U. A.; Arap Koske, S. K.; White, R. P.; Williams, J. H. *J. Am. Chem. Soc.* **1991**, *113*, 4158. (j) Nakamoto, T.; Katada, M.; Kawata, S.; Kitagawa, S.; Kikuchi, K.; Ikemoto, I.; Endo, K.; Sano, H. *Chem. Lett.* **1993**, *22*, 1463. (k) Nakamoto, T.; Katada, M.; Kawata, S.; Kitagawa, S.; Sano, H.; Konno, M. *Hyperfine Interact.* **1994**, *93*, 1567. (l) Sato, T.; Ambe, F.; Endo, K.; Katada, M.; Maeda, H.; Nakamoto, T.; Sano, H. *J. Am. Chem. Soc.* **1996**, *118*, 3450. (m) Onaka, S.; Sakai, Y.; Ozeki, T.; Nakamoto, T.; Kobayashi, Y.; Takahashi, M.; Ogiso, R.; Takayama, T.; Shiotsuka, M. *Dalton Trans.* **2014**, *43*, 6711. (n) Okazawa, A.; Yoshida, J.; Kida, N.; Kashima, I.; Murata, W.; Enomoto, M.; Kojima, N. *Hyperfine Interact.* **2014**, *226*, 351.

(66)   Sorai, M.; Nishimori, A.; Hendrickson, D. N.; Dong, T. Y.; Cohn, M. J. *J. Am. Chem. Soc.* **1987**, *109*, 4266.

(67)   Surerus, K. K.; Münck, E.; Snyder, B. S.; Holm, R. H. *J. Am. Chem. Soc.* **1989**, *111*, 5501.

(68)   Hush, N. S. *Prog. Inorg. Chem.* **1967**, *8*, 391.

(69)   Brunschwig, B. S.; Creutz, C.; Sutin, N. *Chem. Soc. Rev.* **2002**, *31*, 168.

(70)   (a) D'Alessandro, D. M.; Keene, F. R. *Chem. Soc. Rev.* **2006**, *35*, 424. (b) Nelsen, S. *Chem. Eur. J.* **2000**, *6*, 581. (b) Nelsen, S. *Chem. Eur. J.* **2000**, *6*, 581.

(71)   (a) Demadis, K. D.; Hartshorn, C. M.; Meyer, T. J. *Chem. Rev.* **2001**, *101*, 2655. (b) Hush, N. S. *Coord. Chem. Rev.* **1985**, *64*, 135.

(72) $H_{AB} = \dfrac{2.06 \times 10^{-2} \left(\nu_{max} \varepsilon_{max} \varDelta \nu_{1/2} \right)^{1/2}}{r_{AB}}$, where ν_{max} is the absorption maximum in cm^{-1}, ε_{max} is the extinction coefficient at ν_{max} in M^{-1}cm^{-1}, $\varDelta \nu_{1/2}$ is the full width at half maximum in cm^{-1} and r_{AB} is the electron transfer distance in Å. The value of 2.06×10^{-2} is empirically determined.

(73)   Ding, X.-Q.; Bominaar, E. L.; Bill, E.; Winkler, H.; Trautwein, A. X.; Drüeke, S.; Chaudhuri, P.; Wieghardt, K. *J. Chem. Phys.* **1990**, *92*, 178.

(74)   Min, K. S.; DiPasquale, A. G.; Golen, J. A.; Rheingold, A. L.; Miller, J. S. *J. Am. Chem. Soc.* **2007**, *129*, 2360.

(75)   Reduced magnetization data for **1** and **2** were fit using the program MagProp. See (a) Tregenna-Piggott, P. L. W. *MagProp (part of the NIST DAVE software suite), version 2.0*; 2008; http://www.ncnr.nist.gov/dave. (b) Azuah, R. T.; Kneller, L. R.; Qiu, Y. M.; Tregenna-Piggott, P. L. W.; Brown, C. M.; Copley, J. R. D.; Dimeo, R. M. *J. Res. Natl. Inst. Stand. Technol.* **2009**, *114*, 341.

(76)   Here, $\hat{O}_A$ and $\hat{O}_B$ are the occupation operators, and T_{AB} is the transfer operator. See Blondin, G.; Girerd, J.-J. *Chem. Rev.* **1990**, *90*, 1359.

(77)   This value was obtained from fitting variable-temperature magnetic susceptibility data with a model that neglects vibronic coupling. Upon inclusion of vibronic coupling in the model, a larger value of $B = 220$ cm^{-1} was obtained.

(78)   Kirk, M. L.; Shultz, D. A.; Schmidt, R. D.; Habel-Rodriguez, D.; Lee, H.; Lee, J. *J. Am. Chem. Soc.* **2009**, *131*, 18304.

(79)   Here, we define a redox-switchable single-molecule magnet as a complex that features at least one reversible redox process and at least two isolable redox isomers, with at least one of those isomers showing slow magnetic relaxation.

(80)   Freedman, D. E.; Jenkins, D. M.; Iavarone, A. T.; Long, J. R. *J. Am. Chem. Soc.* **2008**, *130*, 2884.

(81)   Fortier, S.; Le Roy, J. J.; Chen, C.-H.; Vieru, V.; Murugesu, M.; Chibotaru, L. F.; Mindiola, D. J.; Caulton, K. G. *J. Am. Chem. Soc.* **2013**, *135*, 14670.

(82)   (a) Liang, W.; Shores, M. P.; Bockrath, M.; Long, J. R.; Park, H. *Nature* **2002**, *417*, 725. (b) Jo, M.-H.; Grose, J. E.; Liang, W.; Baheti, K.; Deshmukh, M. M.; Sokol, J. J.; Rumberger, E. M.; Hendrickson, D. N.; Long, J. R.; Park, H.; Ralph, D. C. *Nano Lett.* **2006**, *6*, 2014.

(83)   (a) Zadrozny, J. M.; Liu, J.; Piro, N. A.; Chang, C. J.; Hill, S.; Long, J. R. *Chem. Commun.* **2012**, *48*, 3927. (b) Huang, W.; Liu, T.; Wu, D.; Cheng, J.; Ouyang; Z. W.; Duan, C. *Dalton Trans.* **2013**, 42, 15326. (c) Colacio, E.; Ruiz, J.; Ruiz, E.; Cremades, E.; Krzystek, J.; Carretta, S.; Cano, J.; Guidi, T.; Wernsdorfer, W.; Brechin, E. K. *Angew. Chem. Int. Ed.* **2013**, *52*, 9130.

(84)   (a) Freedman, D. E.; Harman, W. H.; Harris, T. D.; Long, G. J.; Chang, C. J.; Long, J. R. *J. Am. Chem. Soc.* **2010**, *132*, 1224. (b) Harman, W. H.; Harris, T. D.; Freedman, D. E.;

Fong, H.; Chang, A.; Rinehart, J. R.; Ozarowski, A.; Sougrati, M. T.; Grandjean, F.; Long, G. J.; Long, J. R.; Chang, C. J. *J. Am. Chem. Soc.* **2010**, *132*, 18115.

(85)   Zadrozny, J. M.; Atanasov, M.; Bryan, A. M.; Lin, C.-Y.; Rekken, B. D.; Power, P. P.; Neese, F.; Long, J. R. *Chem. Sci***. 2013**, *4*, 125.

Chapter 3: pH-Dependent Spin-State Population and 19F NMR Chemical Shifts via Remote Ligand Protonation in an Iron(II) Complex.

(86)   P. Gütlich and H. A. Goodwin, in *Topics in Current Chemistry*, 2004, vol. 233, 1.

(87)   C. Lefter, V. Davesne, L. Salmon, G. Molnár, P. Demont, A. Rotaru and A. Bousseksou, *Magnetochemistry*, 2016, **2**, 18.

(88)   K. Senthil Kumar and M. Ruben, *Coord. Chem. Rev.*, 2017, **346**, 176.

(89)   (a) M. A. Halcrow, *Chem. Lett.*, 2014, **43**, 1178. (b) M. A. Halcrow, *Chem. Soc. Rev.*, 2011, **40**, 4119.

(90)   V. Ksenofontov, A. B. Gaspar and P. Gütlich, in *Spin Crossover in Transition Metal Compounds III*, Springer Berlin Heidelberg, Berlin, Heidelberg, 2004, 23.

(91)   (a) A. Cannizzo, C. J. Milne, C. Consani, W. Gawelda, C. Bressler, F. van Mourik and M. Chergui, *Coord. Chem. Rev.*, 2010, **254**, 2677. (b) A. Hauser, in *Spin Crossover in Transition Metal Compounds II*, Springer Berlin Heidelberg, Berlin, Heidelberg, 2004, 155.

(92)   (a) A. E. Thorarinsdottir, A. I. Gaudette and T. D. Harris, *Chem. Sci.*, 2017, **8**, 2448. (b) I.-R. Jeon, J. G. Park, C. R. Haney and T. D. Harris, *Chem. Sci.*, 2014, **5**, 2461.

(93)   (a) A. M. McDaniel, C. M. Klug and M. P. Shores, *Eur. J. Inorg. Chem.*, 2013, **2013**, 943; (b) S. A. Barrett and M. A. Halcrow, *RSC Adv.*, 2014, **4**, 11240.

(94)   (a) F. Touti, P. Maurin and J. Hasserodt, *Angew. Chemie Int. Ed.*, 2013, **52**, 4654; (b) J. Hasserodt, *New J. Chem.*, 2012, **36**, 1707; (c) C. Gondrand, F. Touti, E. Godart, Y. Berezhanskyy, E. Jeanneau, P. Maurin and J. Hasserodt, *Eur. J. Inorg. Chem.*, 2015, **2015**, 1376; (d) V. Stavila, M. Allali, L. Canaple, Y. Stortz, C. Franc, P. Maurin, O. Beuf, O. Dufay, J. Samarut, M. Janier and J. Hasserodt, *New J. Chem.*, 2008, **32**, 428; (e) J. Wang, C. Gondrand, F. Touti and J. Hasserodt, *Dalt. Trans.*, 2015, **44**, 15391.

(95)   (a) B. Y. R. J. Gillies, N. Raghunand, M. L. Garcia-martin, R. A. Gatenby and R. Gillies, *IEEE Eng. Med. Biol. Mag.*, 2004, **23**, 57; (b) R. J. Gillies, N. Raghunand, G. S. Karczmar and Z. M. Bhujwalla, *J. Magn. Reson. Imaging*, 2002, **16**, 430; (c) R. A. Gatenby and R. J. Gillies, *Nat. Rev. Cancer*, 2004, **4**, 891; (d) P. Vaupel, F. Kallinowski and P. Okunieff, *Cancer Res.*, 1989, **49**, 6449; (e) I. F. Tannock and D. Rotin, *Cancer Res.*, 1989, **49**, 4373; (f) F. Kallinowski, K. H. Schlenger, S. Runkel, M. Kloes, M. Stohrer, P. Okunieff and P. Vaupel, *Cancer Res.*, 1989, **49**, 3759.

(96)   (a) J. J. Lemasters, J. M. Bond, E. Chacon, I. S. Harper, S. H. Kaplan, H. Ohata, D. R. Trollinger, B. Herman and W. E. Cascio, *EXS*, 1996, **76**, 99; (b) T. Kalogeris, C. P. Baines, M. Krenz and R. J. Korthuis, in *Int. Rev. Cell Mol. Biol.*, 2012, **32**, 229; (c) K. Katsura, A. Ekholm, B. Asplund and B. K. Siesjö, *J. Cereb. Blood Flow Metab.*, 1991, **11**, 597.

(97)   (a) R. Nowak, E. A. Prasetyanto, L. De Cola, B. Bojer, R. Siegel, J. Senker, E. Rössler and B. Weber, *Chem. Commun.*, 2017, **53**, 97;. (b) M. Enamullah, W. Linert, V. Gutmann and R. F. Jameson, *Chem. Mon.*, 1994, **125**, 1301.

(98)   J. Ruiz-Cabello, B. P. Barnett, P. A. Bottomley and J. W. M. Bulte, *NMR Biomed.*, 2011, **24**, 114.

(99)   W. R. Dolbier. *Guide to Fluorine NMR for Organic Chemists*, John Wiley & Sons, Hoboken, NJ, 2009.

(100)   S. He, R. P. Mason, S. Hunjan, V. D. Mehta, V. Arora, R. Katipally, P. V. Kulkarni and P. P. Antich, *Bioorg. Med. Chem.*, 1998, **6**, 1631.

(101)   (a) K. H. Chalmers, E. De Luca, N. H. M. Hogg, A. M. Kenwright, I. Kuprov, D. Parker, M. Botta, J. Ian Wilson and A. M. Blamire, *Chem. Eur. J.*, 2010, **16**, 134; (b) A. M. Kenwright, I. Kuprov, E. De Luca, D. Parker, S. U. Pandya, P. K. Senanayake and D. G. Smith, *Chem. Commun.*, 2008, 2514.

(102)   I. Bertini and C. Luchinat, *NMR of Paramagnetic Molecules in Bilogical Systems*, The Benjamin/Cummins Publishing Company, Inc., Menlo Park, CA, 1986.

(103)   C. M. Moore, E. W. Dahl and N. K. Szymczak, *Curr. Opin. Chem. Biol.*, 2015, **25**, 9.

(104)   Y. M. Badiei, W. H. Wang, J. F. Hull, D. J. Szalda, J. T. Muckerman, Y. Himeda and E. Fujita, *Inorg. Chem.*, 2013, **52**, 12576.

(105)   G. F. Manbeck, J. T. Muckerman, D. J. Szalda, Y. Himeda and E. Fujita, *J. Phys. Chem. B*, 2015, **119**, 7457.

(106)   D. C. Marelius, S. Bhagan, D. J. Charboneau, K. M. Schroeder, J. M. Kamdar, A. R. McGettigan, B. J. Freeman, C. E. Moore, A. L. Rheingold, A. L. Cooksy, D. K. Smith, J. J. Paul, E. T. Papish and D. B. Grotjahn, *Eur. J. Inorg. Chem.*, 2014, 676.

(107)   (a) R. Kawahara, K. Fujita and R. Yamaguchi, *Angew. Chemie Int. Ed.* 2012, **51**, 12790; (b) J. DePasquale, I, Nieto, L. E. Reuther, C. J. Herbst-Gervasoni, J. J. Paul, V. Mochalin, M. Zeller, C. M. Thomas, A. W. Addison and E. T. Papish, *Inorg. Chem.* 2013, **52**, 9175; (c) R. Kawahara and K. Fujita, R. Yamaguchi, *Angew. Chemie Int. Ed.* 2012, **51**, 12790.

(108)   *SAINT-8.34A Software for the Integration of CCD Detector System*; Bruker Analytical X-Ray Systems, Inc: Madison, WI, USA, 2013.

(109)   G. M. Sheldrick, SADABS, version 2.03, Bruker Analytical X-Ray Systems, Madison, WI, USA,

(110)   G. M. Sheldrick, SHELXTL, Version 6.12; Bruker Analytical X-ray Systems, Inc.: Madison, WI, 2000

(111)   G. M. Sheldrich. *Acta Crystallogr., Sect. A: Found. Adv.*, 2015, **71**, 3.

(112)   O. V. Dolomanov, L. J. Bourhis, R. J. Gildea, J. A. K. Howard and H. Puschmann, *J. Appl.Crystallogr.*, 2009, **42**, 339.

(113)   (a) D. F. Evans, *J. Chem. Soc.*, 1959, 2003; (b) E.M. Schubert, *J. Chem. Educ.*, 1992, **69**, 62.

(114)   G. A. Bain and J. F. Berry, *J. Chem. Educ.*, 2008, **85**, 532.

(115)   I. Prat, A. Company, T. Corona, T. Parella, X. Ribas and M. Costas, *Inorg. Chem.*, 2013, **52**, 9229.

(116)   (a) I. Bernal, I. M. Jensen, K. B. Jensen, C. J. McKenzie, H. Toftlund and J.-P. Tuchagues, J. Chem. Soc., *Dalton Trans.*, 1995, 3667; (b) V. Balland, F. Banse, E. Anxolabéhère-Mallart, M. Nierlich and J.-J. Girerd, *Eur. J. Inorg. Chem.*, 2003, 2529; (d)

(117)   W. Linert, M. Konecny and F. Renz, *J. Chem. Soc., Dalton Trans.*, 1994, 1523.

(118)   O. Kahn, *Molecular Magnetism*, VCH Pulishers, Inc., New York, 1993.

(119)   *OriginPro*, version 9.0; OriginLab, Corp.: Northampton, MA, 2003.

(120)   P. B. Tsitovich, J. M. Cox and J. A. Spernyak and J. R. Morrow, *Inorg. Chem.*, 2016, **55**, 12001.

Chapter 4: Utilizing PARACEST NMR pH Sensors to Image Microbial-Induced Corrosion

(121)   Mansfield, E.; Sowards, J. W.; Crookes-Goodson, W. J. *J. Res. Natl. Inst. Stand. Technol.* **2015**, *120*, 28.

(122)   Striebich, R. C.; Smart, C. E.; Gunasekera, T. S.; Mueller, S. S.; Strobel, E. M.; McNichols, B. W.; Ruiz, O. N. *Int. Biodeterior. Biodegradation* **2014**, *93*, 33.

(123)   (a) Li, S. Y.; Kim, Y. G.; Jeon, K. S.; Kho, Y. T. *Met. Mater.* **2000**, *6*, 281. (b) Sowards, J. W.; Mansfield, E. *Corros. Sci.* **2014**, *87*, 460. (c) Xu, D.; Li, Y.; Gu, T. *Bioelectrochemistry* **2016**, *110*, 52.

(124)   Gillies, R. *IEEE Eng. Med. Biol. Mag.* **2004**, *23*, 57.

(125)   (a) Ward, K. M.; Aletras, A. H.; Balaban, R. S. *J. Magn. Reson*. **2000**, *143*, 79. (b) Zhang, S.; Merritt, M.; Woessner, D. E.; Lenkinski, R. E.; Sherry, a D. *Acc. Chem. Res.* **2003**, *36*, 783. (c) Hancu, I.; Dixon, W. T.; Woods, M.; Vinogradov, E.; Sherry, a D.; Lenkinski, R. E. *Acta Radiol.* **2010**, *51*, 910.

(126)   (a) Zhang, S.; Winter, P.; Wu, K.; Sherry, A. D. *J. Am. Chem. Soc*. **2001**, *123*, 1517. (b) Zhang, S.; Merritt, M.; Woessner, D. E.; Lenkinski, R. E.; Sherry, A. D. *Acc. Chem. Res*. **2003**, *36*, 783. (c) Zhou, J.; van Zijl, P. C. M. *Prog. Nucl. Magn. Reson. Spectrosc*. **2006**, *48*, 109. (d) Woods, M.; Woessner, D. E.; Sherry, A. D. *Chem. Soc. Rev*. **2006**, *35*, 500. (e) Ali, M. M.; Liu, G.; Shah, T.; Flask, C. A.; Pagel, M. D. *Acc. Chem. Res*. **2009**, *42*, 915. (f) Viswanathan, S.; Kovacs, Z.; Green, K. N.; Ratnakar, S. J.; Sherry, A. D. *Chem. Rev*. **2010**, *110*, 2960. (g) Terreno, E.; Castelli, D. D.; Viale, A.; Aime, S. *Chem. Rev*. **2010**, *110*, 3019. (h) Soesbe, T. C.; Wu, Y.; Sherry, A. D. *NMR Biomed*. **2013**, *26*, 829.

(127)   Thorarinsdottir, A. E.; Du, K.; Collins, J. H. P.; Harris, T. D. *Submitted.*

(128)   (a) Allen, J.; Damodaran, K. *Magn. Reson. Chem.* **2015**, *53*, 200. (b) Mitrev, Y.; Simova, S.; Jeannerat, D. *Chem. Commun.* **2016**, *52*, 5418. (c) Salvati, A.; Lynch, I.; Malmborg, C.; Topgaard, D. *J. Colloid Interface Sci.* **2007**, *308*, 542.

(129)   Emsley, L.; Bodenhausen, G., Gaussian Pulse Cascades: *Chem. Phys. Lett.* **1990**, *165*, 469.

APPENDIX

ADDITIONAL DETAILS OF MÖSSBAUER SPECTRAL ANALYSIS (SEE SECTION 2.4.2)

The isomer shifts observed[†] for six-coordinate predominately nitrogen-bonded high-spin iron(II) complexes are usually in the range of 1.00 to 1.10 mm/s at 295 K and 1.15 to 1.25 mm/s at 5 K. Further, in the analogous iron(III) complexes the isomer shifts usually are in the range of 0.4 to 0.5 mm/s at 295 K and exhibit rather smaller increases to ca. 0.5 to 0.6 mm/s upon cooling to 5 K. Hence, it is apparent from Table 2.3 that the observed iron(II) isomer shifts are typical for the coordination environment found in **1**. In contrast, as shown in Table 2.4, the isomer shifts observed in **2** for iron(II) are substantially lower than normal whereas those of the iron(III) are somewhat higher than expected, a difference that is expected in a mixed valence iron(II/III) complex.

The temperature dependence of the electron hopping relaxation obtained from the fits shown in Figure 2.5 is shown in Figure 5.1. As is shown at the top of this figure the temperature dependence of the isomer shifts of the iron(II) and iron(III) in **2** is well fit with the Debye model[‡3] for the second-order Doppler shift and yields Mössbauer temperatures, Θ_M, of 206(46) and 624(78) K for the iron(II) and iron(III) ions, respectively, a difference that is perhaps higher than expected, and presumably is related to the mixed-valence nature of **2**.

[†] (a) Little, B. F.; Long, G. J. *Inorg. Chem.* **1978**, *17*, 3401. (b) Reiff, W. M.; Long, G. J. *Mössbauer Spectroscopy Applied to Inorganic Chemistry*; Long, G. J., ed., Volume 1, Plenum Press: New York, NY, 1984, pp. 245.

[‡] (a) Shenoy, G. K.; Wagner, F. E.; Kalvius, G. M. *Mössbauer Isomer Shifts*; Shenoy, G. K.; Wagner, F. E., eds.; North-Holland: Amsterdam, the Netherlands, 1978, p 49. (b) Owen, T.; Grandjean, F.; Long, G. J.; Domasevitch, K. V.; Gerasimchuk, N. *Inorg. Chem.* **2008**, *47*, 8704.

The temperature dependence of the logarithm of the total Mössbauer spectral absorption area is shown in Figure 2.6 and a fit yields a Debye temperature, Θ_D, of 119(3) K. The logarithm of the absorption area observed at 50 K for **2** (a data point that is not included in the fit shown) is clearly low. This low value indicates that the velocity range of ± 4 mm/s used at 50 K is somewhat too restricted and, as a consequence, some fraction of the absorption area just above and below ± 4 mm/s is missing from the total spectral area. In addition, the Θ_D value of 119(3) K is rather low and indicates that the binding of the iron ions in **2** is weaker than would be the case in a Class I trapped mixed valence iron(II) and iron(III) complex with virtually no electron delocalization by electron hopping on the Mössbauer timescale.

It is known[†] that Θ_M is typically two to three times larger than Θ_D because these two temperatures sample different lattice vibrational properties. More specifically, the isomer shift depends on $<v^2>$, the mean-square vibrational velocity of the iron-57 nuclide whereas the absorption area depends on $<x^2>$, the mean-square atomic displacement of the nuclide; there is no relationship independent model relating these two mean-square values. Measurements on structurally related six-coordinate molecular iron(II) complexes indicate that Θ_M is often twice the Θ_D value and may be as much as three to four times larger for some high-spin iron(II) salts. In **2**, the increase by a factor of ca. 3.5 in going from Θ_D to a Θ_M of 415 K for the average of the iron(II) and iron(III) sites in **2** is realistic for a Class II mixed-valence high-spin iron(II/III) complex undergoing electron hopping.

The temperature dependence of the quadrupole splitting, ΔE_Q, in **2** is shown in Figure 5.1. As expected, the ΔE_Q of the high-spin iron(III) ion is virtually independent of temperature between 50 and 260 K. In contrast and as expected, the temperature dependence of ΔE_Q for the iron(II) ion

is found to be larger, decreasing from 3.17(2) mm/s at 50 K to 2.39(2) mm/s at 260 K. The fit of the iron(II) quadrupole splitting with the Ingalls model[§] yields a low symmetry splitting of the t_{2g} orbitals of 605(10) K or 420(7) cm^{-1}, a splitting that is consistent with the pseudooctahedral coordination environment about the iron(II) ion in **2**.

The analysis of the 5 K Mössbauer spectrum of **2**, shown in Figure 5.2, is problematic because it reveals at least three broadened sextets and, apparently, a small amount of iron(III) impurity. The analysis shown in Figure 5.2, which uses the approach of Dattagupta,[**] assumes that at 5 K **2** is a Class I trapped mixed valence iron(II) and iron(III) complex with virtually no electron delocalization, but in which the iron(II) and iron(III) ion moments undergo ±z anisotropic slow paramagnetic relaxation with a frequency of 6.8(3) MHz similar to the Lamor precession frequency; ±z are the limiting orientations of the relaxing hyperfine field and, hence the magnetic moment, along the principal axis of the electric field gradient tensor, a direction that is unknown but is most likely normal to the plane of the bridging ligand. Other relaxation models, with either isotropic or anisotropic relaxation models yielded far poorer fits. A more definitive analysis of the low temperature slow paramagnetic relaxation of the iron(II) and iron(III) ions in **2** must await more detailed measurements of the Mössbauer spectra of **2** between 2 and 50 K.

The result of the analysis of the 5 K Mössbauer spectrum of **2** with an intrinsic linewidth, Γ, of 0.4 mm/s is shown with the components in Figure A.2 and the corresponding parameters are given in

---

[§] Ingalls, R. *Phys. Rev.* **1964**, *133*, A787-A795.
[**] Dattagupta, S.; Blume, M. *Phys. Rev. B* **1974**, *10*, 4540.

Table A.1. A viable fit requires one iron(II) sextet, shown in green, and two similar iron(III) sextets, shown in red, in an area ratio of 1 to 2; the iron(II) to iron(III) area ratio is 1 to 1.

It has been found that it is not possible to fit the observed relaxation profile with isomer shifts, δ, and quadrupole splittings, ΔE_Q, that are fully consistent with the hyperfine parameters observed at 50 to 260 K, temperatures at which **2** behaves as a class II/III mixed valence compound with electron hopping on the Mössbauer timescale. However, the observed 5 K hyperfine parameters given in Table S2b for both the iron(II) and the two iron(III) sextets are consistent with the assignment shown.
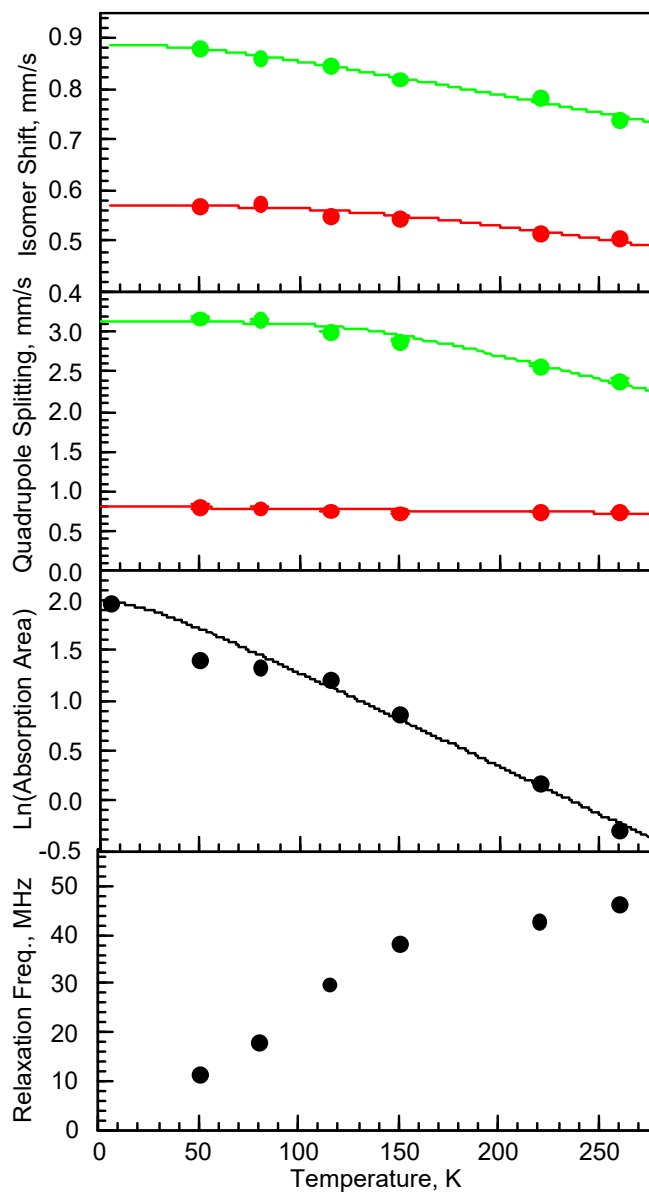
Figure A.1 | Mössbauer spectral parameters for [(Me₃TPyA)₂Fe₂(L)](BArᶠ₄)₃ (**2**) obtained as a f(T) from the electron hopping relaxation fits shown in Figure 2.5. The results are shown in green, for iron(II), in red for iron(III), and in black for the entire complex. The solid line fits of the isomer shifts and the logarithm of the total absorption area have been obtained by using the Debye model for a solid and yield, for the isomer shifts, Mössbauer temperatures, Q_M, of 206(46) and 624(78) K for iron(II) and iron(III), respectively, and for the logarithm of the absorption area, a Debye temperature, Q_D, of 119(3) K. The fit of the iron(II) quadrupole splitting with the Ingalls' model yields a low symmetry splitting of the t_{2g} orbitals of 605(10) K or 420(7) cm^{-1}.
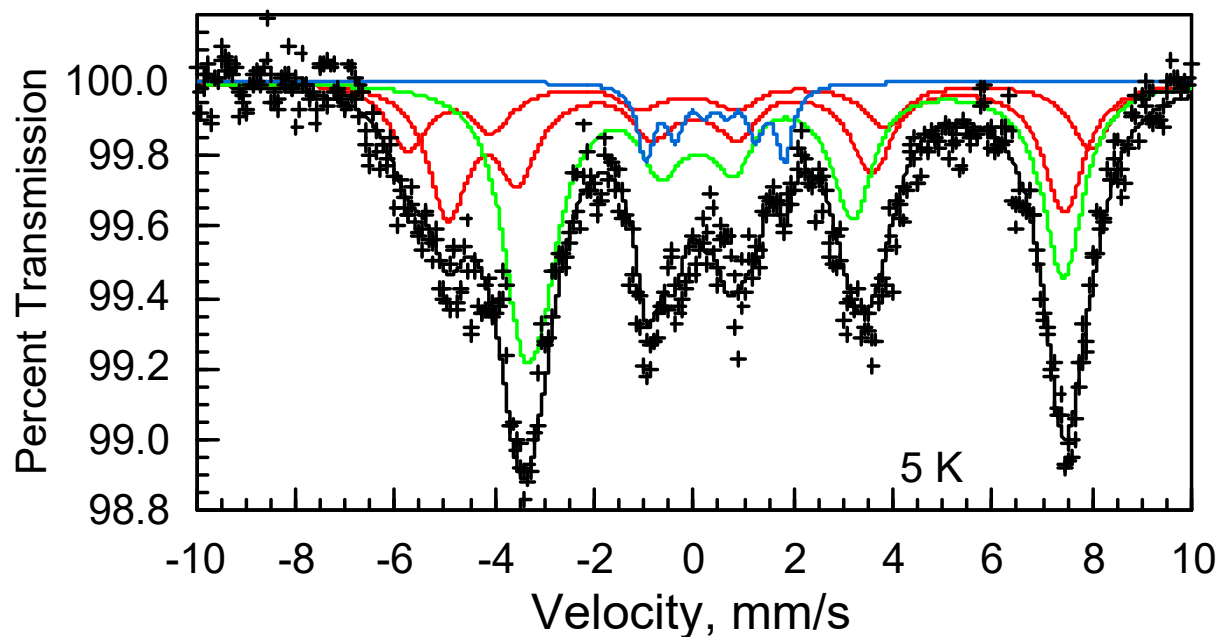
Figure A.2 | 5 K Mössbauer spectrum for **2**. Green, red, and blue lines are fits corresponding to Fe^{II} sites, Fe^{III} sites, and an Fe^{III} impurity, respectively.

Table A.1 | 5 K Mössbauer Spectral Parameters[a] for **2**

Site	d, mm/s[b]	DE_Q, mm/s	H, T	n, MHz	% Area
Fe(III)	0.50(3)	+1.24(5)[c]	42.7(4)	6.8(3)[c]	16(2)[c]
Fe(III)	0.63(3)	+1.24(5)[c]	38.5(3)	6.8(3)[c]	31(2)[c]
Fe(II)	1.02(2)	+1.91(4)	33.9(2)	6.8(3)[c]	46(2)
Fe(III)[d]	0.43(3)	0	8.6(2)	0	7(2)

[a]Statistical fitting errors are given in parenthesis. The actual errors may be two to three times larger. For all components G is fixed at 0.4 mm/s and $q = 0°$. [b]The isomer shifts are reported relative to a-iron foil measured at 295 K. [c]Adjusted parameters constrained to be held in a fixed ratio. [d]Probably an iron(III) impurity.

CURRICULUM VITAE

EDUCATION

Northwestern University, Evanston, Illinois   **Expected September 2017**

PhD. in Chemistry | GPA: 3.71/4.00

Bryn Mawr College, Bryn Mawr, Pennsylvania   **2012**

Bachelor of Arts in Chemistry with Honors, *magna cum laude* | GPA: 3.90/4.00

PUBLICATIONS

1. Gaudette, A. I., Harris, T. D. "pH-Dependent Spin-State Population and ^{19}F NMR Chemical Shifts via Remote Ligand Protonation in an Iron(II) Complex" *Manuscript in Preparation.*

2. Thorairinsdottir, A. E.; Gaudette, A. I., Harris, T. D. "Spin Crossover and High-Spin Iron(II) Complexes as Chemical Shift-Based ^{19}F MR Thermometers" *Chem. Sci.* **2017**. *8*, 2448.

3. Gaudette, A. I.; Jeon, I.-R.; Anderson, J. S.; Grandjean, F.; Long, G. L., Harris, T. D. "Electron Hopping through Double-Exchange Coupling in a Mixed-Valence Diiminobenzoquinone-Bridged Fe_2 Complex" *J. Am. Chem. Soc.* **2015**. *137*, 12617.

RESEARCH PRESENTATIONS

American Chemical Society National Meeting, San Francisco, CA, *Oral Presentation*   **2017**

Air Force Center of Excellence Meeting, Evanston, IL, *Oral Presentation*   **2017**

Wayne State Graduate Research Symposium, Detroit, MI, *Poster Presentation*   **2016**

BIP Departmental Seminars, Evanston, IL, *Oral Presentations*   **2016, 2015, 2014, 2013**

AWARDS AND HONORS

Donald E. Smith Award, *Northwestern University*   **2017**

- Awarded for excellence in 400-level teaching.

Kemin Travel Award, *Kemin Industries*   **2017**

- Competitive grant to fund travel to the American Chemical Society National Meeting.

Basolo Fellowship, *Northwestern University*   **2012–2013**

- Highly selective award presented to first-year graduate students.

ACS Undergraduate Award in Inorganic Chemistry, *Bryn Mawr College*   **2012**

- Awarded to top graduating senior in inorganic chemistry.

Elizabeth S. Shippen Scholarship in Science, *Bryn Mawr College*   **2011**

TEACHING EXPERIENCE

Advanced Inorganic Chemistry, Teaching Assistant and Guest Lecturer, *Northwestern University*   **2017**

- Delivered 20% of lectures to a class of 25 graduate students and senior chemistry majors.

General Chemistry Laboratory, Teaching Assistant, *Northwestern University*   **2012–2014**

- Lectured and supervised groups of 15 undergraduate students in chemistry laboratory procedures and safety.
- Created lab report questions designed to relate laboratory observations to lecture material.
- Graded weekly lab reports, providing comments and feedback.

X-Ray Crystallography Laboratory, Teaching Assistant, *Northwestern University*   **2013–2014**